



**HAL**  
open science

# The contribution of experimental volcanology to the study of the physics of eruptive processes, and related scaling issues: A review

Olivier Roche, Guillaume Carazzo

## ► To cite this version:

Olivier Roche, Guillaume Carazzo. The contribution of experimental volcanology to the study of the physics of eruptive processes, and related scaling issues: A review. *Journal of Volcanology and Geothermal Research*, 2019, 384, pp.103-150. 10.1016/j.jvolgeores.2019.07.011 . hal-02277033

**HAL Id: hal-02277033**

**<https://uca.hal.science/hal-02277033>**

Submitted on 9 Dec 2019

**HAL** is a multi-disciplinary open access archive for the deposit and dissemination of scientific research documents, whether they are published or not. The documents may come from teaching and research institutions in France or abroad, or from public or private research centers.

L'archive ouverte pluridisciplinaire **HAL**, est destinée au dépôt et à la diffusion de documents scientifiques de niveau recherche, publiés ou non, émanant des établissements d'enseignement et de recherche français ou étrangers, des laboratoires publics ou privés.

# **The contribution of experimental volcanology to the study of the physics of eruptive processes, and related scaling issues: a review**

Olivier Roche<sup>1</sup>, Guillaume Carazzo<sup>2</sup>

<sup>1</sup> Laboratoire Magmas et Volcans, Université Clermont Auvergne, CNRS, IRD, OPGC, F-63000 Clermont-Ferrand, France.

<sup>2</sup> Université de Paris, Institut de physique du globe de Paris, CNRS, F-75005 Paris, France

## **Abstract**

The experimental approach has become a major tool increasingly used by volcanologists in recent decades to investigate the physics of eruptive processes in complement to field and theoretical works. Researchers have developed various methodologies to study volcanic phenomena at reduced length scale. The works involve natural or analogue materials and their types range from first-order tests, to identify fundamental processes and make qualitative comparison with field observations, to more sophisticated experiments in which precise data obtained in a controlled environment can be used to validate outputs of theoretical models. Scaling is a central issue to ensure dynamic similarity between the small-scale experiments and the large-scale volcanic phenomena when natural conditions cannot be simulated due to inherent length scale difference and/or technical limitations. In this respect, dimensionless numbers are used to map physical regimes and to define scaling laws, which allow experimental results to be extrapolated to natural scale. This review presents the variety of experimental studies conducted to investigate subterranean and aerial volcanic phenomena involving in particular fluid-particle mixtures. We focus on the major scaling issues and the physical regimes investigated, and we also highlight in a historical perspective some of the major advances achieved through experimental studies. Finally we conclude on some perspectives for future works.

## 1. Introduction

Volcanic phenomena are studied by observing eruptions and their products as well as by indirect theoretical or experimental methods. Observation is necessary but it is not always possible or does not provide all the information on processes because volcanic eruptions are relatively rare, often dangerous and sometimes occur in remote areas, and the interpretation of their final products to discuss the dynamics of eruptions can be equivocal. In this respect, laboratory experiments represent an ideal complementary approach. Although experimental work involves simple configurations and may have severe limitations due to scaling issues, it also has advantages since experiments can be repeated and observed globally while the physical parameters involved are generally well characterized and controlled. Experimental studies are also considered to validate hypotheses formulated in theoretical models used to predict the characteristics and consequences of volcanic eruptions. For these reasons, experimental volcanology has been widely considered by the scientific community since the late 1970s. The recognition by early workers of the relevance of concepts developed by fluid dynamists to better understand fundamental eruptive processes, in particular, is undoubtedly a milestone for volcanology (Huppert 1986).

Experimentalists have adopted different approaches to studying volcanic phenomena (Mader et al. 2004). The first concerns the material, i.e. natural or analogue, used in the experiments. Studies involving natural materials to measure properties (e.g. magma viscosity) under real conditions (e.g. pressure and temperature) generally focus on small-scale processes. Those that use analogue materials focus instead more often on large-scale process dynamics and require a scaling procedure to ensure dynamic similarity between small-scale experiments and large-scale natural phenomena. Another issue is the subject of the experiments according to the degree of knowledge of the physics of the phenomenon addressed, and two approaches are used. The first can be described as *exploratory*, and experiments are conducted to identify fundamental processes when basic physics is poorly known. In contrast, a second approach can be used to test hypotheses of theoretical models based on well constrained physical laws, by comparing the results of simulations with those of experiments.

The aim of this review is to present some of the major advances in volcanology achieved through experimental investigations, focusing on recent works and on studies addressing scaling issues. Unfortunately, we have had to select from the considerable and ever-increasing number of publications dedicated to experimental volcanology, and the fact that some works are not cited is in no way based on scientific quality criteria. First, we present the principles of dimensional analysis and the methods for obtaining dimensionless numbers (detailed procedures are given in the appendix), and we discuss how these numbers can be used to study volcanic processes. Then, we present studies on volcanic phenomena, essentially involving fluid-particle mixtures, according to the natural evolution of magmatic systems, from the deep levels where magmas are stored and transported (magmatic chambers, intrusions, conduits) to the surface levels where products are emitted and dispersed (plumes, gravitational flows). Experimental studies on volcanic phenomena were reviewed recently by Kavanagh et al. (2018), and explosive events, in particular, were discussed by Lane and James (2011). We do not treat studies of water-saturated debris flows with applications to lahars (e.g. Iverson et al. 2010) nor volcano-tectonic processes (e.g. calderas and large-scale intrusions) and we redirect readers interested in the latter issue to the reviews of Acocella (2007), Geyer and Marti (2014), Merle (2015) and Galland et al. (2015).

## 2. The scaling issue

Laboratory experiments can reproduce some natural processes under controlled initial and boundary conditions. Analog experiments can be used to isolate key variables and to understand the role of each parameter independently. However, the complexity of the natural phenomena commonly raises the question of the reliability of the small-scale experimental set-up to correctly simulate the natural processes. This concern is a major question for experimental studies in Earth Sciences in general (Paola et al. 2009), which can be overcome through large-scale experiments (Valentine et al. 2011, Iverson 2015), through a careful scaling analysis for some relatively simple systems (Huppert and Sparks 1984, Woods 1997, Burgisser et al. 2005), or by mathematical modeling of the dynamics of the system (Jaupart and Vergnolle 1989, Woods and Caulfield 1992, Balmforth et al. 2000). Large-scale experiments are very useful to capture the relevant time and length scales, regimes and material properties of natural

phenomena but some scaling issues may remain and their application is up to now restricted to conduit flows (Pioli et al. 2012), volcanic plumes (Dellino et al. 2007, 2010), pyroclastic density currents (or PDC, Lube et al. 2015, Breard et al. 2016), lava flows (Lev et al. 2012, Edwards et al. 2013), phreatomagmatic eruptions (Valentine et al. 2012) and debris flows (Iverson et al. 2010).

Scaling analysis is fundamental to ensure that laboratory experiments are suitable analog for natural systems. Designing an experiment requires to simplify the natural process while reproducing correctly the balance of forces. A first step is to identify the relevant set of dimensionless variables that characterizes the system, either by normalizing the governing equations if they are known or by doing a dimensional analysis (see Appendix). The values of the dimensionless numbers are then calculated for the natural phenomenon, and the experimental set-up is designed in order to reproduce those values in the laboratory. It is generally impossible to match all the conditions in the natural system but the dimensionless numbers can be used to identify relevant dynamical regimes and to discuss the limitations of the experimental results.

For experiments involving fluid flows, the Reynolds ( $Re$ ), the Grashof ( $Gr$ ), and the Richardson numbers ( $Ri$ ) give a minimum set of dimensionless parameters. The Reynolds number quantifies the importance of inertial to viscous forces within the fluid (Reynolds 1883):

$$Re = \frac{\rho UL}{\eta}, \quad (1)$$

where  $U$  and  $L$  are the characteristic velocity and length scales for the flow, and  $\rho$  and  $\eta$  are the density and dynamic viscosity of the fluid, respectively. The Grashof number compares the buoyancy and viscous forces within the fluid (Turner 1973):

$$Gr = \frac{g' L^3}{\nu^2}, \quad (2)$$

where  $\nu = \eta/\rho$  is the kinematic viscosity of the fluid, and  $g' = g [(\rho - \rho_a)/\rho_a]$  is the reduced gravity of the flow, with  $g$  the acceleration of gravity, and  $\rho_a$  the density of the ambient fluid. Combining the above two dimensionless parameters gives the Richardson number (Batchelor 1953):

$$Ri = \frac{g' L}{U^2}, \quad (3)$$

which characterizes the relative importance of the buoyancy and inertia forces within the fluid and is equivalent to the densimetric Froude number  $Fr = 1/Ri^{1/2}$ . A common problem with laboratory experiments is to reproduce the high values of the Reynolds number in turbulent flows (i.e.,  $Re \sim 10^7$ - $10^9$  in volcanic plumes and PDC, see Table 1). Reaching such high values with a small experimental set-up (i.e., with a small length scale  $L$ ) requires to work either with fluids with a very low kinematic viscosity ( $\nu$ ) or to use very high velocities ( $U$ ). Since no fluid has a kinematic viscosity several orders of magnitude lower than that of water or air, it is generally easier to work at high velocities. However, increasing  $U$  makes difficult to reproduce the Richardson number of natural flows. To overcome this issue, experimentalists commonly use the Reynolds number independence principle, which states that as long as the Reynolds number is high enough its exact values does not strongly influence the flow dynamics (Paola et al. 2009). Since the Reynolds number controls the ratio of the largest (i.e., the outer length  $L$ ) to smallest (i.e., the Kolmogorov length) scales of turbulence, increasing its value to those observed in nature would only reduce the turbulence fine scale. In general, when designing an experimental set-up, it is useful to choose a velocity scale  $U$  large enough to reach high values of Reynolds number ( $Re > 10^3$ , i.e., turbulent regime) but small enough to reproduce appropriate values of Richardson or Grashof numbers. In low Reynolds number phenomena, such as lava flows or dyke intrusions, the velocity scale is chosen according to the viscosity of the fluid used (i.e., water, air, gases, gelatin, wax, oil or syrup) to match the natural values of  $Re$ .

Numerous volcanic phenomena involve multiphase flows where solid particles interact with each other depending on their concentration in the flow. In dilute mixtures, such as primary magmatic liquids or volcanic plumes, particle-particle interactions are limited but a complex mechanical coupling between the fluid and the solid phases exists. The Stokes ( $St$ ) and stability numbers ( $\Sigma$ ) fully characterize this two-way coupling (Burgisser and Bergantz 2002, Burgisser et al. 2005). The Stokes number corresponds to the ratio of the inertial force to viscous force of a particle, assuming that  $U^2/L$  is the scale of fluid acceleration (Elghobashi 1994):

$$St = \frac{|\rho_p - \rho| d_p^2 U}{18 f \eta L}, \quad (4)$$

where  $\rho_p$  is the particle density,  $d_p$  is the particle diameter (or effective particle diameter for non-spherical particles), and  $f$  is a drag factor. The stability number is the ratio of gravity force (or buoyancy force) to viscous force of a particle (Burgisser et al. 2005):

$$\Sigma = \frac{|\rho_p - \rho| g d_p^2}{18 f \eta U}. \quad (5)$$

These two numbers fully characterize the behavior of the particles in the flow. Where  $St > 1$  and  $\Sigma > 1$ , particles are strongly decoupled from the fluid phase and either settle or are expelled from the flow. Where  $St < 1$  and  $\Sigma < 1$ , particles are strongly coupled with the fluid phase, a regime that favors the transport of the solid fraction. Intermediate cases where  $St \sim 1$  and  $\Sigma \sim 1$ , or  $St < 1$  and  $\Sigma > 1$ , or  $St > 1$  and  $\Sigma < 1$  correspond to a third class where a strong two-way coupling between the fluid and the particles exists. When designing an experimental set-up, these two numbers can be used to select the appropriate particle characteristics (i.e., size and density) to reproduce a phenomenon where particles are either expelled from the fluid phase or transported within the flow.

In dense mixtures (e.g., dense PDC), particle-particle interactions may dominate fluid-particle interactions. The Savage number (Sa) is relevant when interstitial pore fluid pressure is negligible and it compares the grain collisional to frictional stresses (Savage, 1984):

$$Sa = \frac{\rho_p \gamma^2 d_p^2}{|\rho_p - \rho| g H}, \quad (6)$$

where  $\gamma$  is the characteristic shear rate, and  $H$  is the vertical length scale of the flow, assuming that the frictional stress is proportional to the inter-grain normal stress that is controlled by the grain-static pressure. Frictional flows have  $Sa < \sim 0.1$  whereas collisions affect the flow dynamics significantly at  $Sa > \sim 0.1$ . Other dimensional numbers are defined when the interstitial fluid phase has a non negligible effect. The Bagnold number (Ba) can be used to compare the collisional solid stresses and viscous fluid stresses (Bagnold 1954, Iverson 1997):

$$Ba = \frac{\rho_p \gamma d_p^2 \varepsilon_p}{\eta (1 - \varepsilon_p)}, \quad (7)$$

where  $\varepsilon_p$  is the particle volume fraction. In flows with  $Ba < 40$ , the interstitial fluid viscosity strongly influences the flow dynamics (macro viscous regime) and the shear stress is proportional to the shear rate  $\gamma$ . In flows with  $Ba > 450$ , particle collision dominates (grain inertia regime) and the shear stress becomes proportional to the square of the shear rate. Intermediate cases where  $40 < Ba < 450$  correspond to a transitional regime. The Darcy number (Da) may also be used to calculate the ratio of viscous fluid-particle interaction stresses to particle inertial stresses (Iverson 1997):

$$Da = \frac{\eta}{\rho_p \gamma k \varepsilon_p}, \quad (8)$$

where  $k$  is the permeability of the granular medium. This number also quantifies the tendency for interstitial pore fluid pressure to buffer particle interactions, and solid-fluid interactions dominate where Da is high. Alternatively, the Darcy number may be written as  $k/L^2$ , which is commonly used in studies of heat transfer in porous media. The Savage, Bagnold and Darcy numbers can be used to fully characterize the dynamical regime of dense fluid-particle flows and to identify the key forces reproduced in the laboratory.

Volcanic flows also commonly transport gas bubbles (e.g., conduit or lava flows) or liquid droplets (e.g., volcanic plumes). Several dimensionless numbers can be used to quantify the importance of stabilizing surface tension forces to other destabilizing forces on the formation and transport of bubbles or droplets. The Weber number (We) compares the fluid inertia and the fluid surface tension (Clift et al. 1978, Brennen 1995):

$$We = \frac{\rho d_b U^2}{\sigma}, \quad (9)$$

where  $d_b$  is the bubble diameter, and  $\sigma$  is the surface tension. In flows with  $We > 1$ , the fluid inertia dominates over surface tension and tends to prevent the formation of bubbles. Where  $We < 1$ , surface tension forces are large enough to stabilize the bubbles. The capillary number (Ca) compares the fluid viscous forces and the fluid surface tension (Manga et al. 1998):

$$Ca = \frac{\eta d_b d\varepsilon}{\sigma dt}, \quad (10)$$

where  $d\varepsilon/dt$  is the strain rate. Capillary forces dominate over viscous forces where  $Ca < 1$ , and bubbles remain nearly spherical and preserved in the flow. Where  $Ca > 1$ , viscous forces tend to deform the bubbles, which become elongated and can in turn reduce the flow viscosity. Destabilizing bubbles occurs

at larger values of Ca depending on the shear field (Rust and Manga 2002). Lastly, the Eötvös (Eo) number (also called Bond number) gives the ratio of the gravitational to surface tension forces (Clift et al. 1978):

$$Eo = \frac{\Delta\rho g d_b^2}{\sigma}, \quad (11)$$

where  $\Delta\rho = \rho_b - \rho$  is the density difference of the two phases, with  $\rho_b$  the bubble density. Similarly to the Weber and Capillary numbers, low or high values of the Eötvös number indicate either stabilization or destabilization of bubbles in the flow, respectively. Two additional dimensionless numbers are commonly used to characterize the formation of bubbles/droplets in a two-phase mixture. The Morton (Mo) number compares the destabilizing gravitational, viscous and inertia forces to the stabilizing surface tension forces ( $Mo = We^3 Ri / Re^4$ , with the characteristic length scale set as the bubbles diameter  $L=d_b$ ), and the Ohnesorge (Oh) number compares the inertia, viscous and surface tension forces ( $Oh = We^{1/2} / Re$ ).

Thermal interactions are important in volcanic flows that are far from thermal equilibrium with the surrounding environment (i.e., country rock or cold atmosphere). Heating and cooling induce strong changes in rheology that affect the flow dynamics. The Prandtl number (Pr) can be used to compare the viscous and thermal diffusion rates (Batchelor 1954):

$$Pr = \frac{\eta}{\rho\kappa}, \quad (12)$$

where  $\kappa$  is the thermal diffusivity. In most flows of magmatic liquids, the Prandtl number is very large (i.e.  $Pr > 10^4$ , see Table 1) because the momentum diffusivity dominates over thermal diffusivity. However, in surface processes involving gas as the fluid phase, such as PDC and volcanic plumes, the Prandtl number is of the order of  $10^{-1}$  and heat diffuses quickly compared to momentum. Interestingly, this parameter only depends on the material characteristics and can thus be easily varied in the laboratory from  $10^{-1}$  (most gases) to  $10^5$  (silicone oils). The Peclet number (Pe) compares the relative importance of heat transfer rate by convection and conduction processes (Turner 1973):

$$Pe = \frac{UL}{\kappa}, \quad (13)$$

which is equivalent to the product of the Reynolds and Prandtl numbers ( $Pe = Re \times Pr$ ). In most geological flows, the Peclet number is large (i.e.,  $Pe > 10^2$ , see Table 1) because convective processes mainly dominate heat transfers during cooling. Alternatively, it may be useful to define a Rayleigh number (Ra) such as (Batchelor 1954),

$$Ra = \frac{g' L^3}{\nu\kappa}, \quad (14)$$

which is equivalent to the product of the Grashof and Prandtl numbers ( $Ra = Gr \times Pr$ ). The Rayleigh number controls the onset and style of convectonal instabilities, and is largely used in studies of magma chamber dynamics where  $g'$  is imposed by temperature and/or compositional differences.

Table 1 summarizes the dimensionless numbers presented in this section and provides the range of values for some volcanic phenomena including magma chambers and intrusions, conduit flows, plumes, pyroclastic density currents and lava flows. This set of dimensionless numbers can be used to design and scale future laboratory experiments, but other dimensionless parameters may also be built using ratios including the characteristic length, velocity and time scales, depending on the problem investigated. The variables used to define these numbers are listed in Table 2. As shown in the following sections, the purpose of the scaling analysis is commonly (i) to identify the dynamical regimes observed in the experiments, and (ii) to discuss the limitations of the experimental results when applying them to the natural system. Scaling analysis may be used also to compare results of experiments with those of numerical modeling (e.g. Mier-Torrecilla et al. 2012). Other dimensionless numbers not presented in this section but relevant for volcanic phenomena are presented hereafter.

**Table 1.** Common ranges of some physical parameters and dimensionless numbers typical of volcanic phenomena (Griffiths 2000, Seyfried and Freundt 2000, Burgisser et al. 2005, Carazzo and Jellinek 2012, Roche 2012, Andrews and Manga 2012).

Number	Magma chambers	Magma intrusions	Conduit flows	Volcanic plumes	PDC (dense)	Lava flows
$\rho$ (kg m <sup>-3</sup> )	2200 - 2800	2200 - 2800	2200 - 2800	2 - 90	200 - 1500	2200 - 2400
$\Delta\rho$ (kg m <sup>-3</sup> )	100 - 400	100 - 400	100 - 400	2 - 90	200 - 1500	2200 - 2400
$\rho_p$ (kg m <sup>-3</sup> )	2200 - 2400	2200 - 2400	2200 - 2400	700 - 2400	700 - 2400	2200 - 2400
$d_p$ (m)	10 <sup>-5</sup> - 10 <sup>-3</sup>	10 <sup>-5</sup> - 10 <sup>-3</sup>	10 <sup>-5</sup> - 10 <sup>-3</sup>	10 <sup>-5</sup> - 10 <sup>-2</sup>	10 <sup>-4</sup> - 10 <sup>-2</sup>	10 <sup>-5</sup> - 10 <sup>-3</sup>
$U$ (m s <sup>-1</sup> )	0.01 - 1	10 <sup>-3</sup> - 1	1 - 10	150 - 500	10 - 150	0.1 - 1
$L$ (m)	10 - 10 <sup>3</sup>	0.1 - 1	1 - 10	50 - 200	1 - 50	1 - 10
$\eta$ (Pa s)	10 <sup>3</sup> - 10 <sup>8</sup>	10 <sup>2</sup> - 10 <sup>7</sup>	10 <sup>2</sup> - 10 <sup>7</sup>	10 <sup>-5</sup>	10 <sup>-5</sup>	10 <sup>2</sup> - 10 <sup>3</sup>
$\gamma$ (s <sup>-1</sup> )	10 <sup>-3</sup> - 10 <sup>-1</sup>	10 <sup>-3</sup> - 10 <sup>-1</sup>	10 <sup>-3</sup> - 10 <sup>-1</sup>	-	0.1 - 0.6	10 <sup>-3</sup> - 10 <sup>-1</sup>
$\varepsilon_p$ (-)	0.1 - 0.9	0.1 - 0.2	0.1 - 0.9	-	0.3 - 0.6	0.5 - 0.9
$k$ (m <sup>2</sup> s <sup>-1</sup> )	10 <sup>-15</sup> - 10 <sup>-11</sup>	10 <sup>-15</sup> - 10 <sup>-11</sup>	10 <sup>-15</sup> - 10 <sup>-11</sup>	-	10 <sup>-12</sup> - 10 <sup>-10</sup>	10 <sup>-15</sup> - 10 <sup>-11</sup>
$\kappa$ (m <sup>2</sup> s <sup>-1</sup> )	10 <sup>-7</sup> - 10 <sup>-6</sup>	10 <sup>-7</sup> - 10 <sup>-6</sup>	10 <sup>-7</sup> - 10 <sup>-6</sup>	10 <sup>-7</sup> - 10 <sup>-5</sup>	10 <sup>-8</sup> - 10 <sup>-7</sup>	10 <sup>-7</sup> - 10 <sup>-6</sup>
$d_b$ (m)	10 <sup>-5</sup> - 10 <sup>-3</sup>	10 <sup>-5</sup> - 10 <sup>-3</sup>	10 <sup>-5</sup> - 10 <sup>-2</sup>	10 <sup>-7</sup> - 10 <sup>-6</sup>	-	10 <sup>-5</sup> - 10 <sup>-3</sup>
$\sigma$ (N m <sup>-1</sup> )	0.05 - 0.4	0.05 - 0.4	0.05 - 0.4	10 <sup>-3</sup>	-	0.05 - 0.4
$d\varepsilon/dt$ (s <sup>-1</sup> )	10 <sup>-4</sup> - 10 <sup>-1</sup>	10 <sup>-4</sup> - 10 <sup>-1</sup>	10 <sup>-4</sup> - 10 <sup>-1</sup>	-	-	10 <sup>-4</sup> - 10 <sup>-1</sup>
$Re = \frac{\rho UL}{\eta}$	10 <sup>-6</sup> - 10 <sup>3</sup>	10 <sup>-4</sup> - 10 <sup>3</sup>	10 <sup>-4</sup> - 10 <sup>3</sup>	10 <sup>7</sup> - 10 <sup>9</sup>	10 <sup>5</sup> - 10 <sup>8</sup>	10 <sup>-1</sup> - 10 <sup>3</sup>
$Gr = \frac{g'L^3}{\nu^2}$	10 <sup>-2</sup> - 10 <sup>6</sup>	10 <sup>-7</sup> - 10 <sup>3</sup>	10 <sup>-4</sup> - 10 <sup>4</sup>	10 <sup>12</sup> - 10 <sup>19</sup>	10 <sup>11</sup> - 10 <sup>20</sup>	10 <sup>4</sup> - 10 <sup>8</sup>
$Ri = \frac{g'L}{U^2}$	10 <sup>-7</sup> - 10 <sup>1</sup>	10 <sup>-11</sup> - 10 <sup>-1</sup>	10 <sup>-11</sup> - 10 <sup>-3</sup>	10 <sup>-3</sup> - 10 <sup>1</sup>	10 <sup>-1</sup> - 10 <sup>3</sup>	10 <sup>-2</sup> - 10 <sup>2</sup>
$St = \frac{ \rho_p - \rho  d_p^2 U}{18f\eta L}$	10 <sup>-21</sup> - 10 <sup>-9</sup>	10 <sup>-19</sup> - 10 <sup>-6</sup>	10 <sup>-17</sup> - 10 <sup>-6</sup>	10 <sup>-4</sup> - 10 <sup>3</sup>	10 <sup>-5</sup> - 10 <sup>1</sup>	10 <sup>-14</sup> - 10 <sup>-6</sup>
$\Sigma = \frac{ \rho_p - \rho  g d_p^2}{18f\eta U}$	10 <sup>-15</sup> - 10 <sup>-4</sup>	10 <sup>-14</sup> - 10 <sup>-2</sup>	10 <sup>-15</sup> - 10 <sup>-5</sup>	10 <sup>-6</sup> - 10 <sup>1</sup>	10 <sup>-3</sup> - 10 <sup>2</sup>	10 <sup>-11</sup> - 10 <sup>-5</sup>
$Sa = \frac{\rho_p \gamma^2 d_p^2}{ \rho_p - \rho  g H}$	10 <sup>-17</sup> - 10 <sup>-10</sup>	10 <sup>-16</sup> - 10 <sup>-9</sup>	10 <sup>-17</sup> - 10 <sup>-10</sup>	-	10 <sup>-12</sup> - 10 <sup>-8</sup>	10 <sup>-16</sup> - 10 <sup>-9</sup>
$Ba = \frac{\rho_p \gamma d_p^2 \varepsilon_p}{\eta(1 - \varepsilon_p)}$	10 <sup>-19</sup> - 10 <sup>-6</sup>	10 <sup>-18</sup> - 10 <sup>-7</sup>	10 <sup>-17</sup> - 10 <sup>-5</sup>	-	10 <sup>-2</sup> - 10 <sup>3</sup>	10 <sup>-12</sup> - 10 <sup>-4</sup>
$Da = \frac{\eta}{\rho_p \gamma k \varepsilon_p}$	10 <sup>11</sup> - 10 <sup>23</sup>	10 <sup>11</sup> - 10 <sup>22</sup>	10 <sup>10</sup> - 10 <sup>21</sup>	-	10 <sup>2</sup> - 10 <sup>6</sup>	10 <sup>10</sup> - 10 <sup>17</sup>
$We = \frac{\rho d_b U^2}{\sigma}$	10 <sup>-6</sup> - 10 <sup>1</sup>	10 <sup>-8</sup> - 10 <sup>1</sup>	10 <sup>-2</sup> - 10 <sup>4</sup>	10 <sup>-1</sup> - 10 <sup>3</sup>	-	10 <sup>-4</sup> - 10 <sup>3</sup>
$Ca = \frac{\eta d_b d\varepsilon}{\sigma dt}$	10 <sup>-6</sup> - 10 <sup>5</sup>	10 <sup>-7</sup> - 10 <sup>4</sup>	10 <sup>2</sup> - 10 <sup>10</sup>	10 <sup>-14</sup> - 10 <sup>-10</sup>	-	10 <sup>-7</sup> - 10 <sup>1</sup>
$Eo = \frac{\Delta\rho g d_b^2}{\sigma}$	10 <sup>6</sup> - 10 <sup>9</sup>	10 <sup>2</sup> - 10 <sup>6</sup>	10 <sup>4</sup> - 10 <sup>9</sup>	10 <sup>6</sup> - 10 <sup>9</sup>	-	10 <sup>4</sup> - 10 <sup>7</sup>
$Pe = \frac{\sigma}{UL}$	10 <sup>5</sup> - 10 <sup>8</sup>	10 <sup>2</sup> - 10 <sup>7</sup>	10 <sup>6</sup> - 10 <sup>8</sup>	10 <sup>8</sup> - 10 <sup>11</sup>	10 <sup>10</sup> - 10 <sup>13</sup>	10 <sup>4</sup> - 10 <sup>8</sup>
$Pr = \frac{\kappa}{\eta}$	10 <sup>5</sup> - 10 <sup>11</sup>	10 <sup>4</sup> - 10 <sup>10</sup>	10 <sup>4</sup> - 10 <sup>10</sup>	10 <sup>-1</sup> - 10 <sup>0</sup>	10 <sup>-1</sup> - 10 <sup>0</sup>	10 <sup>4</sup> - 10 <sup>6</sup>
$Ra = \frac{g'L^3}{\nu\kappa}$	10 <sup>3</sup> - 10 <sup>7</sup>	10 <sup>-3</sup> - 10 <sup>13</sup>	10 <sup>1</sup> - 10 <sup>14</sup>	10 <sup>11</sup> - 10 <sup>19</sup>	10 <sup>10</sup> - 10 <sup>20</sup>	10 <sup>9</sup> - 10 <sup>14</sup>

**Table 2.** Summary of variables used in the scaling analysis.

Symbol	Definition	Units
$d_b$	Bubble or aerosol diameter	m
$d_p$	Particle diameter	m
$d\varepsilon/dt$	Strain rate	$s^{-1}$
$f$	Drag factor	-
$g$	Acceleration of gravity	$m\ s^{-2}$
$g'$	Reduced gravity	$m\ s^{-2}$
$k$	Permeability	$m^2$
$H$	Vertical flow length scale	m
$L$	Characteristic flow length scale	m
$U$	Characteristic flow velocity scale	$m\ s^{-1}$
$\gamma$	Characteristic shear rate	$s^{-1}$
$\varepsilon_p$	Particle volume fraction	-
$\kappa$	Thermal diffusivity	$m^2\ s^{-1}$
$\eta$	Fluid dynamic viscosity	Pa s
$\nu$	Fluid kinematic viscosity	$m^2\ s^{-1}$
$\rho$	Fluid density	$kg\ m^{-3}$
$\rho_a$	Ambient (fluid) density	$kg\ m^{-3}$
$\rho_b$	Bubble density	$kg\ m^{-3}$
$\rho_p$	Solid particle density	$kg\ m^{-3}$
$\sigma$	Surface tension	$N\ m^{-1}$

### 3. Volcanic phenomena investigated experimentally

#### 3.1 Magma properties and magma chambers

Understanding the physics that control magma emplacement within the crust to form magma chambers is a central issue in volcanology (e.g., Annen et al. 2015). Two experimental strategies have emerged over the last decades to decipher the mechanisms of magma migration, storage and remobilization: petrological studies of natural samples provided fundamental pre-eruptive parameters such as magma temperature, pressure, and composition (e.g., Hammer and Rutherford 2003; Scaillet et al. 2008), while experiments using analogue materials (e.g., Phillips et al. 1995) were used to investigate phenomena occurring in magma chambers. Here, we do not treat studies on petrological indicators but instead we review a few laboratory experiments aimed at better understanding (i) magma rheology and (ii) the dynamics of magma chambers.

##### 3.1.1 Magma rheology

Rheological characteristics of multiphase magmas have been extensively investigated theoretically and experimentally. Here, we point out the main steps forward to a better understanding of the effects of the bubbles and crystals on magma rheology, and redirect readers interested in these issues to the detailed review by Mader et al. (2013). Bagdassarov and Dingwell (1992) presented laboratory experiments to investigate the effect of porosity on the viscosity of rhyolite samples. Natural obsidian was fused to produce crystal-free rhyolite glasses with varying porosity by adjusting the duration and temperature of fusion. The viscosity and porosity of the samples were measured in order to determine a general relationship between the two parameters:

$$\eta = \frac{\eta_0}{(1-Cf)} \quad (15)$$

where  $\eta$  is the viscosity of the suspension,  $\eta_0$  is the viscosity of the pure liquid phase,  $f$  is the volume fraction of gas, and  $C$  is a dimensionless constant. The results showed that increasing the sample porosity up to 65% reduced the bulk viscosity by at least one order of magnitude, thereby strongly influencing

the eruptive style at the surface. Rust and Manga (2002) built on this work to study the effects of bubble deformation on the bulk viscosity. Corn syrup containing air bubbles was deformed by simple shear flow at low Reynolds number ( $<10^{-5}$ ) in a Couette flow viscometer. The shape and orientation of the air bubbles were accurately measured as a function of the bulk viscosity. The latter parameter was found to strongly depend on the volume fraction of bubbles and on the capillary number ( $Ca$ ), which characterizes the tendency of bubbles to deform (see equation 10). At high shear rates, bubbles deformed ( $Ca > 1$ ) and caused very little deformation of the streamlines around them, which significantly reduced the bulk viscosity of the suspension. However, at low shear rates, the bubbles remained nearly spherical ( $Ca < 1$ ) due to surface tension, resulting in an increase viscous dissipation around them, which significantly increased the bulk viscosity of the suspension. An experimental fit to the data was proposed to account for this effect:

$$\eta_r = \eta_{r,0} + \frac{\eta_{r,0} - \eta_{r,\infty}}{1 + (KCa)^m} \quad (16)$$

where  $\eta_r$  is the relative viscosity of the suspension (i.e., the ratio  $\eta/\eta_0$ ),  $\eta_{r,0}$  and  $\eta_{r,\infty}$  are the asymptotic values of relative viscosity at very low and very high shear rates, respectively, and  $K$  and  $m$  are dimensionless constants (Fig. 1a). Llewellyn et al. (2002) focused on the  $Ca < 1$  regime to determine the visco-elastic rheology of bubbles suspensions by comparing their theoretical model to observations of the deformation of suspensions of nitrogen bubbles in golden syrup subjected to forced oscillations. At high frequencies of oscillation, the bulk viscosity decreased with increasing gas volume fraction, a result consistent with previous studies (Bagdassarov and Dingwell 1992; Rust and Manga 2002). However, at low frequencies of oscillation, increasing the gas volume fraction led to increase the viscosity of the suspension. This reversal effect of gas content on the bulk viscosity was due to the varying bubble deformation with frequency, and can be described by a dimensionless dynamic capillary number,

$$Cd = \frac{\lambda \dot{\gamma}}{\dot{\gamma}}, \quad (17)$$

where  $\lambda$  is the relaxation time,  $\dot{\gamma}$  is the rate of change of imposed viscous forces, and  $\dot{\gamma}$  is the bulk strain rate.  $Cd$  compares the response time of bubble deformation and the characteristic time of shear rate acceleration. When  $Cd \gg 1$ , bubbles cannot deform in response to changes in the shear rate. On the other hand, when  $Cd \ll 1$ , bubbles are expected to maintain their equilibrium shape if sufficient strain is applied. The threshold strain depends on  $Ca$  (Ohashi et al., 2018).

The rheology of magmas can also be strongly influenced by the presence of crystals because additional work may be dissipated due to particle-particle and fluid-particle interactions. Mueller et al. (2010, 2011) presented laboratory experiments in which silicone oil with suspended monodisperse particles of varying aspect ratio was deformed. The results showed that increasing the particle volume fraction led to different behaviors. At very low particle contents, particle-particle interactions were negligible and the bulk viscosity of the suspension increased with particle content due to the additional energy required to flow around the particles. At increasing particle contents, particles started to interact and formed doublets that enhanced the distortion of flow lines and increased the bulk viscosity. At intermediate particle contents, the suspension became non-Newtonian and a shear-thinning behavior developed due to local viscous heating in the interstitial space between the particles, which reduced the viscosity at high strain rates. For higher particle contents, chains of particles formed accommodating the stress elastically until a yield stress was reached. At very high particle contents, the shear-thinning behavior was less important and the suspension behaved more as a Newtonian fluid with a yield stress (i.e., Bingham fluid). The reanalysis of a large database on the rheology of two-phase suspensions showed that the shape of the particles affects the maximum packing fraction in particular when particles are increasingly anisometric. Mueller et al. (2010) proposed a new relationship to calculate the viscosity of a suspension ( $\eta$ ) as a function of particle volume fraction ( $\phi$ ) and particle aspect ratio ( $r_p$ ), based on the Herschel-Bulkley model:

$$\eta = \frac{\tau_0}{\dot{\gamma}} + K \dot{\gamma}^{n-1} \quad (18)$$

where  $\tau_0$  is the yield strength,  $\dot{\gamma}$  is the strain rate,  $n$  is the flow index, and  $K$  is the consistency that can be written as,

$$K = \eta_0 \left(1 - \frac{\phi}{\phi_m}\right)^{-2} \quad (19)$$

where  $\phi_m$  is the maximum packing fraction that can be approximated by a log-Gaussian function:

$$\phi_m = \phi_{m,1} \exp\left(-\frac{(\log_{10} r_p)^2}{2b^2}\right) \quad (20)$$

where  $\phi_{m,1}$  is the maximum packing fraction for particles with  $r_p = 1$ , and  $b$  is a fitting parameter (Fig. 1b). This model allowed to explain why prolate and oblate particles tended to increase the suspension viscosity compared to spherical particles. The effect of bimodal particle size and shape on the viscosity was further studied by Cimarelli et al. (2011). Their results showed that increasing the proportion of isometric to spherical particles in the suspension led to an increase of viscosity by up to three orders of magnitude.

The transition from viscous to brittle behavior of the magma has received some attention since it largely controls the style of volcanic eruptions. Cordonnier et al. (2012) presented laboratory experiments in which crystal-melt suspensions were deformed under extreme temperature, pressure and strain rates conditions (Fig. 1c). The results demonstrated that the viscous-brittle transition depended on the relaxation state of the sample characterized by a Deborah number,

$$De = \frac{\eta_0 \dot{\epsilon}}{G_\infty}, \quad (21)$$

where  $\eta_0$  is the shear viscosity of the liquid phase,  $\dot{\epsilon}$  is the strain rate, and  $G_\infty$  is the elastic shear modulus of the melt. Below a critical  $De \sim 10^{-2.5}$ , the stress remained constant in the experiments during deformation in the viscous regime, whereas for  $De > 10^{-2.5}$ , cracks formed in the brittle regime (Fig. 1d), which allowed gas to escape and reduce overpressure. Hess et al. (2008) used a similar apparatus together with natural and synthetic silicate melts to determine the contribution of viscous heating on the melt temperature and rheology. Viscous heating was found to be of primary importance for highly viscous magmas at high strain rates, where the heat generated through viscous deformation was larger than the heat lost by conduction through the melt.

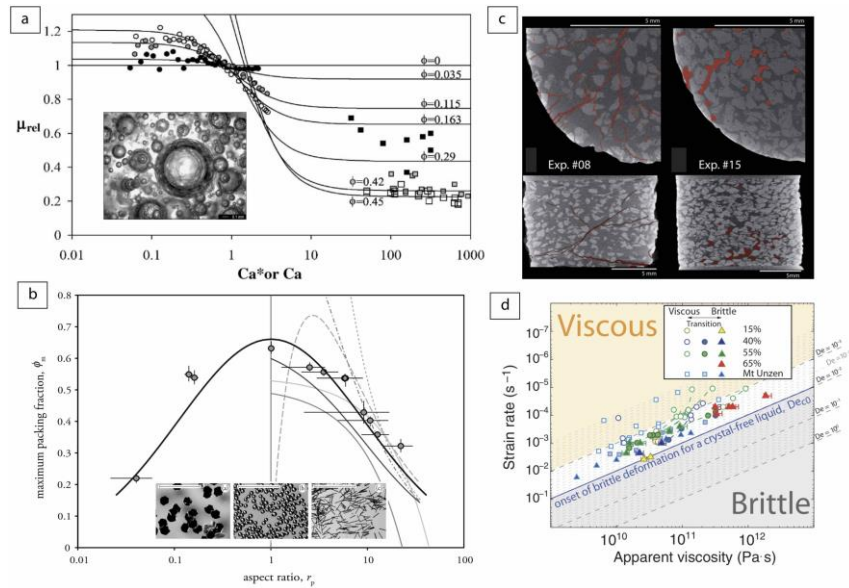


**Figure 1.** Laboratory results on magma rheology. (a) Relative viscosity of a corn syrup-air bubbles suspension as a function of the capillary number ( $Ca$ ) for increasing gas volume fraction ( $\phi$ ), and photograph of a suspension at low  $Ca$  (modified from Rust and Manga 2002). (b) Maximum packing fraction as a function of particle aspect ratio ( $r_p$ ), and photographs of the particles used in the experiments (modified from Mueller et al. 2011). (c) Cross sections of two deformed crystal-melt suspensions. (d) The viscous-brittle transition in laboratory experiments. Panels (c) and (d) are modified from Cordonnier et al. (2012). Symbols correspond to laboratory experiments in panels (a), (b), and (d).

### 3.1.2 Magma chamber dynamics

Recharge of a hot basaltic magma into the continental crust or a pre-existing silicic magma chamber drives many processes such as magma mixing, convection, crystallization, degassing, and melting of the roof/floor/wall materials. The physics of these processes has been investigated

experimentally for different types of magma chambers and compared to mathematical modeling. In particular, the processes leading to magma mixing in basaltic and silicic magma chambers have received a large attention over the last decades. Huppert and Turner (1981) carried out laboratory experiments in which a hot, dense layer of  $\text{KNO}_3$  was emplaced under a cold, lighter layer of  $\text{K}_2\text{CO}_3$  or  $\text{NaNO}_3$ . As cooling of the underlying layer occurred,  $\text{KNO}_3$  crystals formed and settled out at the bottom of the reservoir, decreasing in turn the density of the residual fluid. Once the density of the lower layer became equal to that of the upper layer, the interface between the two layers broke and the two layers mixed thoroughly together. The experimental results were compared to a simple analytical model describing the time rate of change of the temperatures in the lower and upper layers and found in good agreement. This laboratory model of magma chamber replenishment was later extended by Huppert et al. (1982a) who explored the effects of compositional zonation and input rates on magma mixing. The rapid injection of  $\text{KNO}_3$  beneath a stratified layer of  $\text{K}_2\text{CO}_3$  led to the formation of a series of convective layers in the upper layer. As in the homogeneous case, cooling favored crystallization in the lower layer and the residual fluid ended up rising in the upper layer. However, limited mixing was observed due to the stabilizing effect of compositional gradient in the upper layer that prevented the rise of  $\text{KNO}_3$  plumes. Slow injections rates of  $\text{KNO}_3$  beneath a homogeneous layer of  $\text{K}_2\text{CO}_3$  led on the other hand to vigorous mixing between the two layers. Thomas et al. (1993) presented similar laboratory experiments to examine the effect of gas bubbles on magma mixing. The experiments consisted in injecting small air bubbles at the base of a tank containing a lower layer of low viscosity liquid and an upper layer of high viscosity liquid, both at high Pr. Depending mostly on the viscosity ratio of the two layers, the bubbles either moved individually across the two layers, or formed a thin foam layer at the interface (Fig. 2a). In the first regime, some of the underlying fluid was entrained by the bubbles into the upper layer, and the two layers became progressively stirred into a homogeneous mixture. In the second regime, the bubble foam grew until it became gravitationally unstable and formed several two-phase plumes that rose into the upper layer driving in turn a strong mixing of the two layers. The authors proposed a model for the growth and destabilization of the foam layer in this second regime, which was found to capture the experimental results. A similar behavior was observed in the experiments of Woods and Cowan (2009) in which air bubbles were generated by decompression in a vacuum chamber. As the pressure decreased in the chamber, the lower layer of salt water and Natrosol released some of its dissolved air and hence contained small bubbles. The density of the lower layer became progressively lower than that of the upper layer of salt water and Natrosol, leading to overturn of the initial stratification (Fig. 2b). Phillips et al. (2001) considered the case of the replenishment of a shallow basaltic magma chamber by a bubble-rich basaltic magma. Their experiments showed that a turbulent bubble plume ( $\text{Re} > 10^3$ ) can be generated within the chamber, driving a large scale flow that redistribute the bubbles. Sato and Sato (2009) showed that the presence of magma pocket in a conduit can also strongly affect magma mixing. Their experimental set-up allowed to reproduce the simultaneous rise of mafic and silicic magmas using liquids with various density and viscosity (i.e., glycerin-water, syrup-water mixtures, glue, water...) at both low and high Reynolds numbers ( $\text{Re} \sim 10^{-3}$ - $10^2$ ). As the two liquids propagated in the conduit, the presence of a magma pocket enhanced the instability of the annular flow of the two liquids resulting sometimes in magma mixing even at low Reynolds number (Fig. 2c). The authors estimated the conditions for which fluid mixing occurred in their experiments and introduced a new dimensionless number defined as,

$$P = \frac{\eta U}{(g\Delta\rho ab/\pi)} \quad (22)$$

where  $\eta$  is the viscosity,  $U$  is the flow velocity,  $g$  is the acceleration of gravity,  $\Delta\rho$  is the density difference between the two liquids, and  $a$  and  $b$  are base dimensions of their apparatus. When  $P < 0.1$ , the two liquids were gravitationally unstable and mixed in the pocket, whereas, when  $P > 0.1$ , the annular flow of the two liquid remained undisturbed.

The role of crystals settling and mush remobilization on magma mixing was also examined in laboratory studies. Renggli et al. (2016) presented high-temperature experiments in which a platinum sphere was poured on top of a layer of natural rhyolite glass held above a layer of natural basalt glass. The platinum sphere entrained some of the rhyolitic material into the basaltic layer as a long filament that ended up to rise buoyantly up to the initial rhyolitic-basaltic interface where it formed a large layer of hybrid material (Fig. 2d). The results revealed that the movement of settling crystals can cause an increase in local mingling at the rhyolitic-basaltic interface in a magma chamber. Girard and Stix (2009)

showed that the presence of a basal crystal mush can affect the rise of a rhyolitic magma injection into a rhyolitic magma chamber. Their experiments consisted in injecting upwards at low Reynolds number ( $Re < 10$ ) corn syrup in a tank containing corn syrup with a basal mush layer made of a mix of aqueous corn syrup solution and particles. In spite of the low density contrast between the injection and ambient fluids, an initial plume formed, followed by a steady-state column that carried some of the mush particles (up to 12.5%) to the top of the reservoir (Fig. 2e). These experiments highlighted the possibility for a replenishing melt to remobilize crystal mush over relatively short timescales.

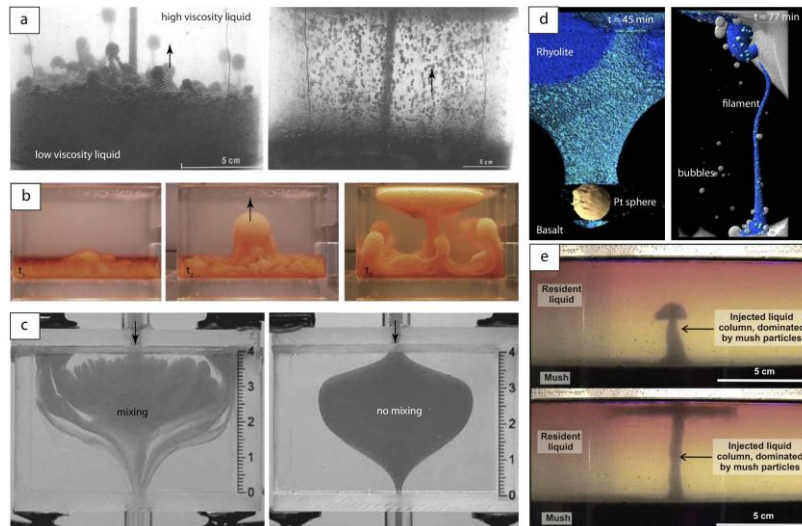


**Figure 2.** Laboratory experiments on magma mixing. (a) Two dynamical regimes of the gas-driven mixing experiments - *left*: unstable bubble foam layer, and *right*: rise of individual bubbles (modified from Thomas et al. 1993). (b) Time-series of a gas-driven mixing experiment generated by decompression (modified from Woods and Cowan 2009). (c) Two experiments illustrating the mixing of two fluids in a pocket (modified from Sato and Sato 2009). (d) X-ray microCT images of two particle-driven magma mixing experiments (modified from Renggli et al. 2016). (e) Crystal mush experiments at early (*top*) and late (*bottom*) stages of the basal injection (modified from Girard and Stix 2009).

Natural convection driven by the rise of buoyant residual liquid into an overlying magma has long been recognized as a major mechanism to produce extensive mixing in magma chambers. Jellinek et al. (1999) and Jellinek and Kerr (1999) conducted laboratory experiments to understand the conditions under which convection can produce extensive mixing or not. In a first series of experiments, a block of frozen polyethylene glycol (PEG) wax was suspended above a layer of hot water or polymer sodium carboxymethyl cellulose (CMC). The hot fluid melted the wax block to form a dense melt layer that grew until it became unstable and drained downward in several plumes. In a second series of experiments, water or aqueous solutions of glucose and/or glycerol were pumped from a lower reservoir through a porous plate into the base of denser layers of glucose or aqueous solutions of glucose,  $K_2CO_3$ , or glycerol. The experiments were made at low and high Reynolds number ( $Re \sim 10^1$ - $10^4$ ), high compositional Rayleigh number ( $Ra \sim 10^{11}$ - $10^{16}$ ), and high Schmidt number ( $Sc = Pe/Re \sim 10^3$ - $10^7$ ). The mixing efficiency was found to depend on two parameters: a Reynolds number based on the thickness of the liquid layer, and the ratio of the ambient liquid kinetic viscosity to the plume liquid kinetic viscosity ( $U^*$ ). At small values of  $Re$  and  $U^*$ , an unstable boundary layer formed at the base of the ambient layer fluid and produced a field of sheet plumes that underwent meandering instabilities causing the plumes to collide and become entangled. The amount of entrainment of ambient fluid was relatively important, which resulted in the nearly complete mixing of the two layers at the end of the experiment. In the small- $Re$  and large- $U^*$  experiments, the input fluid also formed an unstable boundary layer but the rising plumes generated by the Rayleigh-Taylor instability entrained a negligible amount of ambient fluid, resulting in very limited mixing between the two layers. At the end of the experiments, the input fluid had ponded as a separate layer above the ambient fluid (Fig. 3a). At large values of  $Re$  and low values of  $U^*$ , the input fluid produced a field of narrowly spaced sheet plumes that entrained ambient fluid efficiently, resulting in rapid and nearly complete mixing of the two layers. In the large- $Re$  and large-

$U^*$  experiments, a field of axisymmetric plumes rose a short distance from the boundary before meandering instabilities developed, resulting also in rapid and nearly complete mixing of the two layers (Fig 3a). The results clearly showed that the extent to which convection led to either mixing or stratification was determined by the magnitude of  $Re$  and  $U^*$ , which imposed the strength of the resultant large-scale circulation in the chamber. The effect of phenocrysts on convection was investigated experimentally by Koyaguchi et al. (1993) who heated from below suspensions of silicon carbide grit in water or glycerine solutions. The experiments were made at high Rayleigh number ( $Ra \sim 10^8$ - $10^9$ ) and high Prandtl number ( $Pr \sim 10^4$ ). At low particle concentration, highly time-dependent convection was observed in the tank and the particles were uniformly distributed due to turbulent convection. The change of particle concentration with time was found to be consistent with the experiments of Martin and Nokes (1988) who used mixtures of round polystyrene beads and water with NaCl and CMC under similar conditions at high Rayleigh number ( $Ra \sim 10^7$ - $10^9$ ), high Prandtl number ( $Pr \sim 10^0$ - $10^4$ ), and low stability number ( $\Sigma = 10^{-2}$ - $10^{-1}$ ). At higher particle concentration, turbulent convection was suppressed at an early stage and mostly confined to a sedimenting layer separated from an upper clear layer. Heating at the base led to a decrease in the bulk density of the lower layer which overturned rapidly (Fig. 3b). In a second series of experiments cooled from above, a critical particle concentration was found to separate a regime of continuous overturn from a regime of no overturn at all. These results were found in excellent agreement with theoretical predictions for the time evolution of the bulk temperature, concentration and height of the interface, and confirmed that the presence of particles can significantly influence the mode of convection. Hort et al. (1999) explored the interaction of convection and crystallization in a binary phase system by using a water-isopropanol solution cooled from above. After an initial period of high-temperature turbulent convection removing the superheat, the bulk fluid remained steady at the liquidus temperature. The composition of the bulk fluid remained constant throughout the crystallization until arrival of a mush front. Convection then became non-turbulent, only driven by unwanted sidewall effects that prevented convection to stop upon loss of superheat.

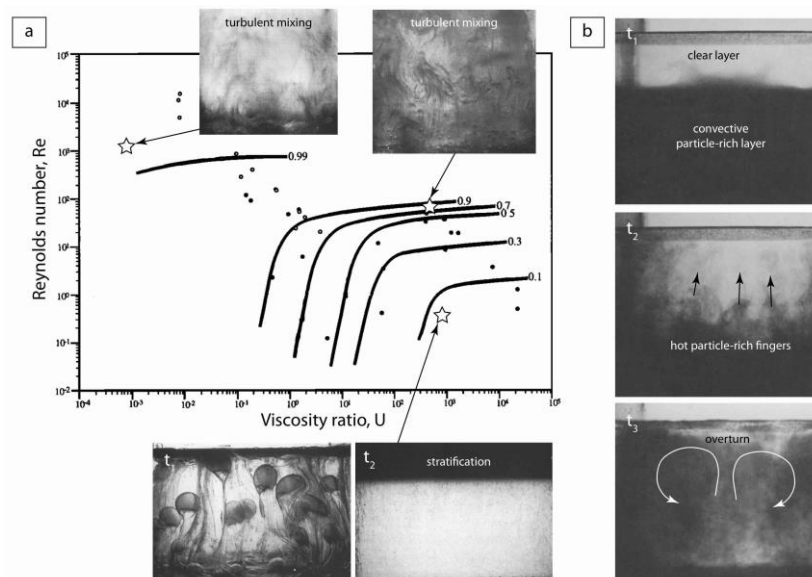


**Figure 3.** Laboratory experiments on convection in magma chambers. (a) Regime diagram illustrating how the mixing efficiency ( $E$ ) varies as a function of  $Re$  and  $U^*$ . Circles correspond to laboratory experiments. Photographs are taken from three different experiments (modified from Jellinek et al. 1999). (b) Photographs showing the overturn of a sedimenting layer heated from below at three different times  $t_1 < t_2 < t_3$  (modified from Koyaguchi et al. 1993).

The input of a hot basaltic magma can result in the melting of the roof, floor and walls of the magma chamber, which may affect convection and mixing. Huppert and Sparks (1988b) investigated experimentally the fluid dynamical and heat transfer processes during roof melting by introducing quickly a hot aqueous solution of salt beneath a roof of PEG wax or ice that started to melt. In the case where the density of the melt exceeded the density of the underlying liquid layer, the melt initially sank

but the turbulent motion resulting from the heat transfer to the cold roof quickly mixed the molten fluid into the ambient fluid (Fig. 4a). In the case where the density of the melt was smaller than the density of the ambient fluid, a separate layer formed between the roof and the fluid (Fig. 4a). The experimental results were fully captured by a theoretical model for the time evolution of the bulk temperature and melt thickness. Huppert and Sparks (1988a) extended this work to the case of basaltic intrusions into the continental crust and showed that the second regime was expected to occur because the magma produced by melting of the roof rocks was lighter than the magma below. Consequently, the melted material was expected to remain at the top of the chamber and to be chemically isolated from the basaltic magma at the bottom. This phenomenon was also observed by Campbell and Turner (1987) who performed similar experiments using a hot aqueous solution of  $\text{Na}_2\text{CO}_3$  or  $\text{KNO}_3$  to melt a roof made of  $\text{Na}_2\text{CO}_3$  and ice. Kaneko and Koyaguchi (2000) investigated the situation where a hot magma simultaneously crystallized and melted both the floor and the roof of a magma chamber by using a hot solution and cold solid mixtures in the  $\text{NH}_4\text{Cl-H}_2\text{O}$  binary eutectic system. The experiments were made at high Rayleigh number ( $\text{Ra} \sim 10^9$ ), low Prandtl number ( $\text{Pr} \sim 5$ ), high Lewis number ( $\text{Le} = \text{Sc}/\text{Pr} \sim 10^2$ ), and low Stefan number ( $\sigma \sim 2$ ), the latter being the ratio of the heat required to melt a solid to the heat available to cause melting. The experiments gave results similar to those of Huppert and Sparks (1988a,b) and Campbell and Turner (1987) when only floor melting was simulated. However, in the experiments where both roof and floor melting were addressed, thermal convection driven by cooling at the roof and compositional convection driven by melting and crystallization at the floor occurred simultaneously in the solution. Crystallization of the liquid led to the formation of a mushy layer at the floor but the heat flux accompanied with compositional convection at the floor was very limited. The formation of a stabilizing compositional gradient and an unstable temperature gradient in the solution promoted the formation of double-diffusive convective layers (Fig. 4b). The results clearly showed that floor melting did not always enhance the cooling of the solution, but instead reduced the total heat loss by suppressing convection in the solution. Kaneko and Koyaguchi (2004) later explored the mechanisms controlling the formation of a mushy layer in their experiments when only floor melting was simulated, and they quantified its impact on the degree of mixing in the solution. The results showed that the mushy layer formed due to simultaneous crystallization of the liquid and partial melting of the solid. Convective exchanges were observed between the interstitial liquid of the partially molten solid layer and the overlying liquid but mixing was relatively limited. Leitch (2004) explored the effects of roof and walls melting by injecting a hot, dense aqueous solution of  $\text{NaNO}_3$  or  $\text{FeSO}_4$  at the base of a cavity with a roof and walls made of aqueous ice or cold PEG wax. The experiments were made at low Reynolds number ( $\text{Re} \sim 10^{-3}$ - $10^{-1}$ ), high Rayleigh number ( $\text{Ra} \sim 10^6$ - $10^9$ ), high Prandtl number ( $\text{Pr} \sim 10^0$ - $10^3$ ), high Lewis number ( $\text{Le} \sim 10^2$ ), and low Stefan number ( $\sigma \sim 10^{-1}$ - $10^0$ ). The results showed that the walls melted quickly and formed a layer of wall melt beneath the roof that impeded heat transfer and roof melting. Convection and mixing in the solution was therefore strongly affected by walls melting. Shibano et al. (2012) investigated the extreme case of liquid migration in a crystalline magma chamber. The experiments consisted of placing a thin silicon oil layer at the base of a thick granular layer made of glass beads and silicone oil (Fig. 4c). In this configuration, the particles at the base of the granular medium quickly became gravitationally unstable and detached to form downwelling plumes, which drove a cellular convection in the basal liquid-rich layer. This convection eroded the granular layer, allowing the basal layer to migrate upwards. By repeating this process, the liquid-rich layer migrated upwards within the granular medium. These observations shed some light on an efficient mechanism to disintegrate the jammed crystals and transport melt in a crystalline magma chamber.

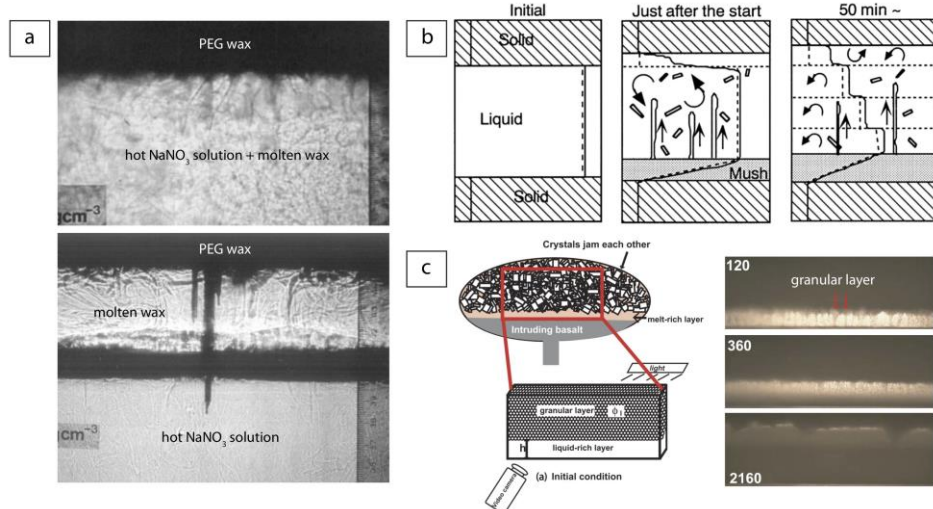


**Figure 4.** Laboratory experiments on liquid transport by rock melting. (a) Photographs of two roof melting experiments in which the melt mixed with the lower hot layer (*top*) or formed a separate layer (*bottom*) (modified from Huppert and Sparks 1988a,b). (b) Sketches of temperature and compositional profiles in a laboratory experiment of roof and floor melting at three different times (modified from Kaneko and Koyaguchi 2000). (c) (*left*) Sketch of experiment on liquid migration in a crystalline magma chamber, and (*right*) photographs illustrating the rise of a liquid-rich layer through an upper granular medium at three different times given in seconds (modified from Shibano et al. 2012).

A few laboratory experiments were designed to investigate how magma chamber dynamics may influence the style of an eruption at the surface. Jaupart and Vergnolle (1988, 1989) simulated the recharge of a magma chamber by a source of gas bubbles. For this, they injected large bubbles distributed over the base of a tank containing either silicon oil or glycerol solutions. Gas bubbles rose through the liquid and remained trapped at the reservoir roof, where they accumulated and coalesced in a foam layer. This foam periodically collapsed into gas pockets, which erupted into a conduit following three dynamical regimes determining eruption behavior (Fig. 5a). In the first regime, the foam remained stable and the bubbly mixture ascended into the conduit, which reproduced the behavior of effusive eruptions. In the second regime, alternating foam build-up and collapse led to the (fire-fountaining) eruption of a single, large gas pocket. In the last regime, the foam became unstable and developed large slugs of gas leading to intermittent slug flow in the conduit, a behavior that could explain the discrete explosions of Strombolian eruptions. The authors proposed a theory to explain the first two regimes that was found in good agreement with their experimental observations. A remarkable result from this analysis was that the foam at the top of the magma chamber collapsed above a critical thickness determined by the liquid viscosity and the gas flux. In a different context, Namiki et al. (2016) examined experimentally to what extent large earthquakes can activate volcanic eruptions. The experiments consisted of shaking a tank containing a foam layer overlying a liquid layer made of glucose syrup solutions. During the shaking, a surface wave appeared and the interface between the liquid layer and the foam layer sloshed until the foam collapsed and mixed with the underlying layer (Fig. 5b). The experiments allowed the authors to build a scaling law and apply these results to the natural case. The authors concluded that the gas released from the collapsed foam may cause a magmatic Strombolian eruption, while the overturn in the magma reservoir may provide new nucleation sites that can help to prepare a future eruption. Kennedy et al. (2008) investigated the catastrophic case of a caldera-forming eruption by looking at the coupled dynamics of chamber roof subsidence and magma flow. The experiments consisted of dropping a cylindrical block into a tank containing aqueous corn-syrup solutions in order to measure the velocity fields around the block. The results showed that the block subsidence led to complicated and vigorous liquid stirring and mixing in the tank depending on the Reynolds number ( $Re$ ), and two geometric parameters referred as the tilt ( $Ti$  = ratio of the horizontal distance between the block and the chamber wall to the chamber depth) and subsidence number ( $Su$  = ratio of the block width to the liquid magma chamber thickness) (Fig. 5c). These parameters fully controlled the style of subsidence and helped to

provide a framework to explain textural, petrological and geochemical variation in deposits associated with caldera-forming eruptions.

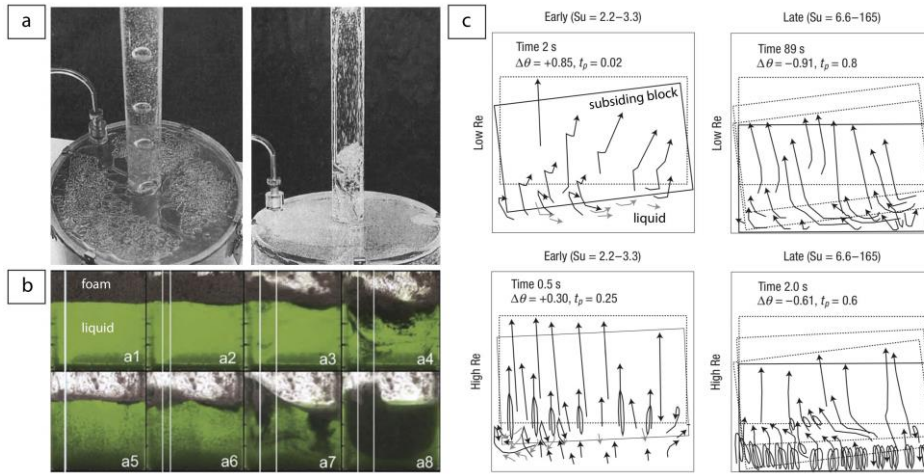


**Figure 5.** Laboratory results on the influence of magma chamber dynamics on the eruptive style. (a) Strombolian (*left*) and fire fountaining regimes (*right*) observed when a magma chamber is recharged by gas bubbles (modified from Jaupart and Vergnolle 1988). (b) Time series of a foam collapse and mixing during a shaking tank experiment (modified from Namiki et al. 2016). (c) Dynamical regimes observed for low and high Re and Su numbers during the block subsidence experiments (modified from Kennedy et al. 2008).

### 3.2 Magma intrusions: dykes and sills

The dynamics of fluid-filled fractures such as dykes and sills depends fundamentally on the buoyancy of the intrusion, due to the density difference between the fluid and the surrounding solid, and on the mechanical properties of the host medium (Tait and Taisne 2013, Gonnermann and Taisne 2015). As described below, experiments on intrusions are good examples of the use of dimensionless numbers for mapping physical regimes. Analogue magmas are fluids (gas or liquid) whereas analogue host rocks are either (visco)elastic solids or granular brittle materials (Table S1, Supplementary material). Gelatin has been widely used since earlier works (e.g. Fiske and Jackson 1972) because it is a transparent brittle viscoelastic solid, which allows for direct observation of the fractures in three dimensions and as such provides an ideal complement to two-dimensional theoretical analysis, and its elastic parameters (Poisson's ratio, Young's and shear moduli) are generally well-known. Relatively high fracture resistance at crack tip in gelatin, however, poses scaling issues as it causes deformation and opening-length ratio larger than that in natural rocks, and hence may make quantitative extrapolation of experimental results to nature uncertain (Takada 1990, Kavanagh et al. 2013).

#### 3.2.1 Intrusion dynamics

The fundamental dynamics of experimental buoyant intrusions (or cracks) were investigated by Takada (1990) who used gelatin and various fluids as the analogue host rock and magmas, respectively, to investigate the shape and the velocity of the cracks (Fig. 6a). The fluid was injected with a syringe either in gelatin without or with a preexisting fracture formed by an air-filled crack. Transient fluid injection caused isolated cracks whereas continuous injection led to cracks growing continuously from their source point. Crack segmentation occurred when a critical volume of injected fluid was reached. Takada (1990) identified scaling laws for the morphology and the kinematics of isolated cracks, which confirmed the theoretical prediction that cracks growth and propagation were controlled fundamentally by buoyancy ( $\Delta\rho g$ ). The ratio of the crack width (or thickness),  $w$ , over the crack height,  $h$ , was given by

$$\frac{w}{h} = k_1 \Delta\rho g h, \quad (23)$$

where  $k_l$  depended on the fluid used. The ratio of the crack length ( $l$ ) over its height, which could not be predicted by the two-dimensional elastic theory, increased with  $h$  as

$$\frac{l}{h} = \frac{(h-h_0)}{\beta h}, \quad (24)$$

with  $h_0$  the height of the crack tail and  $\beta$  an empirical constant. Note that  $l/h$  rather decreased with  $h$  in case of preexisting fractures. The ascending velocity of isolated cracks was

$$U_c = k_2(\Delta\rho g)^3 h^4 = k_3 \Delta\rho g w^2. \quad (25)$$

Takada (1990) pointed out scaling issues because this velocity was significantly smaller than that predicted by theory, possibly because of a ductile behavior at the crack tip. Finally, the height and the length of the growing cracks increased with time,  $t$ , according to

$$h, l = cQ^{1/3} t^{4/9}, \quad (26)$$

with  $c$  a constant and  $Q$  the injection rate.

In nature, dyke dynamics may be controlled by volatiles that exsolve from the magma and accumulate at the tip. Menand and Tait (2001) addressed this issue in experiments in which air was continuously injected into a liquid-filled crack after the latter began to propagate in gelatin. The air extracted itself from the liquid and formed a gas pocket at the crack tip. The pocket grew with time and controlled the velocity of the crack tip once it was sufficiently buoyant to overcome the fracture resistance of the gelatin. The crack velocity was proportional to the square of the air bubble height ( $h_b$ ) whatever the injection rate of air,

$$U_c = c_v h_b^2, \quad (27)$$

where  $c_v$  was a constant proper to a fluid of a given viscosity. Menand and Tait (2001) proposed that the critical height required for the air bubble to fracture the gelatin was

$$h_{b,c} = \left( \frac{4K}{3\rho_g g} \sqrt{\frac{2}{\pi}} \right)^{2/3}, \quad (28)$$

with  $K$  and  $\rho_g$  the fracture toughness and the density of the gelatin, respectively. These results help to better understand the phenomenology and the timing of the precursory activity of some volcanic eruptions.

Several mechanisms may hamper the propagation of magma intrusions, which may eventually come to halt. Taisne and Tait (2009) showed that dyke arrest could be caused by a static mechanical equilibrium because of a three-dimensional effect. In their experiments, constant volume liquid-filled cracks in gelatin stopped when horizontal cracking required for vertical propagation could no longer occur as the crack thinned progressively. They identified scaling laws for the final length and breadth of cracks as a function of a governing dimensionless number

$$K^* = \frac{K}{\Delta\rho g V^{1/2}}, \quad (29)$$

with  $\Delta\rho g$  the buoyancy pressure gradient and  $V$  the volume of liquid in the crack. Values of  $K^*$  in the experiments were close to that estimated for natural cases and suggested good dynamic similarity between both systems. Equation 29 shows that the volume of fluid in the experimental crack is the key factor since other parameters are constant. Considering the buoyancy length, i.e. the minimum length required for buoyancy effect to cause fracturation in a two-dimensional geometry,

$$L_b = \left( \frac{K}{\Delta\rho g} \right)^{2/3}, \quad (30)$$

Taisne and Tait (2009) identified scaling laws for the final crack length ( $L_f$ ) and breadth ( $B_f$ )

$$\frac{L_f}{L_b} \sim 54 K^{*-3/2} \quad \frac{B_f}{L_b} \sim 5 K^{*-5/6}. \quad (31)$$

Combining equations 29-31 gives

$$L_f = 54 \frac{V^{3/4}}{L_b^{5/4}}, \quad (32)$$

which shows that a dyke from a magma reservoir at given depth (i.e.  $L_f$ ) will lead to an eruption at surface only if it contains a critical volume of magma.

Magma solidification in fractures caused by cooling is another mechanism that contributes to stop intrusions. Taisne and Tait (2011) addressed this issue by using a fluid with a temperature-dependent rheology (see also Galland et al. 2006). The viscosity increased due to cooling, and the fluid eventually solidified when its temperature was below that of the phase change. An important result was that cooling caused intermittent propagation of a fracture even at constant injection rate. After a pause,

the crack swelled and then grew again either at the top or at the margins. Taisne and Tait (2011) proposed that the intrusion dynamics could be described by a dimensionless temperature (varying from 0 to 1)

$$\Theta = \frac{T_s - T_\infty}{T_m - T_\infty} \quad (33)$$

and a dimensionless flux (varying from 0 to  $\infty$ )

$$\Phi = \frac{3Q\Delta\rho g}{2\kappa E}, \quad (34)$$

with  $T_s$  the solidification temperature,  $T_\infty$  the temperature of the host medium,  $T_m$  the temperature of the injected fluid,  $Q$  the volumetric injection rate,  $\Delta\rho g$  the fluid buoyancy,  $\kappa$  the thermal diffusivity, and  $E$  the Young's modulus. They argued that intrusions could experience intermittent propagation and stop as both  $\Theta$  increase to 1 (i.e. hot intrusions) and  $\Phi$  decrease to zero (i.e. slow intrusions). Chanceaux and Menand (2014, 2016) built on these findings to investigate to effect of solidification on sill propagation, using two layers of gelatin of different stiffness to promote sill formation. Chanceaux and Menand (2014) scaled their experiments according to the procedure of Kavanagh et al. (2013) and injected the fluid vertically at the base of the lower, less stiff silicone layer. They found four distinct regimes depending on both  $\Theta$  and  $\Phi$  (Fig. 6b). When solidification effects were negligible, the analogue dyke passed through the interface between the gelatin layers because of the constant input of hot fluid at the dyke tip. When these effects increased, the dyke spread at the interface and formed a sill, and solidification stopped the dyke at the interface. For extreme solidification effects the intrusion did not propagate. Further experiments by Chanceaux and Menand (2016) focused on the dynamics and morphology of sills generated by injecting directly the fluid at the interface. The intrusions propagated continuously and had a regular and smooth surface at small solidification effects whereas they grew incrementally and formed lobes with irregular surface structures when solidification was dominant.

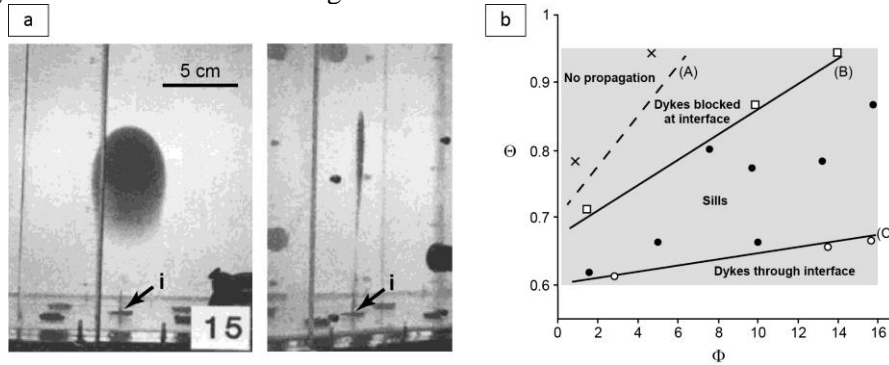


**Figure 6.** Experiments on intrusion dynamics. (a) Buoyant crack generated by injection of a fluid by a syringe at a point source (i), shown in front (*left*) and side (*right*) views. From Takada (1990). (b) Regimes of experimental intrusions as a function of the dimensionless temperature  $\Theta$  and the dimensionless flux  $\Phi$  given by equations 33-34 (the gray area corresponds to natural ranges of values). Lines (B) and (C) indicate respectively  $\Theta=0.0039\Phi+0.61$  and  $\Theta=0.019\Phi+0.68$ . From Chanceaux and Menand (2014).

### 3.2.2 Influence of the host medium

The orientation of the stress field in the host medium is fundamental in controlling the emplacement of intrusions since these propagate respectively parallel and perpendicular to the directions of the maximum ( $\sigma_1$ ) and minimum ( $\sigma_3$ ) principal stresses. Hence various tectonic settings and loading conditions may lead to a variety of intrusions dynamics and orientations. Menand et al. (2010) investigated how a compressive environment may control the propagation of vertical dykes. They generated vertical cracks by injecting air in homogeneous gelatin subjected to a compressive stress field with  $\sigma_1$  horizontal and  $\sigma_3$  vertical. The lateral deviatoric compressive stress was generated by inserting plastic sheets between the gelatine and the lateral walls of the container. The experiments showed that a vertical fracture reached the surface when the compressive stress was small or the buoyancy force was high. In contrast, a weakly buoyant fracture responded to a large compressive stress field by adjusting its trajectory and it became a sill. A dimensional analysis showed that the vertical distance,  $d_c$ , traveled by the crack before it became a horizontal fracture depended on two dimensionless numbers

$$\Pi_1 = \frac{d_c}{h_0}, \quad \Pi_2 = \frac{\Delta\rho g h_0}{\sigma_1}, \quad (35)$$

so that  $\text{Ln}(\Pi_1) \sim 0.36 + 0.1\Pi_2$ , with  $h_0$  and  $\Delta\rho g$  the initial height and buoyancy of the crack, and further algebra gave

$$d_c \sim 1.4h_0 \exp\left(0.1 \frac{\Delta\rho g h_0}{\sigma_1}\right). \quad (36)$$

Application to natural cases shows that  $d_c$  is typically of several kilometers, and crustal heterogeneities distributed at smaller length scales are likely to control the formation of sills.

The effect of an extensional regime on the propagation of successive dykes was studied by Daniels and Menand (2015). The device involved a lower layer of gelatin overlain by a more rigid upper layer of the same material, which forced the analogue dykes to propagate laterally within the lower layer, and uniform extension was simulated by compressing the gelatine vertically and allowing it to deform horizontally. Vegetable oil was injected successively in the gelatin at regular spacing and the initial fractures were parallel to  $\sigma_1$  and perpendicular to  $\sigma_3$ . The experiments revealed that the initial stress field was modified by an intrusion, and in consequence later intrusions were diverted from their initial direction. A scaling analysis showed that the rotation angle between two successive intrusions (measured in plan view) depended on the following dimensionless numbers,

$$N_1 = \frac{\sigma_3}{P_0}, \quad N_2 = \frac{d_s}{h_i}, \quad (37)$$

where  $P_0$  was the fluid overpressure of the first injection (before the extensional regime was imposed),  $d_s$  was the injection spacing of the intrusions, and  $h_i$  was the half-height of the first intrusion. Experimental results were in fairly good agreement with theory, and application of the scaling law to the Red Sea rift indicated dykes interdistance of a few kilometers.

Experimental works have also given insights into the effect of the load generated by a volcanic edifice on the ascent of dykes and on the spatial distribution of eruptive vents. Muller et al. (2001) and Watanabe et al. (2002) imposed a local surface load by placing a rigid object on top of a gelatin layer, which modified the original hydrostatic stress field, and they injected a fluid at the base of a gelatin layer at a given distance from the vertical axis beneath the object (Fig. 7a). Both studies showed that the analogue dykes were attracted by the surface load. The cracks were deflected during ascent according to the local stress field imposed by the load and they became parallel to  $\sigma_1$  and perpendicular to  $\sigma_3$ . Muller et al. (2001) generated buoyant air-filled cracks and found that the maximum distance for which fractures were attracted,  $x_c$ , scaled by the load half width,  $l$ , was controlled by the ratio of the average load stress,  $P_l$ , over the driving pressure at mid-height of the fracture head,  $\Delta P_m$ , so that

$$\frac{x_c}{l} = 0.86 \frac{P_l}{\Delta P_m} + 1. \quad (38)$$

Application to natural cases suggested that dykes can converge to volcanic edifices over lateral distances equal to several times the load width. Watanabe et al. (2002) rather used silicone oil as the analogue magma to generate fractures whose internal pressure was controlled by the volume of liquid. They found that the fractures propagated towards the surface load at a decreasing velocity and stopped, and that deflection occurred if the ratio of the shear stress on the fracture plane over the liquid overpressure was larger than 0.2. Kervyn et al. (2009) further investigated the effect of an edifice load, simulated by a granular cone, when intrusions were generated beneath it (Fig. 7b). The analogue dykes decelerated while approaching the load and were stopped by the load compressive stress. As the intrusions were forced then fluid overpressure increased and modified the local stress field, and the dykes extended first laterally and then vertically. The dykes erupted at the base or in the flank of the granular cone depending on the thickness of the substratum, the slope of the cone and the dyke overpressure. This mechanism may explain the presence of vents away from a central conduit at many volcanoes.

Mechanical heterogeneity of the crust, caused by preexisting fractures or variation of elastic parameters due to a temperature gradient, is another factor that may control the emplacement of magma intrusions. Le Corvec et al. (2013) showed that a buoyant air-filled crack in gelatin propagated toward a pre-existing fracture if the dimensionless distance between them,  $d/L_b$  (with  $L_b = (K/\Delta\rho g)^{2/3}$  the buoyancy length scale and  $K$  the fracture toughness) was less than  $\sim 0.4$ . When the crack propagated between two parallel fractures, deflection towards one of them occurred if the dimensionless distance between the fractures,  $d'/L_b$ , was less than  $\sim 0.8$ , and the angle of inclination of the fractures had a minor effect. A scaling analysis suggested that interactions in nature were likely to occur if dykes and fractures were less than  $\sim 200$  m apart. Rivalta et al. (2005) found that air-filled cracks passing from a stiff to a

compliant medium accelerated and acquired a larger head, before they recovered the shape typical of intrusions in a homogeneous medium. In contrast, the cracks decelerated while approaching a stiffer medium and they came to halt beneath the interface unless additional air injection enlarged the crack and caused propagation into the upper layer. At very high rigidity contrast (ratio of shear moduli of 7.5), however, the fracture could not propagate into the upper layer and it grew horizontally below the interface to form a sill. Kavanagh et al. (2006) further showed that different types of intrusions were generated depending on a dimensionless rigidity (ratio of Young's modulus of upper and lower gelatin layers) and a dimensionless pressure (ratio of fluid overpressure over rock strength) (Fig. 7c). In agreement with Rivalta et al. (2005) they found that an analogue dyke could propagate through the interface and into a less stiff upper layer, irrespective of the pressure ratio, but it was stopped by a more rigid layer. Continuous intrusion in the latter case, however, led to either (i) a hybrid structure consisting of a sill at the interface and a dyke into the upper layer at moderate rigidity and pressure ratios or (ii) a pure sill at higher ratios. In complementary experiments, Kavanagh et al. (2015) varied the strength of the interface by controlling the amount of welding through the temperature of the initial gelatin-water solution of the upper layer. Qualitatively, sill-like and hybrid intrusions typical of high rigidity ratios formed if the interface was weak, otherwise the intrusion was stopped.

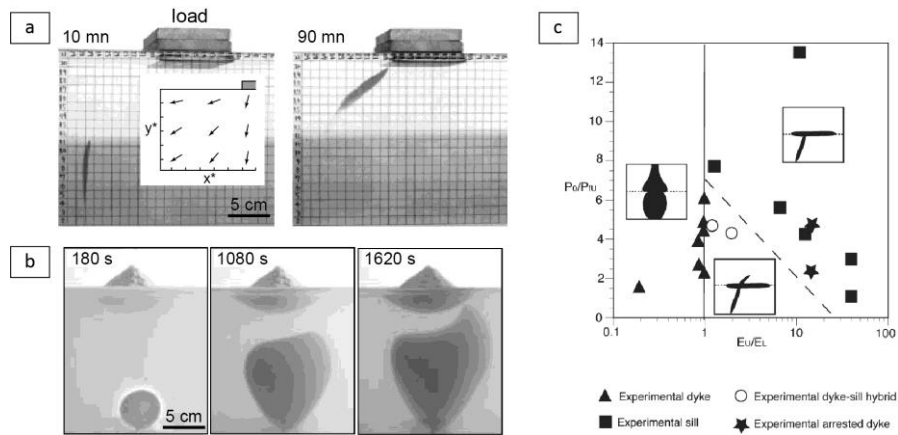


**Figure 7.** Effect of boundary conditions on intrusion dynamics. (a) Deflection of an experimental crack due to a surface load. The inset shows the half-space analytical solution of the orientation of the maximum deviatoric compressive stress (arrows) generated by the surface load, with  $x^*$  and  $y^*$  as normalized length. From Watanabe et al. (2002). (b) Water-filled intrusion into gelatin overlain by a granular cone. Kervyn et al. (2009). (c) Intrusions morphologies in experiments involving a mechanical interface, as a function of the dimensionless pressure (fluid overpressure over rock strength,  $P_0/P_{fl}$ ) and rigidity (ratio of Young modulus of lower and upper layers,  $E_U/E_L$ ). In Kavanagh et al. (2006).

### 3.2.3 Dyke-dyke interaction

Experimental studies have shown that dykes interaction can modify the surrounding stress field and induce dyke rotation and coalescence. Takada (1994) found that buoyancy-driven cracks coalesced more easily than pressure-driven cracks, and that coalescence decreased the local compressive stress field. Ito and Martel (2002) identified scaling laws for the critical horizontal distance between two parallel vertical cracks,  $x_{ci}$ , required for intersection. In their experiments a first crack filled with hexane (A) ascended slowly at  $\sim 10^{-4}$  m/s owing to its low buoyancy, and a later air-filled crack (B) ascended about ten times faster, curved toward crack A and finally intersected it (Fig. 8). A scaling analysis showed that the parameters controlling  $x_{ci}$  were the dykes driving pressures ( $P_A$  and  $P_B$ , controlled by the volume of buoyant fluid injected) and dyke head ( $L_A$  and  $L_B$ , Fig. 8a), so that

$$\frac{x_{ci}}{L_A} = c \left( \frac{P_A}{P_B} \right)^n \left( \frac{L_A}{L_B} \right)^m, \quad (39)$$

where  $c$ ,  $n$ , and  $m$  were empirical constants and exponents whose exact values depended on the crack conditions (i.e. pressure or buoyancy-driven). Notice that  $P_A/P_B$  and  $L_A/L_B$  varied simultaneously owing to the experimental configuration. In similar experiments, Watanabe et al. (2002) showed that a crack

was deflected when the ratio of the shear stress (generated by the crack) over the fluid pressure in the neighboring fracture was larger than 0.2.

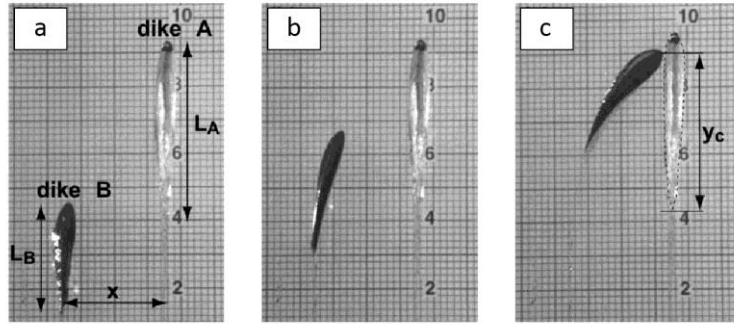


**Figure 8.** Interaction of experimental buoyant cracks initially parallel to each other. Analog dyke B curves toward and finally intersect dyke A at height  $y_c$ . Ito and Martel (2002).

### 3.2.4 Dykes from or into magma chambers

Dykes commonly originate from pressurized magma chambers. McLeod and Tait (1999) investigated dyke nucleation from pre-existing liquid-filled cracks at the margins of a rounded reservoir in experiments aimed to test a theoretical model. Flow of the liquid from the reservoir into the cracks caused pressurization, which promoted failure at the tip of one of the cracks that propagated and acquired a disc-cone hybrid morphology. At given initial reservoir overpressure the rate of pressurization decreased with the fluid viscosity, suggesting that in nature the delays before dyke nucleation may be of hours or years for basaltic or rhyolitic magmas, respectively. Menand and Tait (2002) further showed that analog dyke propagation from a pressurized source occurred in two distinct stages. A crack was driven first by the source overpressure and it grew as a circular disk in a nearly vertical plane at decreasing velocity. Then the buoyancy pressure (cf.  $\Delta\rho$ ) became dominant and the crack (of head length  $l_c$ ) propagated mainly vertically at a constant velocity that scaled with  $\Delta\rho l_c^2$ .

Dykes that do not reach directly the surface may be injected into shallower reservoirs. Hodge et al. (2012) mapped the regimes of deformation of analog intrusions into a reservoir containing a fluid sheared by a rotating plate, which simulated a convective chamber (Fig. 9). They identified three types of structures, resulting from various degrees of interaction between the two fluids, depending on two dimensionless numbers: a so-called Stokes ratio of the time for the growth of the Rayleigh–Taylor instabilities of the injected fluid to the fall time of the intrusion through the sheared fluid,

$$S = \frac{\eta_i R_i}{\eta_a h}, \quad (40)$$

and a ratio of the timescales of lateral stretching and disaggregation of the intruded fluid,

$$Y = \frac{2\pi}{r\Omega} \left( \frac{\tau_y}{\rho_i} \right)^{1/2}, \quad (41)$$

with  $\eta_i$ ,  $\tau_y$ ,  $\rho_i$  the viscosity, the yield strength, and the density of the injected fluid, respectively,  $R_i$  and  $r$  the radius and the radial position of the injection point, respectively,  $\eta_a$  and  $h$  the viscosity and the depth of the ambient fluid, and  $\Omega$  the rotation rate of the tank.

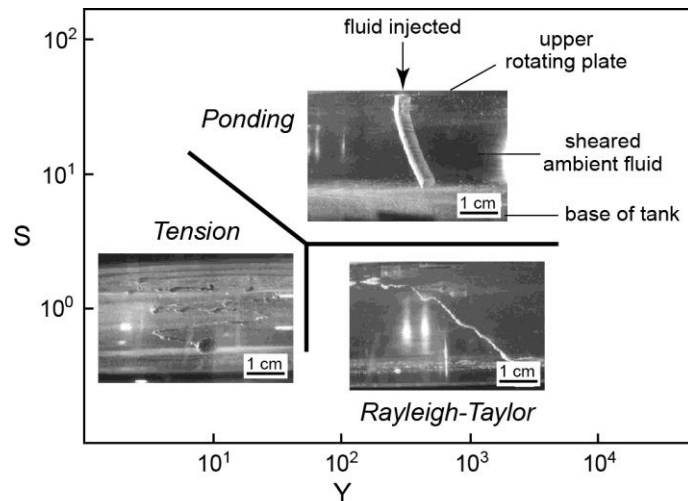


**Figure 9.** Regimes of fluid injections into a less dense sheared fluid as a function of dimensionless numbers  $S$  and  $Y$  (equations 40-41). The intrusion is injected from above and ponds, experiences instabilities (Rayleigh-Taylor regime) or is disaggregated and forms analog enclaves (tension regime). From Hodge et al. (2012).

### 3.3 Conduit flow processes

Physical processes in magmas ascending in conduits control the style and the intensity of volcanic eruptions. In particular, the exolution of volatiles due to decrease of the lithostatic pressure, which promotes gas bubble nucleation and growth, and the mechanical response of the magma as a function of the decompression rate are essential in controlling magma fragmentation (Gonnermann 2015, Cashman and Scheu 2015). Various types of experimental works have been conducted in order to better understand these mechanisms and to elucidate conduit flow regimes. Studies carried out principally since the 1990's have involved natural or analogue materials depending on their principal objectives. The use of natural materials at real pressure and temperature have permitted sometimes experimentalists to overcome scaling issues, but the configuration of most devices also prevented direct observations (see for instance works on decompressed melts saturated in volatiles, e.g. Hurwitz and Navon 1994). In contrast, in experiments with analogue systems key parameters such as the crystal and volatile contents as well as the fluid viscosity could be controlled, and the processes of bubble nucleation and growth could be observed directly (e.g. Phillips et al. 1995).

#### 3.3.1 Bubble nucleation and growth

Since early works (e.g. Murase and Mc Birney 1973, Bagdassarov and Dingwell 1992), experimental studies involving natural materials initially saturated in volatiles have addressed gas bubble formation essentially as a function of the decompression rate. Spontaneous, homogeneous nucleation producing evenly-spaced bubbles was observed in experiments involving crystal-free magmas (mostly rhyolites) saturated with  $H_2O$  and/or  $CO_2$  and decompressed at rates up to  $\sim 10$ - $100$  MPa/s (Mourtada-Bonnefoi and Laporte 1999, 2004, Mangan and Sisson 2000, Hamada et al. 2010). Homogeneous nucleation is a delayed process that results from high degrees of volatiles supersaturation of up to  $\sim 300$  MPa, the latter controlling the surface tension between the critical bubble nuclei and the surrounding melt and hence the nucleation rate and the bubble number density (Gonnermann and Gardner 2013, see Toramaru 1995 and 2006 for theoretical treatment and comparison with experiment). Large supersaturation in experiments suggested that in nature a delayed and homogeneous nucleation event during magma ascent could lead to rapid vesiculation and violent eruption dynamics, even for low viscosity magmas (Rivalta et al. 2013). In nature, however, magmas often contain crystals and microlites that favor the formation of nuclei and lead to heterogeneous nucleation. Experiments with such magmas degassing in equilibrium (at low decompression rates) or not in equilibrium (at high decompression rates) showed that the nucleation sites density and the nucleation rates increased with the microlites content (Hurwitz and Navon 1994, Gardner et al. 1999). Experiments with analogue materials were ideal

complement to those with natural magmas since wider ranges of physical properties could be investigated. For instance, Hammer et al. (1998) could vary the melt viscosity and investigated its influence on critical supersaturations by adjusting the degree of dilution of a corn syrup solution. Rivalta et al. (2013) identified end-member processes as materials with high volatile and low particles contents, which experienced delayed nucleation, could fragment even under low decompression, whereas those with low volatile and high particle contents degassed efficiently and did not fragment.

The growth of gas bubbles from their nuclei results from the combination of the decompression rate of the magma, the diffusion rate of volatiles into the bubbles, and the deformation of the viscous melt around the bubbles. Lensky et al. (2004) did experiments with rhyolitic melts in order to test a theoretical model and they showed that the regime of bubble growth depended on two dimensionless numbers involving the respective timescales of the three above-mentioned processes,

$$\Theta_V = \frac{\tau_v}{\tau^*}, \quad \Theta_D = \frac{\tau_d}{\tau^*}, \quad (42)$$

where  $\tau_v = 4\eta/P_i$  is the viscous timescale,  $\tau_d = d_{bi}^2/D$  is the diffusion timescale, and  $\tau^* = P_i/R$  is the decompression timescale, with  $\eta$  the melt dynamic viscosity,  $P_i$  the initial pressure,  $d_{bi}$  the initial bubble radius,  $D$  the diffusivity, and  $R$  the decompression rate. With these dimensionless numbers Lensky et al. (2004) could map the regimes of bubble growth, which could be used to infer the possible styles of eruptions when natural parameters are known (Fig. 10). Other experiments with analogue materials revealed that the size of the bubbles increased with time to the power  $2/3$ , in agreement with theories assuming that bubble growth depends primarily on the fluid viscosity though the effect of buoyant rise of bubbles may be non negligible (Zhang et al. 1997), and that foam expansion increased with the potential energy that depended on the porosity and amount of decompression (Namiki and Manga 2005, see their equation A.7).

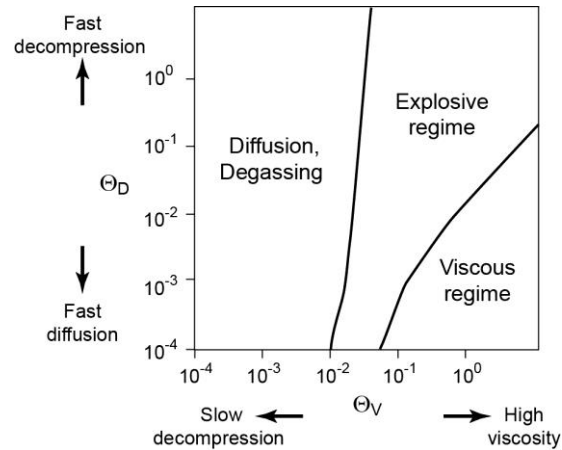


**Figure 10.** Regimes of bubble growth as a function of dimensionless numbers  $\Theta_V$  and  $\Theta_D$  (equations 42). Bubble overpressure and melt supersaturation favor explosive eruptions (transition field) whereas equilibrium-degassing and overpressure growth regime favor effusive eruptions. From Lensky et al. (2004).

### 3.3.2 Magma fragmentation

A vesiculated magma fragments when it is suddenly decompressed and the vesicles explode, when it is sheared at high rates, and/or when its bubbles grow rapidly and coalesce as it is accelerated and stretched (Cashman and Scheu 2015, Gonnermann 2015). The balance between the strain rate of the melt and its rate of structural relaxation defines a continuous range of mechanisms with two end-members, ductile-like melt disruption when viscous stresses can be relaxed, and brittle-like fragmentation when the tensile strength is exceeded (Ichihara 2008, Wadsworth et al. 2018). Laboratory experiments carried out with shock tube devices since the 1990's have investigated these two styles of fragmentation, which generated clast sizes and shapes similar to those in nature (e.g. Zimanowski et al. 1997, Yamamoto et al. 2008, Martel et al. 2000).

Ductile fragmentation was studied in experiments involving analogue liquids, such as water saturated with  $H_2O$  and/or  $CO_2$  or gum rosin acetone solutions, which were stretched upwards as gas

bubbles grew. In seminal works of Mader et al. (1994, 1996) supersaturation of the volatile phase was caused by decompression or by a chemical reaction. The resulting expanding bubbles led to violent acceleration proportional to the degree of supersaturation, which caused severe strain and ductile rupture of the bubble walls, hence creating a heterogeneous foam. Further investigation with CO<sub>2</sub>-saturated water revealed liquid fragmentation whose maximum amount moved down the analogue conduit (Mader et al. 1997, Fig. 11); note that the same phenomenon was observed in experiments of Sugioka and Bursik (1995) involving solid particles immersed in a liquid, and which further revealed that compression caused by a fragmentation front could inhibit bubble growth. Further works showed that the presence of crystals and bubbles facilitated fragmentation, which occurred at lower initial volatile contents and amounts of decompression (Mourtada-Bonnefoi and Mader 2004), and that the foam accelerated constantly (Zhang et al. 1997). In experiments involving Newtonian fluids with viscosities and surface tension similar to those of basaltic magmas Namiki and Manga (2006, 2008) showed that fragmentation occurred at critical Reynolds numbers larger than  $\approx 1$  provided the decompression rate was high enough.

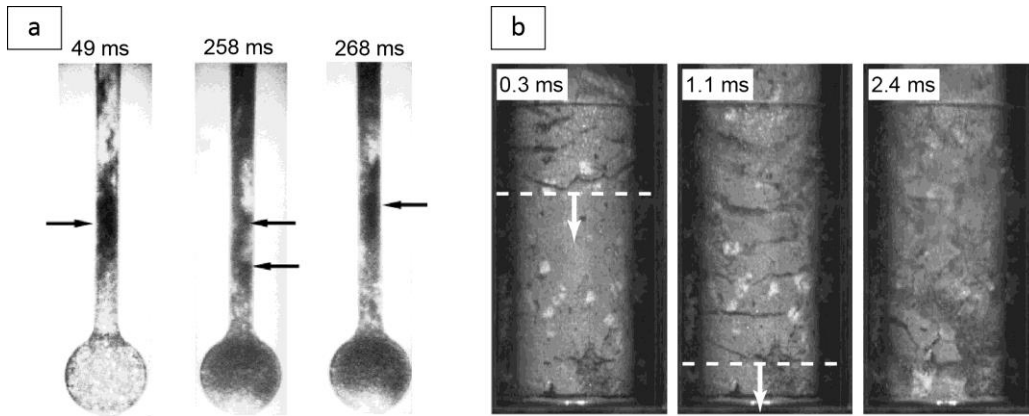


**Figure 11.** Snapshots of shock-tube experiments after onset of decompression. (a) Ductile fragmentation of CO<sub>2</sub>-saturated water, with lower liquid containing bubbles and delimited by a zone of fragmentation (arrow, 49 ms), and later liquid slugs with bubbles (arrows, 258 and 268 ms). From Mader et al. (1997). (b) Brittle fragmentation of a natural rock sample, with downward fragmentation wave. Notice that the vertical edge of the sample is glued to a transparent holder. From Fowler et al. (2010).

Brittle fragmentation favored by rapid decompression of solidified or highly viscous magmas containing overpressurized vesicles was studied using natural samples. Pioneering experiments of Alidibirov and Dingwell (1996), with andesitic to dacitic samples of viscosities  $>10^8$  Pa s at natural temperature and pressure and decompressed at very high rates of 40 MPa/ms, revealed that this style of fragmentation was characterized by a release wave that propagated downward (i.e. according to the pressure gradient) at the speed of sound. Resulting tensile stresses and high gas pressure in the initial vesicles promoted fragmentation, which proceeded sub-parallel to the front wave and generated pyroclasts with grain size distribution and shapes similar to those in nature. In this configuration the speed of the fragmentation front increased up to  $\sim 130$  m/s as either the fragmentation threshold (i.e. pressure drop,  $\Delta P$ ) or the connected porosity,  $\phi_c$ , increased (Spieler et al. 2004a, Taddeucci et al. 2004, Scheu et al. 2006, 2008), and the pyroclasts resulted from breakage of larger blocks formed from primary cracks (Fowler et al. 2010). Brittle fragmentation was controlled fundamentally by the potential energy available (Kueppers et al. 2006b),

$$E=V\phi_c\Delta P, \quad (43)$$

with  $V$  the volume of the sample (notice that the volume dependence may pose scaling issues). In detail,  $\Delta P$  was inversely proportional to  $\phi_c$  (Spieler et al. 2004b, Scheu et al. 2006, 2008) and proportional to the square root of the material permeability, so that

$$\Delta P=\frac{a\sqrt{k}+\sigma_m}{\phi_c}, \quad (44)$$

with  $a$  an empirical constant and  $\sigma_m$  the tensile strength of the porous matrix (Mueller et al. 2008; see also Koyaguchi et al. 2008 for theoretical considerations). Detailed grain size analyses showed that both the fragmentation efficiency, i.e. the amount of fine particles generated, and the fractal dimension of particle size distribution increased with  $E$  (Kueppers et al. 2006a, 2006b). Clasts ejection velocities

indicated that the energy consumed through the creation of new surfaces correlated inversely with  $\phi_c$  and represented 10-15 % of the total energy (Alatorre-Ibargüengoitia et al. 2010, Montanaro et al. 2016). Other experiments with analogue materials suggested that the geometry of the fractures, and hence the size and shape of the particles created, were dependent on the stress field at the time of fragmentation (Dürig and Zimanowski 2012).

Experiments with analogue materials such as silicone polymers, gum rosin and syrups allowed exploring physical parameters (viscosity, porosity, initial pressure, amount and rate of decompression) over ranges commonly larger than in studies with natural samples. They revealed that both ductile and brittle fragmentation could occur during a given decompression event. For instance, Taddeucci et al. (2006) showed that bubble growth was accompanied by fracturing as material expansion was hampered by friction along the margin of the device. Stix and Philipps (2012) reported that samples near the fragmentation threshold, which depended on both the decompression rate and the final pressure with respect to volatile saturation, were disrupted in a ductile fashion. In contrast, samples subjected to decompression significantly higher than this threshold fragmented in a brittle manner. This dichotomy depended fundamentally on the timescales of the different stress relaxation processes. Ichihara et al. (2002) used a viscoelastic material with controlled porosity to investigate the fragmentation behavior by comparing the timescale of decompression with the timescale of glass transition (i.e. relaxation time of the viscoelastic fluid), also known as the Maxwell relaxation time,

$$\tau_r = \frac{\eta_0}{G}, \quad (45)$$

with  $\eta_0$  the zero-shear viscosity and  $G$  the (unrelaxed) rigidity at elastic limit, and the timescale of bubble expansion (i.e. relaxation time of the excess pore pressure by viscous expansion of the liquid),

$$\tau_v = (1 - \phi_0) \frac{4\eta_0}{3P_0}, \quad (46)$$

with  $\phi_0$  and  $P_0$  the initial porosity and pressure, respectively. In these experiments, however, the timescales  $\tau_r$  and  $\tau_v$  were similar and their effect could not be discriminated, and conduit walls could influence the fragmentation process. To overcome these issues, Kameda et al. (2008, 2013) used a new experimental device and a material with a large rigidity  $G$ . They considered the Deborah number,

$$De = \frac{\tau_r}{\tau_d}, \quad (47)$$

with  $\tau_d$  the timescale of decompression (of amount  $\Delta P$ ), which was obtained from the decrease of pressure ( $P$ ) with time ( $t$ ) according to

$$P = P_0 - \Delta P \left( 1 - e^{-\frac{t}{\tau_d}} \right). \quad (48)$$

For a given material, brittle fragmentation and ductile expansion were observed at  $De > 1$  and  $De < 0.02$ , respectively, and intermediate values of  $De$  led to a transitional brittle-like fragmentation through bursting of the material (Kameda et al. 2008). In fact, brittle fragmentation could occur even at low  $De$  indicating ductile response, when the maximum differential stress at the bubble surface

$$\Delta\sigma_{max} = \frac{3\Delta P}{2(1 - \phi_0)} \quad (49)$$

was larger than the critical fracture stress  $\Delta\sigma_c$ . Fragmentation was possible at  $\Delta\sigma_{max} > \Delta\sigma_c$  at  $De \sim 10$ . Brittle fragmentation occurred when  $De > 1$  whereas brittle-like fragmentation was possible at  $De < 1$  but with a time delay (Fig. 12). In more recent works, Kameda et al. (2017) showed that brittle-like fragmentation occurred through development of solid-like fractures in a fluid and was controlled by the local stress field, which depended on the spatial distribution of the bubbles.

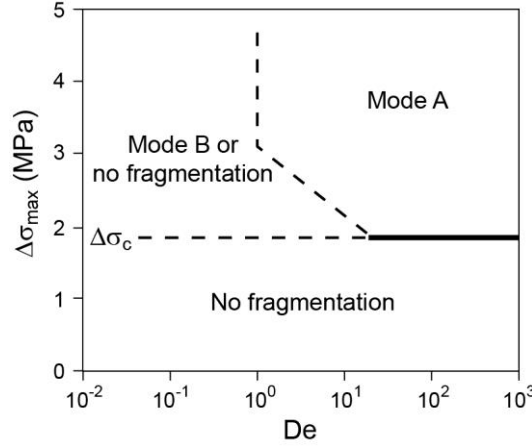


**Figure 12.** Mode of fragmentation as function of the Deborah number (equation 47) and the maximum differential stress  $\Delta\sigma_{\max}$  above the critical stress  $\Delta\sigma_c$ . Fragmentation modes A and B occur when the fragmentation time is respectively smaller or larger than the relaxation time. From Kameda et al. (2013).

### 3.3.3 Conduit flow dynamics

In a conduit, gas-particle mixtures above the fragmentation level and melts containing gas bubbles and/or slugs rising buoyantly are characterized by different physical regimes. Dynamic similarity in experiments is generally ensured for fluid flows but it is often incomplete for biphasic mixtures of gas and solid or fluid particles. For instance, Anilkumar et al. (1993) pointed out that though the particle Reynolds number could be the same in nature as in experiments other dimensionless numbers such as the Froude number were impossible to match owing to the small size of the analogue systems (i.e. gravitational forces were negligible).

Analogue experiments have given insights into the turbulent flow dynamics in volcanic conduits after onset of fragmentation. Biphasic mixtures resulting from disrupted saturated fluids had a discharge rate that first increased, as fragmentation occurred in the flow interior or a fragmentation level moved down the analogue conduit, and that later became nearly constant with some fluctuations due to heterogeneity of the two-phase mixture (Mader et al. 1997, Zhang et al. 1997). Mixtures formed from decompressed beds of solid particles revealed heterogeneous flow structures with dilute and dense parts at early stages before they became fully dilute with particle concentrations typically lower than ~1 vol. % (Anilkumar et al. 1993, Cagnoli et al. 2002). The mixtures ejection velocities were up to ~250-300 m/s at early stages and then decreased with time according to either power or exponential laws (Cigala et al. 2017). In a different configuration, Dufek et al. (2012) further showed that particle collisions in turbulent mixtures could change significantly the grain size distribution. Lane et al. (2001) ensured dynamic similarity of their experiments by matching the conduit radius-to-height ratio ( $<0.01$ ), the pressure ratio  $\Delta P/P$ , the Reynolds number before ( $Re \sim 1$ ) and after ( $Re > 1000$ ) fragmentation, the Mach number after fragmentation ( $\sim 1$ ), and the Capillary number ( $\gg 1$ ) here defined as (compared to equation 10),

$$Ca = \frac{\eta r \frac{d\varepsilon}{dt}}{\sigma} \quad (50)$$

with  $r$  the bubble radius and  $d\varepsilon/dt$  the strain rate. The flows in the analogue conduit generated pressure oscillations related to resonant oscillation modes of the fluid, which were produced by degassing. Such experiments are particularly useful to interpret sismo-acoustic data recorded at volcanoes (see also Rust et al. 2008 for flows through planar conduits).

Flows of fluids of relatively low viscosity with gas bubbles, representative of many basaltic eruptions, are characterized by elongated gas slugs of diameter similar to that of the conduit width and which ascend buoyantly and finally burst at the surface. These slugs may result from the coalescence of smaller bubbles in a foam layer at the roof of the chamber (Jaupart and Vergnolle 1988, 1989, see section 3.1.2) or in the conduit during ascent (Fig. 13). Their physical regimes were addressed by considering dimensionless numbers defined in fundamental studies on gas bubble dynamics and presented in section 2. Seyfried and Freundt (2000) identified the main regimes of slug flows by matching the Reynolds, Froude, Morton and Eotvös numbers, the two latter being defined as

$$Mo = \frac{\eta^4 g}{\rho \sigma^3}, \quad (51)$$

and

$$Eo = \frac{\rho g D^2}{\sigma}, \quad (52)$$

with  $D$  the width of the gas slug. They observed that single slugs, subjected to hydrostatic decompression during ascent, grew and ascended at constant velocity and had negligible internal excess pressure, whereas supplied slugs formed by continuous gas flux rose faster than single slugs. In further experiments, James et al. (2004) considered also the dimensionless inverse viscosity (see also Llewellyn et al. 2012)

$$N_f = \left( \frac{Eo^3}{Mo} \right)^{1/4}, \quad (53)$$

whose values, along with those of the Reynolds number, indicated that the flows were in transitional to inviscid regimes (i.e.  $N_f > 300$ ). Their experiments revealed that the flow of liquid around ascending individual slugs created dynamic pressure variations, which varied with the slug position in the conduit, and that conduit inclination favored the formation of larger and faster but less frequent slugs. They also observed a transition from bubbly to slug flows as the continuous gas flux (and hence volume fraction) increased (Fig. 13). Considering these dimensionless numbers to run large-scale experiments, Pioli et al. (2012) found that the slug speed was controlled by the Froude number. Vergnolle and Ripepe (2008) investigated the deformation of an ascending slug by considering the Weber number (equation 9). At low bubble Reynolds numbers  $Re_b = \rho U_b d_b / \eta \approx 1$ , at which  $We$  was relevant, they observed slug length-to-diameter ratios of  $\sim 2$ -3. Further studies investigated inter-slug interactions (Pering et al. 2017). Del Bello et al. (2015) also studied the influence of a rheological stratification in the conduit, which was representative of most natural cases, and they showed that slugs ascending through an upper viscous plug of degassed fluid exploded more violently as the slugs were pressurized. Capponi et al. (2017) explored shear stresses and gas pressure variations as a function of the rheological contrast).

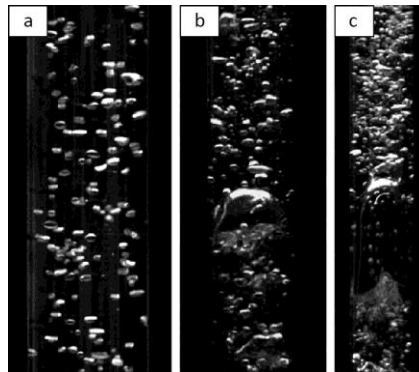


**Figure 13.** Regimes of continuously supplied liquid-gas flow at increasing gas flux and volume fraction in a tube of diameter 4 cm. (a) Bubbly flow, (b) transitional flow, (c) slug flow. James et al. (2004).

### 3.3.4 Degassing

Degassing of vesiculated magmas, caused by bubble escape or the formation of permeable channels through disruption of the magmatic foam or shear-induced strain, is fundamental in controlling the transition from explosive to effusive eruptive regimes. Spina et al. (2016) scaled their experiments relevant to basaltic eruptions by considering the following dimensionless numbers,

$$\frac{d_b}{\delta_f}, \quad \frac{\delta_0}{\delta_f}, \quad (54)$$

with  $\delta_0$  and  $\delta_f$  the initial and final film thickness, respectively. They showed that bubble growth caused thinning of the fluid film between the bubbles, which led to periodic foam disruption at the top of the fluid column and to efficient gas escape. Oscillations of the fluid level related to foam disruption could explain cycles of magma level in conduits as well as in lava lakes (see also Witham et al. 2006). Experimental configurations relevant to more viscous magmas with pervasive shear zones located preferentially along the conduits margins revealed other degassing mechanisms. Lane et al. (2008) observed that fragmentation at the flow margins created fractures that served as pathways for rapid gas

escape. The fractures sealed as the pressure decreased, and then the diffusion of volatiles into the bubbles repressurized the system until subsequent pathways formed, thus causing a cyclic behavior consistent with some natural observations. Such fractures were shown to form in experiments with natural samples even at low vesicularities (Carichi et al. 2011) and degassing stopped when the fractures healed (Yoshimura and Nakamura 2010, Shields et al. 2014). Okumura et al. (2009) further found that shear-induced degassing resulting from bubble coalescence and networking could dominate fracturing except at very shallow part of the conduit. This degassing process was investigated through analogue experiments by Namiki (2012) who showed that it occurred when the strain reached a critical value that decreased with the Capillary number at  $Ca > \sim 1$  (Fig. 14).

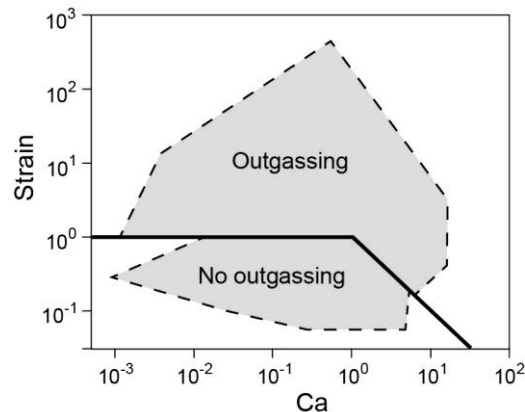


**Figure 14.** Critical strain required for shear-induced degassing as a function of the Capillary number. Shaded areas stand for experimental conditions. From Namiki (2012).

### 3.4 Volcanic jets and plumes

Explosive volcanic eruptions commonly produce high-speed turbulent jets carrying hot gas and particles to several kilometers into the atmosphere. Depending on the intensity and the steadiness of the discharge rate feeding the eruption, the volcanic mixture may either form a Vulcanian- or Plinian-type eruption column. Experimental work have been carried out over decades to understand the role of source parameters and of environmental conditions on the dynamics of these turbulent flows, and they have addressed three main issues (Table S2, Supplementary material): (i) the impact of unsteady conditions at the vent on the flow dynamics, (ii) the dynamics of sustained Plinian columns, and (iii) the mechanisms controlling particle sedimentation from volcanic clouds.

#### 3.4.1 Unsteady volcanic jets

Gas-particle mixtures from explosive volcanic eruptions commonly reach supersonic speeds at the vent and may also generate a shock wave that can travel several kilometers from the volcano. Early experimental studies focused on reproducing these phenomena in the laboratory to investigate the mechanisms controlling the jet expansion into the atmosphere. Kieffer and Sturtevant (1984) erupted various gases (nitrogen, helium, neon) under pressure from a small reservoir into the atmospheric air upon rupture of a thin diaphragm at the exit of a convergent nozzle. The pressure at the nozzle reached 7.25 bar in all experiments, allowing the laboratory jets to reach exit velocities up to 175-868  $\text{m s}^{-1}$ . Such high speeds are of the same order than that of volcanic jets and ensured that the Reynolds number was large enough to reach a high level of turbulence ( $Re = 5 \times 10^4$ ). The experiments revealed that the impulsive acceleration of the gas from the reservoir into the atmosphere produced a starting vortex structure at the head of the jet and a compression wave whose strength mainly depended on the sound speed of the gas and, to a lesser extent, to the gas density (Figure 15a-c). Simultaneously, a rarefaction wave propagated downwards until it reached the bottom of the reservoir and reflected as another rarefaction wave. High-speed shadow and schlieren photography showed that the experiments reproduced several important features of underexpanded jets including Mach disks, Barrel shocks and

N waves. Chojnicki et al. (2006) extended this work by adding particles in a 1-D shock tube experiment in order to understand the behavior of rapidly-decompressed gas-particle mixtures and associated shock waves. Monodisperse mixtures of ballottini glass spheres ( $d_p = 45 - 150 \mu\text{m}$ ,  $\rho_p = 2500 \text{ kg m}^{-3}$ ) and air were rapidly decompressed by rupturing a diaphragm between a high-pressure reservoir (up to 70 bar) and the low-pressure atmosphere. The experiments showed that the presence of particles largely reduced shock velocities (by 30-40%) and strengths (by 60%) compared to the predictions made with the pseudogas approximation (Figure 15d-e). The authors suggested that this difference was due to imperfect coupling between the particles and the gas and they proposed a modified Rankine-Hugoniot relationship to account for this effect:

$$\frac{P_2}{P_1} = 1 + \frac{2\xi}{\xi+1}(M_s^2 - 1) - \frac{F_{da}}{AP_1}, \quad (55)$$

where  $P_1$  and  $P_2$  are the pressure in front of and behind the shock, respectively,  $\xi$  is the ratio of the specific heats for the gas ( $C_p/C_v$ ),  $M_s$  is the shock Mach number (i.e., the ratio of the shock speed to the sound speed of the gas),  $A$  is the cross sectional area of the shock tube, and  $F_{da}$  is the drag force exerted by the particles on the air, such as:

$$F_{da} = \frac{1}{2}C_D\rho_2U_2^2A, \quad (56)$$

where  $C_D$  is a drag coefficient,  $\rho_2$  is the density of the gas behind the shock, and  $U_2$  is the gas velocity behind the shock. Replacing the drag coefficient, which is only a function of the particle Reynolds number, the authors were able to propose new predictions for shock strength ( $P_2/P_1$ ) and velocity ( $U_2$ ) of the gas-particle mixture that were in good agreement with their experimental results (Figure 15d-e). The predictions were then tested against field measurements of volcanic jet and shock velocities during the 1982-1983 Sakurajima and the 2002-2004 Santiaguito eruptions to retrieve the pre-eruption conduit pressures. The values predicted by the new theory (1.5 - 10 MPa) were in better agreement with the typical values for Vulcanian eruptions (5 - 10 MPa) than those inferred from the classical pseudogas theory (0.4 - 1.2 MPa).

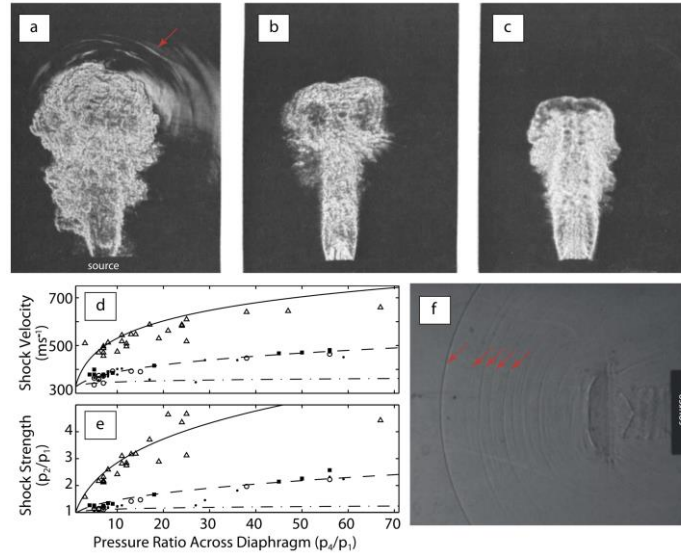


**Figure 15.** Structure of the expanding jets of (a) helium, (b) nitrogen, and (c) freon (modified from Kieffer and Sturtevant, 1984). (d) Shock velocity and (e) shock strength as function of pressure ratio across the diaphragm in the experiments of Chojnicki et al. (2006). Open triangles, solid squares, dots, and open circles correspond to experiments with no particle, 45, 90, and 150  $\mu\text{m}$  particles, respectively. Solid and dashed lines give the predictions of the pseudogas theory and of the new model, respectively. (f) Structure of an expanding jet with multiple shock waves (modified from Medici and Waite, 2016). Red arrows show shock wave panels (a) and (f).

Shock waves travel significant distances from the volcanic vent and are eventually dissipated into sound waves that can be recorded by barometers and infrasound instruments. The experiments of Medici et al. (2014) and Medici and Waite (2016) were designed to investigate how the information carried by the recorded wave can be interpreted in terms of eruption dynamics. A modified shock tube

was used to generate shock waves under controlled conditions. The driver section was filled with nitrogen at different pressures from 50 to 80 bar, and the jet velocity reached 750-810 m s<sup>-1</sup> at the nozzle. The explosive power, shock wave velocity and pressure ratios were accurately measured and compared to predictions from strong shock wave theory. Though this theory significantly overpredicted experimental weak shock wave speed, the scaling typical of shocks can still be used as a first approximation for modeling shock waves generated by volcanic eruptions. The energy that generated the shock wave can thus be calculated by using:

$$E = \frac{(P_m r_m)^3 k_t}{0.155(k_t - 1)^3 P_a^2}, \quad (57)$$

where  $P_m$  is the measured pressure,  $r_m$  is the distance from the vent where the pressure was measured,  $P_a$  is the atmospheric pressure, and  $k_t$  is a pressure ratio that varies between 1.023 and 1.035. Comparing the predictions made with this equation to the total thermal energy estimated from the plume height during the 1982, 1987, 2011 Sakurajima, the 1975 Ngauruhoe, the 2010 Eyjafjallajökull, and the 2006 Augustine eruptions showed that the new model provided a relatively good order of magnitude estimate of eruption energy, suggesting that pressure measurements made at a safe distance from the volcano could be used for improved early warning of eruption hazard. Later, Medici and Waite (2016) extended their work by filling the driver section with nitrogen at lower pressures (from 35 to 50 bar), producing jets with lower velocities at the nozzle (380-530 m s<sup>-1</sup>). The experiments showed that a single discharge could lead to multiple pressure waves (Figure 15f), presumably produced by the interaction with the decelerating jet, and hence suggested that interpretation of shock waves measurements in terms of eruption dynamics is not straightforward.

Laboratory experiments were designed to study the impact of unsteady supply of momentum and buoyancy on the dynamics of volcanic plumes (Clarke et al. 2009, Chojnicki et al. 2014, 2016). Clarke et al. (2009) studied the effect of variations in discharge rate on the plume velocity by injecting upwards a mixture of particles and aqueous solution at the base of a tank containing fresh water. All the source parameters affecting the flow dynamics were varied from one experiment to another: the fluid density (961 to 1037 kg m<sup>-3</sup> by using water with isopropyl or salt), the particle composition (silica powder or ballotini glass spheres), the particle size (<10 μm or 45 μm), the particle concentration (2 or 3.5 vol%), the exit velocity (4-7 m s<sup>-1</sup>), and the pipe diameter (3 or 15 mm). The mass discharge rate was first increased to a peak value and then decreased during each experiment that lasted about 30 s. The Reynolds number of these experiments reached up to 10<sup>5</sup>. The results showed that all the experimental data on flow propagation could be explained by a single scaling law relating the front flow velocity ( $U$ ) to source momentum ( $M$ ) and buoyancy fluxes ( $B$ ), such as:

$$U = c M^{1/2} B^{-1/4} t^{-1}, \quad (58)$$

where  $t$  is the time and  $c$  is a constant factor. Good agreement with natural data on several Vulcanian eruptions suggested that the new scaling law could be used to estimate the total mass and mass discharge rate of natural eruptions as a function of time from the measurement of eruption cloud front velocity. Chojnicki et al. (2014) used a similar experimental device to investigate the effect of mass discharge rate variations on the structure of the jet by visualizing the flow field using a PIV technique. They produced turbulent mixtures of water and particles at the base of a tank containing fresh water. The particles used were silver-coated hollow glass sphere with  $d_p = 10 \mu\text{m}$  and  $\rho_p = 1100 \text{ kg m}^{-3}$ . The scaling analysis was made through the Reynolds number that reached 10<sup>3</sup>-10<sup>4</sup>. The experiments showed that variations in momentum flux at the source quickly modified the jet velocity structure and thus directly controlled the jet dynamics. The comparison of the time-averaged and instantaneous distributions of the vertical component of velocity suggested that some important aspects of the instantaneous dynamics cannot be captured by quasi-steady flow approximation. These experimental results emphasized the need for new modeling approaches capable of describing the time-dependent properties of transient volcanic eruption plumes for improved hazard assessment. To achieve this goal, Chojnicki et al. (2016) carried out new laboratory experiments producing a turbulent jet of fresh water propelled into fresh water at Re between 10<sup>4</sup> and 10<sup>5</sup> and with varying supply of momentum. The results showed that, in contrast to steady or instantaneous momentum sources where the jet rise is captured by a power-law dependence on time, the front height varied logarithmically with time in these experiments. Such evolution was also observed during explosive eruptions at Stromboli, suggesting that the new scaling law could be used to predict the rise of unsteady volcanic plumes from short-duration eruptions.

### 3.4.2 Sustained Plinian columns

Laboratory studies of sustained volcanic columns were initially designed to investigate the different eruptive styles as the eruption conditions change (Figure 16). Carey et al. (1988) presented a series of experiments in which a mixture of water and silicon carbide grinding grit particles ( $d_p = 7 - 120 \mu\text{m}$ ,  $\rho_p = 3210 \text{ kg m}^{-3}$ ) was injected at the base of a tank containing salt water. Varying the particle size, particle content and source velocity led to four different behaviors of the jet. For low particle concentrations, the turbulent mixture formed a buoyant stable plume that reached the top of the tank. After a short period of time, dilute gravity currents began to spread downwards around the plume and flowed short distances across the tank floor. Turbulent mixtures with higher yet low concentrations exhibited several convective instabilities enhancing particle sedimentation and leading to column collapse. At intermediate particle contents, the plume developed a bent-over fountain with a strong asymmetry generating a downward particle-laden flow moving as a gravity current on the tank floor. At high particle contents, a low collapsing fountain formed producing a concentrated gravity current. A last regime corresponded to the whole collapse of a buoyant (at initial stage) plume generating a radially spreading dilute gravity current. In nature, the volcanic mixture of gas and pyroclasts ejected from the vent lightens by turbulent entrainment and heating of cold atmospheric air. A stable plume forms when the bulk density of the mixture attains values lower than that of ambient. This issue was addressed by Woods and Caulfield (1992) through experiments with a mixture of water, methanol and ethylene glycol (MEG) injected downwards ( $\text{Re} \sim 10^2$ ) in a tank containing fresh water, which mimicked the behavior of particle-laden volcanic plumes. The light mixture of water and MEG was injected downwards so that it mixed and became denser than ambient water to form a stable plume. This method had the advantage that the density of the water-MEG mixture was a known function of the degree of mixing between the MEG and the water. Four different behaviors were identified depending on the imposed momentum and mass fluxes at the source: a stable buoyant plume, a collapsing fountain with periodic released of thermals, a collapsing fountain feeding gravity currents from which buoyant material emerged, or a low collapsing fountain. Based on these observations, Woods and Caulfield (1992) proposed a criterion for collapse of the jet as an analytical relationship between the initial density anomaly of the jet ( $\Delta\rho_0$ ) and the minimum volume flux ( $Q_0$ ) required to generate a plume:

$$\Delta\rho_0 \left[ 1 - \left( 1 - \frac{\Delta\rho_0}{\Delta\rho_m} \right)^{1/2} \right] = \frac{16}{5} \alpha_e \frac{\rho_w Q_0^2}{g R_0^5}, \quad (59)$$

where  $\Delta\rho_m$  is the maximum density anomaly a mixture of MEG and water can reach,  $R_0$  is the initial jet radius,  $\rho_w$  is the water density, and  $\alpha_e$  is the entrainment coefficient (see equation 63). The theoretical predictions made with this equation showed a satisfactory agreement with the threshold volume flux measured in the experiments. Further experimental studies showed that the plume shape can evolve with time even if the source conditions are maintained constant (Kitamura and Sumita 2011), and that the plume trajectory can be strongly affected by the presence of wind (Ernst et al. 1994, Carazzo et al. 2014). Four dynamical regimes were identified by Kitamura and Sumita (2011) based on laboratory experiments where jets of water, milk or saline solutions were injected downwards in a tank of fresh water at a constant rate ( $\text{Re} = 10^2 - 10^3$ ). Initially, the laboratory plume had a "finger-like" shape but, as it decelerated and entrained the ambient fluid, a "plume-head" formed, which later transformed in a "cone-like" self-similar shape. In the case where the buoyancy flux was large, the plume head temporarily inflated above the cone to form a "headed cone". Scaling laws for the onset of these four regimes were proposed by the authors and found in good agreement with the laboratory measurements. These large scale structures were similar to those observed during volcanic eruptions, although the Reynolds number was rather low in the experiments, suggesting that monitoring the changes in plume shape during an eruption could be used to constrain their buoyancy.

The impact of wind on the plume dynamics may be critical and experimental studies attempted to quantify this process. Ernst et al. (1994) performed laboratory experiments where cold or hot water was injected at the base of a 25 m-long flume into cold flowing water, generating turbulent jets ( $\text{Re} = 10^3$ ) in a cross-current. The experiments showed that a buoyant jet distorted by a cross-current can develop a vortex pair structure and bifurcate to produce two distinct lobes, which diverge from one another downwind. This bifurcation may initially arise because of the pressure distribution around the plume but it can be further enhanced by the plume buoyancy, the absorption of latent heat due to evaporation of water droplets in the plume, and the tropopause that acts as a density interface. These

results were the first to provide an explanation for the bifurcation observed by satellites and from the ground during historical eruptions, and also inferred from the bilobate distribution of the tephra deposits of past events. Laboratory experiments were also performed by Carazzo et al. (2014) to characterize the effect of wind on the plume trajectory and maximum height. In this study, salt water was injected downwards into a tank containing stratified salt water while the nozzle was towed away at a constant speed, producing turbulent buoyant jets in a cross-flow (Figure 16a-c). The experimental set-up was scaled to reproduce the Reynolds ( $Re = 10^3$ ) and Richardson numbers ( $Ri = 10^{-4} - 10^{-1}$ ), as well as the wind ( $W^*$ ) and plume ( $U^*$ ) velocity ratios of volcanic eruptions, such as:

$$W^* = \frac{W}{U_0}, \quad \text{and} \quad U^* = \frac{NH_0}{U_0}, \quad (60)$$

where  $W$  is the wind speed,  $U_0$  the plume velocity at the source,  $N$  is the Brunt-Väisälä frequency, and  $H_0$  is a characteristic length scale for a pure plume. For low wind speed and relatively high flow rates, the buoyant jet formed a strong plume where the impact of wind was limited (Figure 16a). For high wind speed and relatively low flow rates, the buoyant jet formed a weak plume with a centerline bent over in the wind field (Figure 16c). For intermediate conditions, the jet formed a distorted (or transitional) plume (Figure 16b). The transition from one regime to another was found to depend on the ratio  $W^*/U^*$ , and the experimental results were used to propose new scaling laws to determine the mass discharge rate feeding a volcanic plume from its observed maximum height in the presence of wind, a method that is extensively used for hazard assessment.

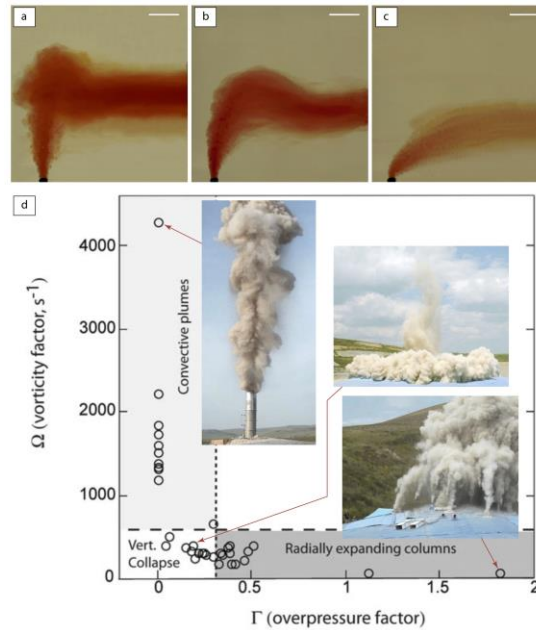


**Figure 16.** Experimental plumes. (a) Strong plume, (b) distorted plume, and (c) weak plume (modified from Carazzo et al. 2014). (d) Regime diagram showing the stability fields of the convective plumes, vertically collapsing fountains, and radially expanding columns (modified from Dellino et al. 2010).

Several experimental works focused on reproducing explosive volcanic plumes by using gas and particles (instead of a pure liquid phase) to cover the range of dynamical parameters controlling natural eruptions (Dellino et al. 2007, 2010, 2014) or to study the mass partitioning in a collapsing fountain (Carazzo et al., 2015). Dellino et al. (2007, 2010, 2014) designed a large-scale apparatus where highly pressurized gas was released at the base of a 30 to 60 cm-large cylindrical conduit filled with samples of natural volcanic particles ( $d_p = 10 \mu\text{m} - 8 \text{mm}$ ,  $\rho_p \sim 2000 \text{kg m}^{-3}$ ). The scaling was made using the Reynolds ( $Re = 10^6 - 10^7$ ) and densimetric Froude numbers ( $Fr = 10^{-1} - 10^1$ ). The resulting highly turbulent particle-laden mixture were propelled at high velocities ( $7 - 110 \text{m s}^{-1}$ ) and formed either a buoyant plume with sedimenting particles or a dense collapsing fountain with gravity currents (Figure 16d) depending on the specific mechanical energy (SEM) of the system. For  $SME > 2.6 \text{kJ kg}^{-1}$ , the flow was in the plume regime, whereas for  $SME < 1.5 \text{kJ kg}^{-1}$  the flow was in the fountain regime (Dellino et al. 2007). In extreme cases, radially expanding columns led to an expanded collapse that

generated dilute gravity currents (Dellino et al. 2010). The authors mapped the three dynamical regimes in their experiments according to a vorticity factor ( $\Omega$  in  $s^{-1}$ ) that characterizes the tendency of the mixture to be sustained by vortices, and an overpressure factor ( $\Gamma$ ) that quantifies the tendency to favor lateral expansion, such as (Figure 16d):

$$\Omega = \frac{2W_{exit}}{RC}, \quad \text{and} \quad \Gamma = \frac{P_{over}}{P_{dyn}}, \quad (61)$$

where  $W_{exit}$  is the exit velocity,  $R$  is the conduit radius,  $C$  is the particle concentration,  $P_{over}$  is the gas overpressure, and  $P_{dyn}$  is the dynamic pressure along the vertical axis. The experiments showed that temperature had almost no effect on the formation of collapsing fountains, on the formation of gravity currents upon collapse, and on the velocity of the shear current at the flow base (Dellino et al. 2010). Carazzo et al. (2015) investigated the mechanisms leading to partial column collapse, a regime observed in nature where the flow separates in a dense collapsing part and a buoyant rising part. For this, they designed an experimental set-up in which a mixture of hot gas and hollow polymer spheres ( $d_p = 13\text{-}120 \mu\text{m}$ ,  $\rho_p = 42 \text{ kg m}^{-3}$ ) was injected upwards in a chamber containing ambient air. The scaling analysis was made using the Reynolds ( $Re = 10^3$ ), Richardson ( $Ri = 10^{-2}\text{-}10^0$ ), Stokes ( $St = 10^{-2}\text{-}10^{-1}$ ), stability ( $\Sigma = 10^{-3}\text{-}10^{-2}$ ) and Peclet numbers ( $Pe = 10^{-4}\text{-}10^{-2}$ ) that were imposed to partially match those of natural eruptions. The experiments showed that for low concentrations and high flow rates, the turbulent mixture formed a buoyant plume, whereas for high concentrations and low flow rates, a collapsing fountain occurred. The collapse was rarely total and the mass partitioning between the rising part and the collapsing part, that was determined by collecting the particles fallen on the chamber floor, depended on a buoyancy ratio  $R_s$  such as:

$$R_s = \frac{\alpha\Delta T}{\gamma\Delta C}, \quad (62)$$

where  $\alpha$  and  $\gamma$  are the volumetric expansion coefficient for heat and particles, respectively, and  $\Delta T$  and  $\Delta C$  are the temperature and particle concentration differences between the ambient and the plume at the altitude where the flow separates, respectively. At this separation height, particles tended to fall because the flow velocity decreased to values lower than their settling velocity, whereas the thermal gradient between the flow and the ambient tended to promote the rise of the plume. The ratio  $R_s$  fully captured this behavior in the experiments and it was also found to correctly explain the mass partitioning observed in the deposits of past eruptive events in the partial collapse regime.

Among the mechanisms controlling the dynamics of explosive volcanic plumes, the phenomenon of turbulent entrainment of air into the flow has received a large attention over the last decade. Typically, the entrainment rate of ambient fluid at the plume margins ( $U_e$ ) is assumed to be proportional to the average vertical velocity of the plume ( $U$ ) through an entrainment coefficient ( $\alpha_e$ ), such as (Morton et al. 1956):

$$U_e = \alpha_e U, \quad (63)$$

where the entrainment coefficient is commonly taken as a constant between 0.07 for neutrally buoyant jets and 0.16 for buoyant plumes (Linden 2000). Kaminski et al. (2005) proposed new laboratory experiments using the same experimental technique as Woods and Caulfield (1992) and showed that turbulent entrainment can be significantly reduced in jets with negative buoyancy ( $\alpha_e = 0.05$ ). This reduction of entrainment was well described by a linear dependence of the entrainment coefficient on the local Richardson number, and to a lesser extent to a similarity drift corresponding to a weak evolution of the shapes of the velocity and buoyancy profiles with the distance from the source. These results suggested that the conditions of collapse can be significantly affected by the drastic reduction of entrainment close to the vent where the mixture of hot gas and particles is denser than the ambient medium. Later, Paillat and Kaminski (2014a,b) extended this work to investigate turbulent entrainment in plane pure plumes and plane pure jets. In these studies, water and salt water were injected downwards in a tank of water or water and ethanol, generating turbulent linear jets or plumes ( $Re = 10^1\text{-}10^2$ ). Particle image velocimetry was used to measure the velocity, buoyancy and turbulent shear stress profiles, and to determine the value of  $\alpha_e$ . For the planar pure jets, the authors found no systematic variations of  $\alpha_e$  as a function of  $Re$  or the distance from the source. For the planar pure plumes, however, the variations in  $\alpha_e$  were well explained by the contribution of buoyancy. The effects of nozzle geometry and particle content on  $\alpha_e$  were also investigated experimentally (Jessop and Jellinek 2014, Jessop et al. 2016). In these studies, a mixture of water and silica powder ( $d_p = 40\text{-}325 \mu\text{m}$ ,  $\rho_p = 2500 \text{ kg m}^{-3}$ ) was injected at the base of a tank containing fresh or salt water through a straight or flared nozzle. The scaling analysis

was made using the Reynolds ( $Re = 10^3$ ), Richardson ( $Ri = 10^{-7}$ - $10^{-1}$ ), Stokes ( $St = 10^{-1}$ - $10^0$ ), and stability numbers ( $\Sigma = 10^{-2}$ - $10^{-1}$ ). The experiments revealed that particle inertia and vent geometry both had a crucial effect on the shape of the largest eddies at the edges of the jet, affecting turbulent entrainment of ambient fluid. Particles were found to augment the angular momentum of entraining eddies, forcing them to overshoot more deeply into, deform and engulf the ambient fluid. Entrainment in the flow was also enhanced for flared nozzles but it was reduced for cylindrical nozzles (Jessop and Jellinek 2014). Experiments made with linear and annular vents revealed that entrainment was reduced as the vent width became small compared to its length because the size of the entraining eddies scaled with the vent width (Jessop et al. 2016). These experimental results suggested that a reduction of entrainment, potentially leading to column collapse, may occur during an eruption due to vent erosion. The efficiency of turbulent entrainment was also investigated by Solovitz and Mastin (2009) and Solovitz et al. (2011) who propelled compressed air into ambient air ( $Re = 10^5$ ) and made particle image velocimetry (PIV) measurements to examine the development of the flow structure near the source. The entrainment coefficient estimated from the instantaneous and time-averaged velocity fields at several axial distance from the vent was always much lower than commonly measured in laboratory studies for both subsonic ( $\alpha_e = 0.02$ - $0.045$ ) and sonic jets ( $\alpha_e = 0.015$ - $0.04$ ). The authors suggested that in this developing region near the vent, the influence of the high-momentum jet flow had not yet diffused outward to equilibrate with ambient conditions, reducing the efficiency of turbulent entrainment.

### 3.4.3 Particle sedimentation

Several laboratory experiments were done to understand transport and deposition of volcanic materials from plumes. Sparks et al. (1991) proposed a theoretical model for the sedimentation of particles from dilute suspensions generated by turbulent plumes and they tested it against laboratory experiments made using the same experimental device as Carey et al. (1998). The theory assumed that particles were distributed homogeneously in the suspension by turbulence. At the base of the suspension where turbulence diminishes, the particles were assumed to fall out at their terminal fall velocity ( $U_t$ ), resulting in an exponential decrease in the concentration of particles ( $C$ ) with the distance from the source ( $r$ ), such as:

$$C(r) = C_0 \exp\left[-\frac{\pi U_t}{Q}(r^2 - r_0^2)\right], \quad (64)$$

where  $Q$  is the volumetric flow rate of the suspension,  $C_0$  is the initial particle concentration at the distance  $r_0$ . The results showed an excellent agreement between the model and the experiments (Figure 17a), and also between the model and field data from the Fogo A Plinian eruption, suggesting that the physics of particle sedimentation was fully captured by the model. The authors noted nevertheless that in the proximal region, where the buoyant plume spreads out to form a horizontal suspension, particle sedimentation was affected by the fall-out of the coarser particles from the plume margins. Ernst et al. (1996) explored this phenomenon by using the same set-up but with larger particles ( $d_p = 115 - 327 \mu\text{m}$ ,  $\rho_p = 3210 \text{ kg m}^{-3}$ ). The fall-out of the largest particles from the plume margins was well captured by a modified theoretical model of turbulent jets and plumes (Morton et al. 1956) that used the same assumptions as in Sparks et al. (1991). However, the smallest particles fallen from the plume margins were re-entrained at lower levels after fallout, making sedimentation less efficient. The authors introduced a re-entrainment parameter in their model to explain their experimental results (Figure 17b). This parameter was found to be constant for jets ( $\phi = 0.1$ ) and plumes ( $\phi = 0.4$ ). Veitch and Woods (2000) studied the effect of this re-entrainment on the dynamics of the buoyant plume. Their experiments consisted in a mixture of fresh water and glass beads ( $d_p = 40 - 70 \mu\text{m}$ ,  $\rho_p = 2500 \text{ kg m}^{-3}$ ) at the base of a tank containing salt water, producing a turbulent jet that rose to the top of the tank before spreading out radially as a gravity current. Varying the initial particle concentration led to different dynamical regimes for the plume. At low particle concentrations, the particles settled through the ambient fluid individually at their settling velocity. At intermediate particle concentrations, a coherent annular structure developed downwards around the rising plume. The re-entrainment of particles increased the density of the ascending plume, making the radially spreading gravity current a dense intrusion. Above a critical particle concentration, a downward convecting flow immediately developed from the gravity current and the plume underwent an oscillatory collapse. The transition from one regime to another was

successfully captured by a modified model of turbulent plumes (Morton et al. 1956) that included particle re-entrainment.

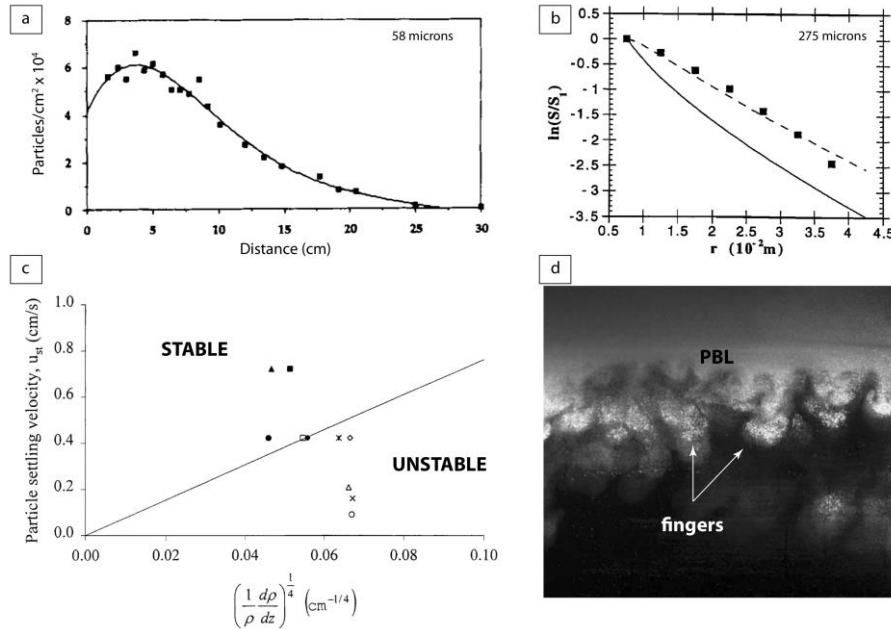


**Figure 17.** Experimental studies on particle sedimentation from plumes. (a) Sediment mass (in  $\text{cm}^{-2}$ ) as a function of the distance from the vent, with  $d_p = 58 \mu\text{m}$  (Sparks et al. 1991). The solid curve is a best fit function. (b) Sediment accumulation as a function of the distance from the vent, with  $d_p = 275 \mu\text{m}$  (Ernst et al. 1996). Dashed and solid curves correspond to theoretical predictions made with and without re-entrainment. (c) Regime diagram indicating the conditions under which gravitational instabilities (unstable) or individual particle settling (stable) develop (modified from Cardoso and Zarrebini 2011a). (d) Photograph of the base of a particle-laden suspension showing the particle boundary layer (PBL) and the fingers associated with settling-driven gravitational instabilities (modified from Scollo et al. 2017).

Cardoso and Zarrebini (2001a,b) studied the deposition patterns from gravity currents generated by turbulent plumes at the buoyancy level and carrying polydisperse glass beads particles ( $d_p = 33 - 115 \mu\text{m}$ ,  $\rho_p = 2470 \text{ kg m}^{-3}$ ). Predictions of the deposition patterns made with a modified equation (64) taking into account the polydispersity of particles were successfully compared to the experiments. A striking observation was the development of convective instabilities at the base of the gravity currents, characterized by thin fingers of fluid with large concentration of particles that moved downward at velocities much larger than the settling velocity of the particles (Figure 17d, Cardoso and Zarrebini, 2011a). The authors derived a simple criterion for the onset of these settling-driven gravitational instabilities based on the Stokes' settling velocity and the density gradient in the environment. Further works on this type of instability were done by Carazzo and Jellinek (2012), Manzella et al. (2015), and Scollo et al. (2017) who ensured the suitability of the experiments to reproduce natural eruption plumes by matching the Reynolds, Richardson, Grashof, Stokes, and stability numbers. Similar observations were made by Carazzo and Jellinek (2012) in their experiments producing turbulent particle-laden jets and subsequent intrusive gravity currents into a stratified environment. A scaling analysis was derived to show that during the spreading of the gravity current, internal sedimentation drove the growth and intermittent overturn of a thin, unstable particle boundary layer (PBL) that formed particle-rich fingers. For natural eruptions, this settling-driven gravitational instability was expected to occur depending on the grain-size distribution of the particles, particle concentration, and to a lesser extent plume height. Manzella et al. (2015) and Scollo et al. (2017) refined this work by performing laboratory experiments in which an aqueous suspension of glass beads or volcanic material ( $d_p = 32 - 180 \mu\text{m}$ ,  $\rho_p = 2550 \text{ kg m}^{-3}$ ) was emplaced above a layer of sugar solution. Instabilities formed at the boundary of the two layers propagated downward. Measurements of the evolution of particle concentration, number of fingers and

finger speed in the lower layer confirmed that particle sedimentation could be significantly enhanced by settling-driven instabilities in volcanic clouds.

The intensity of turbulence has a strong effect on the distribution of volcanic ash particles within the cloud (Koyaguchi et al. 2009), which in turn controls their effective settling velocity (Del Bello et al. 2017). Laboratory experiments made by Koyaguchi et al. (2009), in which glass beads ( $d_p = 23 - 100 \mu\text{m}$ ,  $\rho_p = 2500 - 4200 \text{ kg m}^{-3}$ ) were mixed in stirred water with various intensities of turbulence, revealed that the particles remained homogeneously distributed in the fluid and settled at their terminal fall velocity when the root-mean-square of velocity fluctuation in the fluid was much larger than the particle terminal velocity. On the other hand, when the root-mean-square of velocity fluctuation was smaller than the terminal fall velocity, particles concentrated at the base of the fluid as a PBL that ultimately formed particle-rich fingers. These experimental results were compared to predictions of volcanic plume dispersion using a 3D numerical model and suggested that particles greater than a few millimeters are not homogeneously distributed in volcanic clouds but tend to concentrate at the base. The effect of particle concentration on the settling velocity of individual particles was investigated experimentally by Del Bello et al. (2017) who released volcanic particles in a box ( $d_p = 125 - 1000 \mu\text{m}$ ,  $\rho_p = 764 - 2846 \text{ kg m}^{-3}$ ) and measured the particle settling velocities and concentrations. The results revealed that the settling velocity was largely enhanced by particle-fluid interactions but partially attenuated by particle-particle interactions with increasing concentration. The authors proposed a new empirical relationship to calculate the settling velocity of an individual particle from its size, density, shape and particle concentration, which can be easily implemented in numerical models of volcanic ash dispersal.

Other intriguing phenomena observed in volcanic clouds were reproduced in the laboratory. Holasek et al. (1996) simulated the separation of ash and gas and the formation of secondary intrusions from a volcanic cloud, a phenomenon that occurred during the 1990 Reboudt and 1980 Mt St Helens eruptions. The experiments consisted in injecting horizontally a mixture of fresh water and particles ( $d_p = 17 - 37 \mu\text{m}$ ,  $\rho_p = 3210 \text{ kg m}^{-3}$ ) in a tank containing a stratified saline solution. As the intrusion became progressively thinner during propagation, a layer of particle-depleted fluid gradually developed on the upper surface of the intrusion and became thicker as sedimentation continued. Small fingers ascended from the particle-poor upper part of the intrusion while particles sedimenting from the lower particle-rich part of the intrusion were swept back towards the source due to a relatively strong return flow in the tank. This particle-laden fluid was relatively dense and descended below the main intrusion to a new level a neutral buoyancy where it formed a secondary intrusion. A remarkable layering of the intrusion was also observed in the experiments of Carazzo and Jellinek (2013) who used the same set-up and scaling analysis as Carazzo and Jellinek (2012). The production of internal layering in these experiments was due to a large scale instability driven by particle sedimentation and to the differential diffusion of salt and fine particles. This particle diffusive convection was expected to occur in natural volcanic clouds where heat diffuses faster than fine particles, hence enhancing particle sedimentation. A new model of particle sedimentation was built and found in good agreement with real-time measurements of the rate of change of particle concentration in a few explosive eruptions. Interestingly, this type of instabilities led to regions with locally large particle concentrations, providing a potential way to produce aggregation processes. Evidence of interactions between convective instabilities and particle aggregation was also provided by the experiments of Manzella et al. (2015) and Scollo et al. (2017).

#### 3.4.4 Particle aggregation

Experimental studies have provided fundamental insights on the processes of volcanic ash aggregation, by which individual particles collide and bind to form aggregates that may potentially breakup (Table S3, Supplementary material). Gilbert and Lane (1994) performed experiments in a recirculating wind tunnel with various particle types (andesitic volcanic ash, glass beads, silicon carbide, fused alumina) to investigate the mechanisms controlling the growth of accretionary lapilli in volcanic ash clouds. Two series of experiments were made to study the formation of aggregates under wet conditions. In the first series, single liquid droplets were injected in the tunnel and particles were introduced in the flow stream. The scavenging of ash by liquids drops formed layered aggregates with a hemispherical geometry and a flat surface that were not similar to the massive or concentrically-structured aggregates observed in the field. In the second series, a polystyrene sphere coated with a liquid layer was used as pre-existing nucleus in suspension. Particles fed into the flow stream collided

with the liquid layer and stuck to the sphere, generating concentrically-zoned, cemented and spherical aggregates that matched the field observations. Gilbert and Lane (1994) developed a simple description of accretionary lapilli growth based on collision and coalescence models for raindrop growth, and proposed an experimentally-derived aggregation coefficient aimed at estimating the aggregate size distributions in volcanic ash clouds. Schumacher (1994) and Schumacher and Schmincke (1995) investigated the characteristic of ash aggregates produced by an electrostatic powder-coating device and by an oscillatory pan device under liquid water conditions. The results showed that in dry conditions the volcanic ash formed instantaneously layered and fine-grained aggregates bound by electrostatic forces. Under wet conditions, capillary forces of liquid bridges from condensed moisture drove the formation of spherical well-developed aggregates, whose strength increased with the liquid water content. The authors concluded that both capillary and electrostatic forces may be effective during the formation of accretionary lapilli in volcanic ash clouds.

The role of electrostatic forces as a binding agent was investigated using several experimental techniques. James et al. (2002, 2003) presented experiments in which fine particles were produced by fracturing a 2 cm-large pumice and aggregated, as they fell in 1 m-long a chamber, due to electrostatic charges imparted during the fracture process and to the differential fall velocities. Detailed photographs and Elzone analyses of the resulting aggregates allowed to determine crucial physical properties and fall characteristics. The particle size distributions of the aggregates systematically followed an exponential type law, with a maximum size of 800  $\mu\text{m}$ , and the aggregate densities were much lower (80 - 220  $\text{kg m}^{-3}$ ) than that of individual ash particles (2200  $\text{kg m}^{-3}$ ). Bimodal particle size distributions were also produced, a feature that is commonly observed in tephra fall deposits. The authors proposed several empirical relationships to determine the size distribution and drag coefficient of volcanic ash aggregates that can be easily implemented in ash dispersal models. Telling and Dufek (2012, 2013) further investigated the role of electrostatic forces in a humidity-controlled tank where silica or volcanic ash particles were propelled and formed aggregates. They correlated the number of particle collisions that resulted in the formation of an aggregate to different ambient water vapor contents and they found that aggregation efficiency was highly dependent on collision kinetic energy (Figure 18a). The relative humidity was varied from 11 to 95% and was important only for particles that had long residence times in a high-humidity environment. The authors concluded that electrostatic forces were the main driving mechanism for particle aggregation in their experiments. To quantify the importance of hydrodynamic and electrostatic forces, the authors introduced a Stokes number that compared the relative inertial timescale of a particle to the viscous fluid timescale of the film of water that formed around a particle under wet conditions:

$$St = \frac{mU}{6\pi\eta r^2}, \quad (65)$$

where  $m$ ,  $U$  and  $r$  are the particle mass, velocity and radius, respectively, and  $\eta$  is the viscosity of the interstitial fluid. The critical Stokes number below which aggregation occurred was found to be of the order of  $10^1$  in the experiments, a condition that was never reached under dry conditions ( $St \sim 10^2 - 10^3$ ). To explain the formation of aggregates in the latter case, the authors introduced a ratio that compared the inertial and electrostatic forces:

$$IE = \frac{\delta m U^2}{K q^2}, \quad (66)$$

where  $\delta$  is the distance between two charges,  $K$  is the Coulomb's constant, and  $q$  is the particle charge. The critical IE ratio below which aggregation occurred was of the order of  $10^0$  in the experiments made under dry conditions. Probabilistic relationships were then developed to predict the efficiency of aggregation in volcanic ash dispersal models under both wet and dry conditions. Del Bello et al. (2015) performed similar laboratory experiments under turbulent ( $Re = 10^3$ ) and low-humidity (50-60%) conditions, and they confirmed the importance of collision kinetic energy (CKE) on aggregation efficiency. The results showed that disaggregation dominated over aggregation as the CKE was increased (Figure 18b). The minimum charge density required for particle aggregation to occur was found to be  $0.3-1.7 \times 10^{-2} \text{ C m}^{-2}$ , a value higher than those inferred in previous experimental studies, i.e.,  $2-5 \times 10^{-4} \text{ C m}^{-2}$  (Telling and Dufek 2012, 2013) and  $0.5-1 \times 10^{-3} \text{ C m}^{-2}$  (James et al. 2002, 2003). These differences were attributed to the enhanced turbulent conditions that increased the collision velocities of the particles and contributed to higher charges. Furthermore, aggregation was possible for particles smaller than 63  $\mu\text{m}$ , a threshold value much smaller than those of previous experiments in dry

conditions, i.e.,  $\sim 125\text{-}180\ \mu\text{m}$  (Schumacher 1994),  $\sim 150\ \mu\text{m}$  (James et al. 2003), and  $170\ \mu\text{m}$  (Van Eaton et al. 2012).

Van Eaton et al. (2012) investigated the role of liquid water and ice on the formation of ash and ash-ice aggregates using a vibratory pan aggregation technique. The experiments successfully reproduced aggregates with characteristics (grain-size distribution, maximum particle size and mean density) comparable to those of natural eruptions (Figure 18c-f). The density and maximum aggregate size were found to increase with the amount of liquid added in the experiments until oversaturation was reached ( $> 20\text{-}25\%$ ) and liquid mud droplets were formed. Mueller et al. (2016) confirmed that liquid bonding can be the primary control on the formation of aggregates by using a fluidization bed technique. The aggregates formed were generally fragile but could be more stable when the particles were initially coated with high concentrations of NaCl whose dissolution and reprecipitation made solid interparticle bridges. The initial granulometry strongly influenced the growth and structure of aggregates, while the rate of aggregate formation increased exponentially with increasing relative humidity in the range  $12\text{-}45\%$  (Figure 18g), above which overwetting promoted mud formation.

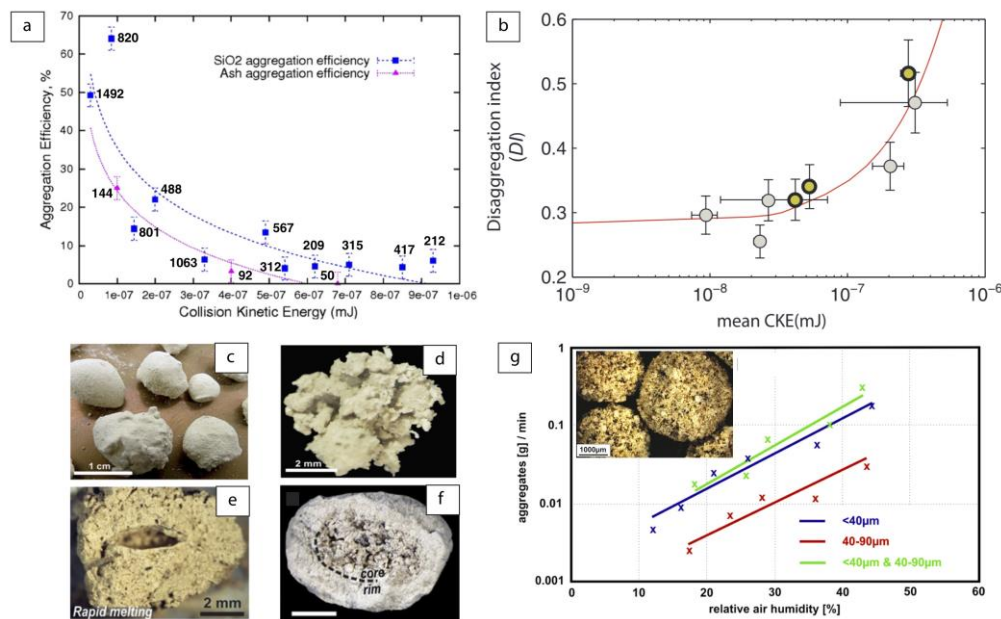


**Figure 18.** Experiments on particle aggregation. (a) Aggregation efficiency as a function of the collision kinetic energy (modified from Telling and Dufek 2012). (b) Disaggregation index as a function of the collision kinetic energy (modified from Del Bello et al. 2015). (c)-(f) Photographs of experimental aggregates (modified from Van Eaton et al. 2012): (c) ash-ice aggregate formed in the absence of a liquid phase, (d) ash-ice cluster formed by freezing liquid drops, (e) ash aggregate formed by rapid water melting and boiling, (f) ash aggregation formed by wet aggregation at room temperature. (g) Rate of aggregate production as a function of the relative humidity, and photograph of an experimental aggregate (modified from Mueller et al. 2016).

### 3.5 Pyroclastic density currents

Pyroclastic density currents (PDC) are hot mixtures of gas and particles that propagate predominantly horizontally under the influence of gravity (Sulpizio et al. 2014, Dufek 2016). The physics of these currents is certainly one of the most debated issues in volcanology, and in this regard the experimental approach may be particularly insightful. Though experiments on PDC have been done since the 1960's (McTaggart 1960) detailed studies were carried out only fairly recently. Experimental investigations have addressed the two types of solid particle transport in gravity currents, i.e. (i) dilute mixtures in which particles are carried by the turbulent fluid phase, and (ii) dense granular flows in which momentum is transferred through particle interactions and/or solid-fluid interactions. These two

mechanisms are thought to operate simultaneously in distinct parts of most currents (Breard et al. 2016). Owing to scaling considerations, but also technical requirements or limitations in some cases, the experiments have involved either a liquid or a gas (most often water or air) as the analogue fluid phase.

### 3.5.1 Dilute turbulent flow regime

The experimental studies on dilute PDC first relied on the methods used to investigate, in a general context, Boussinesq turbulent gravity currents whose density ( $\rho_c$ ) is slightly larger than that of their surrounding medium ( $\rho_a$ ) (cf. Benjamin 1968). Subaqueous turbidity currents are other natural examples of this type. Experiments on these currents commonly involve a given liquid as the current and ambient fluid phases, so that the Boussinesq condition is satisfied even though the current contains dissolved salt or solid particles, and they are commonly done in the so-called lock-exchange (or dam-break) configuration. The emplacement of such fluid-particle mixtures is controlled fundamentally by the balance between inertial and buoyancy forces as well as the flow resistance, which set the current Froude number

$$Fr = \frac{U}{\sqrt{g'h}}, \quad (67)$$

where  $U$  and  $h$  are the current front velocity and thickness, and  $g'$  is the reduced gravity equal to  $g(\rho_c - \rho_a)/\rho_a$  according to Benjamin (1968) analysis. We highlight two issues regarding the definition of  $g'$  when considering scaling of experiments applied to dilute PDC. First, the term  $(\rho_c - \rho_a)/\rho_a$  is several orders of magnitude smaller in experiments than in nature. Second,  $g'$  may be defined only if  $\rho_c < 2\rho_a$  (otherwise  $g'$  would be larger than  $g$ ) whereas dilute PDC may be more than twice denser than the ambient atmosphere. These two caveats indicate that  $g'$  may be rather defined as  $g(\rho_c - \rho_a)/\rho_c$ , which satisfies the condition  $g' < g$  in all cases and is applicable to any ambient fluid. Sedimentation of the particles from the turbulent current is controlled by the balance between the shear current velocity ( $u_*$ ) and the particle settling velocity ( $u_s$ ), which is expressed by the Rouse number:

$$Pn = \frac{u_s}{C_K u_*}, \quad (68)$$

where  $C_K \sim 0.4$  is the von Kármán constant, so that particles with  $Pn < 2.5$  are supported by fluid turbulence whereas those with  $Pn > 2.5$  are not. Particle settling causes the solid concentration to decrease exponentially with time and in consequence leads to a progressive decrease of the current density, speed and Reynolds number (Dade and Huppert 1995, Stix 2001). Choux and Druitt (2002) investigated the segregation of particles of different densities and with polydisperse log-normal size distributions typical of PDC. They considered dense and light particles as analogue lithics and pumices, respectively, whose size ranges were chosen to satisfy hydrodynamic equivalence (i.e. same settling velocity) and which had Rouse numbers indicating regimes of turbulent support or settling. They scaled their experiments considering  $Re$ ,  $Fr$ , and  $Pn$  as well as the effective particle density  $(\rho_D - \rho_a)/(\rho_L - \rho_a)$ , with  $\rho_D$  and  $\rho_L$  the density of the dense and the light components, respectively. They showed that at initial particle concentrations of 0.6-23 vol. % the dense particles were segregated according to  $Pn$  and that the light particles obeyed hydrodynamic equivalence only at concentrations lower than a few percent whereas they segregated efficiently at higher concentrations. Further experiments revealed vertical and longitudinal reverse grading of the large light particles in the deposits due to delayed sedimentation (Choux and Druitt 2004).

Entrainment of the ambient air by dilute PDC is another important mechanism. It occurs through destabilization of the interface between a current and its surrounding medium, which is described by the Richardson number (Equation 3). Air entrainment increases as  $Ri$  decreases due to a smaller density difference and/or a higher shear velocity between the current and the ambient air. The entrained cold air is heated and expands, thus causing the bulk density of the gas-particle mixture to decrease, and the current may eventually lift off if it becomes buoyant. The lift-off mechanism was investigated in experiments involving various liquids (mixtures of ethanol, ethylene glycol and water, or fresh water with particles into saline water) whose properties could vary while they mixed with another fluid. For flows on a horizontal substrate, Hallworth et al. (1993) showed that entrainment into the head of a turbulent gravity current did not depend on the density difference with the ambient medium but was controlled by the initial volume of the current and increased with the distance of propagation. In a similar configuration, experiments of Sher and Woods (2017) revealed that lift-off occurred at travel distance

~9-12 times the initial current length. For currents down slopes, experiments showed that temporal confinement of the current by a buoyant plume caused by ambient fluid entrainment along the flow axis could in turn reduce mixing and promoted pulses of unmixed fluid (Huppert et al. 1986) and that sudden changes in slope angle caused hydraulic jumps that enhanced entrainment (Woods and Bursik 1994). Experiments on currents containing particles showed that sedimentation contributed also to decrease the current density, which caused strong flow deceleration before lift-off occurred (Sparks et al. 1993, Woods and Bursik 1994).

Several subsequent studies on dilute PDC involved air as the ambient fluid and permitted experimentalists to further explore the flow dynamics. In this configuration, large-scale devices (>~5-10 m) were used to create currents large and fast enough to be in a fully turbulent regime with  $Re > 10^3$  (Dellino et al. 2007, Lube et al. 2015). Dellino et al. (2010a, 2010b) measured the dynamic pressure of currents generated from collapse of a column of pyroclastic material initially ejected upwards in air from a vertical conduit, and they reported that the current velocity increased with the impact mass flow rate. Thermal effects, which are fundamental in natural dilute PDC, were investigated by Andrews and Manga (2011, 2012) in currents at concentrations <0.003 vol.% and generated by releasing from a steep incline 20  $\mu$ m talc powders heated at 30-100°C. These authors scaled their experiments considering  $Re$ ,  $Fr$  and  $Ri$ , and they pointed out that though  $Re$  in experiments could not match that in nature it was nevertheless higher than  $\sim 10^3$  and thus ensured conditions for fully turbulent flows. The behavior of the particles was described by two dimensionless numbers. The first was a Stokes number defined as:

$$St = \frac{\tau u'}{f \Lambda} \left( 1 + \frac{\rho_c}{2\rho_p} \right), \quad (69)$$

with  $\tau$  the particle characteristic response time,  $u'$  the fluctuations in fluid velocity,  $f$  a drag coefficient,  $\Lambda$  the characteristic turbulent length scale, and  $\rho_c$  and  $\rho_p$  the bulk current and particle densities, respectively (see equation 4 for comparison). The second was the stability number defined as

$$\Sigma = \frac{u_s}{u'}, \quad (70)$$

which indicated whether the particles were suspended ( $\Sigma < 1$ ) or settled ( $\Sigma > 1$ ) (see equation 5). Thermal effects were accounted for by (i) the thermal Richardson number, which is the ratio of buoyant to forced convection,

$$Ri_T = \frac{g \Delta T \alpha h}{U^2}, \quad (71)$$

with  $\Delta T$  the difference in temperature between the current and the ambient air,  $\alpha$  the coefficient of thermal expansion,  $h$  the current thickness, and  $U$  the current mean velocity, and (ii) the ratio of buoyant thermal energy over the kinetic energy defined as

$$\frac{TE_b}{KE} = \frac{\rho_c (C_{p,c}/C_{p,a}) \alpha \Delta T g h}{\rho_c U^2 / 2}, \quad (72)$$

with  $C_{p,c}$  and  $C_{p,a}$  the heat capacities of the current and air, respectively. The experiments revealed that both the particle concentration and the current velocity increased downwards, and that lift-off set approximately the current runout distance (Fig. 19a-b). In contrast with experiments with liquids, ambient air entrainment occurred essentially behind the head and not at the flow front, and sedimentation was not steady as it proceeded through successive sedimentation-erosion events, so that the deposit thickness did not decrease exponentially from the source. The runout distance decreased and the particle fractionation into the buoyant lift-off increased as  $TE_b/KE$  increased, showing that current expansion and buoyancy reversal was favored by excess thermal energy (Andrews and Manga 2012). Air entrainment occurred preferentially along the current lateral margins through vertically oriented vortices, which prevented lateral spreading and favored unidirectional propagation (Andrews 2014).

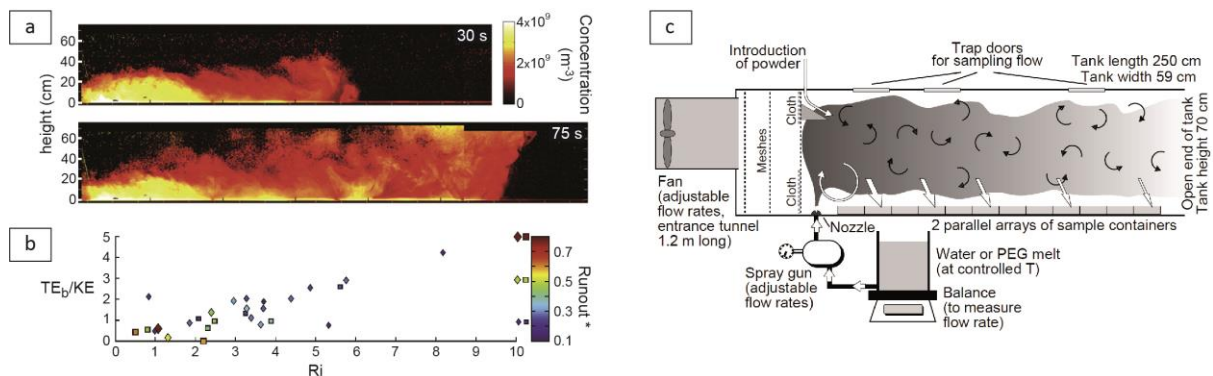


**Figure 19.** Experiments on dilute PDC. (a) Current of heated 20  $\mu\text{m}$  talc powder with large Kelvin-Helmholtz instabilities on top and lift-off at the maximum runout distance (at 75 s). Yellow color corresponds to higher particle concentration. (b) Normalized flow runout as a function of  $TE_b/KE$  and  $Ri$ . (a) and (b) from Andrews and Manga (2012). (c) Experimental device of Freundt (1998) used to generate turbulent suspensions of droplets.

Gas-particle dilute currents were also generated in a wind tunnel in which a turbulent air flow was blown. Freundt (1998) addressed the emplacement of PDC of high-temperature, which form the so-called high-grade ignimbrites that resemble lavas. A spray generated from polyethylenglycol (PEG) melt was injected upwards into a horizontal turbulent air flow and was then advected laterally (Fig. 19c). The experiments were scaled considering the turbulent flow conditions (through  $Re$  and  $Re_p$ ) as well as the aggregation of the droplets, which was accounted for by two dimensionless numbers that described the stability of bonding necks in the aggregates: the Weber number, whose length scale was the size of the droplets  $d_p$  (see equation 9), and the Ohnesorge number

$$Oh = \frac{\eta_p}{\sqrt{\rho_p d_p \sigma}}, \quad (73)$$

which was the ratio of viscous forces to surface tension, with  $\eta_p$  and  $\rho_p$  the viscosity and the density of the droplets, respectively. The sedimentation rate was higher than for non-coalescing particles and it decreased downstream owing to less frequent collisions as the droplets concentration decreased. Notice that other experiments at high particle concentrations revealed the formation of catastrophic agglomerates that defluidized rapidly, which suggested that the emplacement of high-grade ignimbrites by dense currents was not possible. Other studies characterized welding (or sintering) and viscous deformation of hot static materials as a function of the material temperature and pressure, the size of the melt aggregates and the strain typical of volcanic contexts (Grunder et al. 2005, Quane and Russell 2005, Vasseur et al. 2013).

Laboratory experiments have also addressed the complex dynamics of horizontal blasts such as that of the 1980 Mount St-Helens eruption. Orescanin et al. (2010) investigated unsteady supersonic free jets in a shock tube facility by releasing suddenly a compressed gas into the ambient air, a configuration also relevant to vertical blasts (see Fig. 15). Their study revealed that the propagation of a free jet led to the formation of a main shock system that expanded downstream and consisted of symmetrical lateral barrel shocks and of a frontal Mach disk shock. The latter reached a maximum distance controlled by the vent diameter ( $D$ ) and the ratio of the initial gas pressure ( $P_r$ ) over the atmospheric pressure ( $P_a$ ), so that

$$\frac{x_m}{D} = 0.67 \left( \frac{P_r}{P_a} \right)^{1/2}. \quad (74)$$

Orescanin et al. (2014) further investigated jets released over a horizontal rigid surface (Fig. 20). They found that, compared to a free jet seen in a vertical plane, the height of the shock was decreased and an oblique shock foot arose beneath the Mach disk. In nature, such a shock foot may have a ground signature, which may delimit the devastated zone. A scaling analysis applied to the Mount St-Helens blast suggested that the imprint of the Mach disk shock could be found at 4 to 9 km from the vent depending on vent dimensions and initial reservoir pressure.

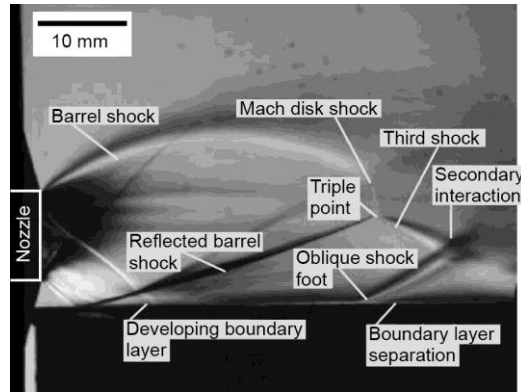


**Figure 20.** Jet generated by sudden release of a pressurized gas from a nozzle and impinging a horizontal rigid surface. Structures are seen as density gradients refract the light. Notice that the lower part of the Mach disk shock is reduced compared to a free jet. From Orescanin et al. (2014).

### 3.5.2 Dense flow regime

Particle interactions in dense (parts of) PDC with negligible to strong gas-particle interactions control energy dissipation, produce significant amounts of ash, and cause particle segregation. Particle collisions (i.e. normal motion) and friction (i.e. tangential motion) have been the focus of several studies involving volcanic clasts (Fig. 21). Cagnoli and Manga (2004) investigated pumice flows generated by a rotating disk between two vertical and coaxial cylinders. The flow structure consisted of a highly agitated basal layer and of a thicker upper layer with limited grain motions, or plug (Fig. 21a). In the basal layer, energy dissipation due to particle interactions, expressed as the dimensionless number

$$\Pi = \frac{\omega_d^2 - \omega_u^2}{\omega_u^2}, \quad (75)$$

with  $\omega_d$  and  $\omega_u$  the angular velocities of the rotating disk and of the upper layer, respectively, increased with the Savage number (see equation 6). Values of  $Sa$  generally  $>0.1$  indicated that energy dissipation occurred mainly through collisions, which generated increasing amounts of ash as  $Sa$  increased. Other studies showed that collisions caused energy dissipation that varied with the incidence angle (Cagnoli and Manga 2003, Dufek et al. 2009), produced ash mass at rates proportional to the square of the impact velocity (Dufek and Manga 2008), and generated the coarsest ash fractions (Mueller et al. 2015). In contrast, friction produced ash at rates increasing linearly with the flow velocity (Dufek and Manga 2008) and led to the finest fractions  $<10 \mu\text{m}$ , particularly when the pumices had high open vesicularity (Mueller et al. 2015). Manga et al. (2011) also showed that pumices abraded in a tumbler acquired a highest roundness once they had lost 15-60% of their initial mass, and that the abrasion rate decreased with time and with the crystal content.

Particles interactions were also shown to control the flow runout distance (or mobility). Experiments of Cagnoli and Romano (2010, 2012) on flows of angular rock fragments on an incline of given width ( $w$ ) and with slope angle decreasing downstream revealed that the apparent friction coefficient ( $\mu_a$ ), equal to the ratio of the drop height over the runout of the center of mass, decreased as the grain size ( $d_p$ ) decreased because smaller particles were less agitated and hence dissipated less energy per unit volume. In contrast,  $\mu_a$  increased with the product of  $d_p/w$  and  $V^{1/3}/w$ , two dimensionless numbers derived from scaling analysis, showing that the flow runout decreased with the volume of material released, which could be inherent to the non-constant slope angle. Breaks in slopes that are common in nature may be the sites of intense particle interactions that cause severe energy dissipation as well as flow deceleration and deposition. In this context, large-scale experiments showed that the flow runout increased because of lower energy dissipation as the slope angle of the upstream channel became closer to that of the depositional area (Sulpizio et al. 2016) and as the pumice-lithic volume ratio decreased (Rodriguez-Sedano et al. 2016).

Particle segregation is a direct consequence of grain interactions and may in turn exert a feedback on flow emplacement. Analogue experiments of Félix and Thomas (2004) on pumice flows showed that large particles were segregated upwards as a consequence of both kinetic sieving of the smaller particles and squeeze expulsion. These particles then moved preferentially toward the flow

margins to form lateral static borders, which delimited a central channel and formed levées once the material in the channel drained (Fig. 21c). The levée-channel morphology obeyed the following scaling law

$$\frac{U}{\sqrt{gh_l}} = \omega \frac{h_l - h_c}{h_c}, \quad (76)$$

with  $U$  the flow front velocity,  $\psi$  an empirical constant dependent on the type of granular material, and  $h_l$  and  $h_c$  the height of the levees and of the deposit in the channel, respectively. Despite uncertainties regarding applicability to natural flows (cf.  $\omega$ ), this scaling law is relevant for inferring the velocity of pumice flows from the morphological characteristics of their deposits (Jessop et al. 2012).

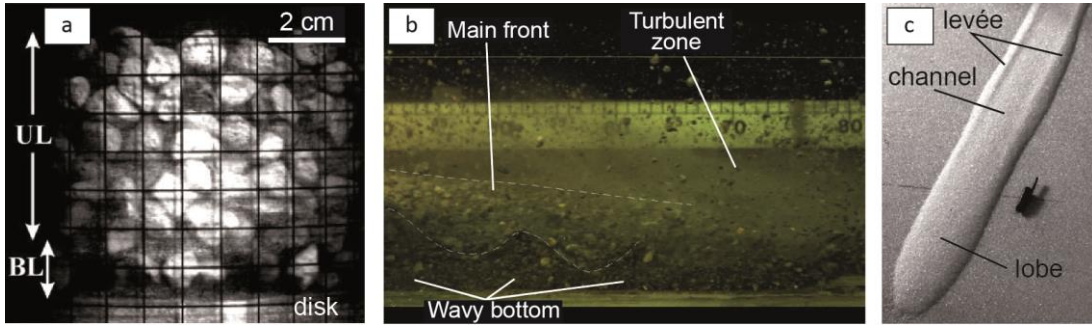


**Figure 21.** Experiments on dense granular flows. (a) Pumice flow generated by a rotating disk between two vertical cylinders, from Cagnoli and Manga (2004). (b) Flow of pyroclastic material down an incline and dominated by particle interactions, from Sulpizio et al. (2016). (c) Deposit with a frontal lobe and lateral levées delimiting a central channel, from Félix and Thomas (2004).

The role of interstitial gases in controlling the dynamics of dense PDC was recognized since the seminal studies of Anderson and Flett and of Lacroix on historical eruptions in the lesser Antilles islands in the early 1900's. McTaggart (1960) was the first to address this issue experimentally. He observed that hot sand flows travelled further than cold ones and he hypothesized that this was due to rapid heating and expansion of the ambient cold air entrapped by the hot flows, which caused high internal turbulence. Brown (1962) argued that the high mobility of PDC could rather be due to fluidization caused by gases released by the particles and percolating upwards. Since then the concept of fluidization by gases of internal or external sources in dense PDC has received much attention from experimentalists. Studies on static fluidized ignimbrite samples revealed particle size or density segregation features similar to those observed in natural deposits (Wilson 1980, 1984) and complete fluidization at gas velocities as low as  $\sim 1$  mm/s in materials at high temperatures ( $\sim 200^\circ\text{C}$ , Druitt et al. 2007). In addition to these works, the effect of fluidization on the dynamics of granular flows was addressed in various experimental configurations. The key physical parameter of fluidization is the interstitial pore fluid pressure that arises as a consequence of (i) vertical gas-particle differential motion and associated drag, which occurs when a gas of internal or external sources percolates upwards and/or when a granular mixture deflates and expels the interstitial gas upwards (Bareschino et al. 2008, Chédeville and Roche 2014, Breard et al. 2018, Lube et al. 2019), or (ii) sustained gas-particle relative oscillations that cause steady rotational fluid currents across a boundary layer around the particles, a phenomenon called acoustic streaming (Valverde and Soria-Hoyo 2015, Soria-Hoyo et al. 2019). Pore pressure reduces particle interactions and thus favors propagation of dense gas-particle mixtures. Once generated, and in absence of significant gas-particle differential motion, the pore pressure decreases according to a diffusion law and may persist for long duration in fine-grained materials with low hydraulic permeability owing to the high compressibility of the interstitial gas (Montserrat et al. 2012, Roche 2012, Breard et al. 2019). The Bagnold and Darcy numbers (equations 7-8) are relevant for describing the emplacement of dense PDC. Another useful dimensionless parameter is the pore pressure number (Iverson and Denlinger 2001),

$$Pr = \frac{(L/g)^{1/2}}{(h^2/D)}, \quad (77)$$

with  $L$  and  $h$  the typical flow length and height, respectively, and  $D = k/(1 - \epsilon_p)\eta\beta$  the pore pressure diffusion coefficient (with  $\beta$  the gas compressibility), which is the ratio of the pore pressure advection timescale (that scales with flow duration) over the pore pressure diffusion timescale.

Experiments on gas-particle flows applied to dense PDC have involved different configurations. Takahashi and Tsujimoto (2000) showed that flows down inclines generated by release of fine ( $\sim 80 \mu\text{m}$ ) sand heated at  $300^\circ\text{C}$  and mixed with sodium hydrogen carbonate, which generated  $\text{H}_2\text{O}$  and  $\text{CO}_2$  that escaped rapidly and fluidized the flow, could propagate on slopes down to  $\sim 5^\circ$  and much lower than the friction angle of the sand ( $\sim 30^\circ$ ). Granular flows with pore fluid pressure were also investigated in the dam-break configuration in order to allow for direct comparison with similar studies on fluid currents (see previous section). Roche et al. (2008) showed that flows at almost maximum particle concentration, generated by release of fluidized granular columns of height  $h_0$  onto a horizontal surface from which there was no external source of gas, propagated as currents of pure fluids if high pore pressure could be maintained for long durations due to the low hydraulic permeability (cf. small particle size and low Pr, Fig. 22). The fluid-like behavior was evidenced in particular as the flow Froude number (cf. equation 67) and the initial Froude number

$$Fr_0 = \frac{U}{\sqrt{g'h_0}}, \quad (78)$$

were respectively  $Fr \sim 2\sqrt{2}$  and  $Fr_0 \sim \sqrt{2}$  (note that  $g' \sim g$ ), indicating transfer of potential to kinetic energy through column collapse with negligible resistance and energy dissipation. The flows decelerated and eventually stopped when the pore fluid pressure became too low to buffer particle interactions, and the flow runout distance,  $x_f$ , and duration,  $t_f$ , scaled with the column height so that

$$x_f = c_1 h_0, \quad t_f = c_2 \sqrt{\frac{h_0}{g}}, \quad (79)$$

where  $c_1$  and  $c_2$  were empirical constants that increased with the pore pressure diffusion timescale. Other dam-break experiments with synthetic or pyroclastic material showed that the flow runout and duration increased with the initial amount of material expansion (Girolami et al. 2008, 2015), suggesting that flow deflation increased the pore pressure diffusion timescale, in agreement with experiments on static granular columns (Montserrat et al. 2012, Roche 2012, Breard et al. 2019). The experiments also revealed that deposition of the particles occurred through progressive aggradation whose rate decreased with the initial material expansion (Girolami et al. 2008, Roche 2012).

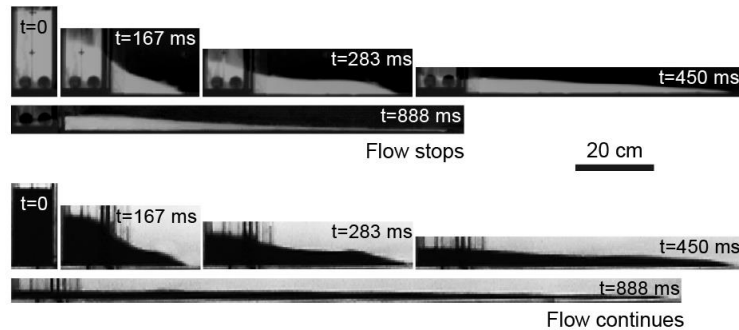


**Figure 22.** Fluid-like behavior of a dense dam-break granular flow with high gas pore pressure (top) evidenced through comparison with a similar inertial flow of water (bottom). From Roche et al. (2008).

### 3.5.3 Coupling of dilute and dense flow regimes

Large-scale experiments revealed how the dilute and the dense flow regimes can coexist in a current and they provided insights into the complex structure and processes of PDC (Lube et al. 2015, 2019, Breard et al. 2016, Breard and Lube 2017). The experiments simulated the formation of PDC from column collapse through release of pyroclastic material onto the base of a channel inclined at  $5\text{-}25^\circ$  (Fig. 23). They showed that, even at initial particle concentration of a few percent, the material released accumulated at the impact zone to form an aerated (i.e. with some pore pressure) dense basal underflow with particle concentration up to  $\sim 45 \text{ vol. } \%$  (see also Rowley et al. 2014). The dense flow had a less concentrated thin bottom part with concentration of  $\sim 20 \text{ vol. } \%$  and deposited particles through an aggradation process. It was overridden by a turbulent ash cloud with particle concentration less than  $\sim 1 \text{ vol. } \%$  and decreasing from the current head to the wake. Clusters of particles at intermediate concentrations arose in the cloud in a transition zone from where they settled to feed the underflow. In other experiments involving turbulent but quasi-static gas-particles mixtures in a vertical pipe, Weit et

al. (2018, 2019) showed that the emergence of settling clusters established a maximum particle concentration ( $C_{\max}$ ) in dilute mixtures. They found that  $C_{\max}$  was dependent on the particle Reynolds number,  $Re_p$ , according to  $C_{\max}=0.78 \times Re_p^{0.17}$ . This scaling law provided results in good agreement with those of Breard et al. (2016) and predicted maximum particle concentrations of ~2-5 vol. % for turbulent mixtures in nature (at  $Re_p \sim 10^2$ - $10^5$ ).

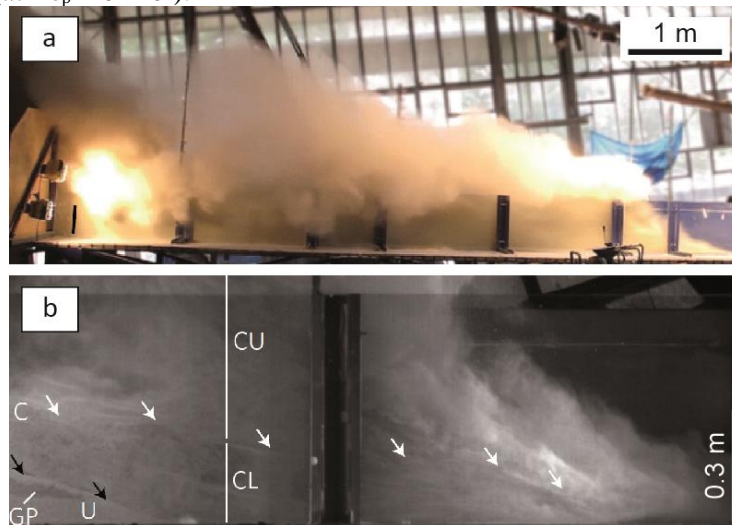


**Figure 23.** Analogue PDC in the large-scale PELE facility. (a) Side view. (b) Detailed side view of the current head showing the dense underflow (U) and the dilute ash cloud region (C) with middle (CL) and upper (CU) zones. Clusters at intermediate concentrations in zone CL settle from the cloud and entrap gas pockets in the underflow. From Breard et al. (2016).

### 3.5.4 Interaction of flow with boundaries

The mechanisms of interaction between PDC and topography may provide fundamental insights into the flow dynamics. Experiments of Bursik and Woods (2000) on confined dilute particle-saline currents in fresh water and at  $Re=10^3$ - $10^4$  revealed that constrictions or openings had no influence on the typical exponential decrease of deposit thickness even though the runout distance changed as the sedimentation rate varied with the channel width. Woods et al. (1998) further showed that in the subcritical regime (at  $Ri > 1$ ) relatively small topographic barriers did not affect flow propagation and sedimentation rate. In contrast, intermediate-size barriers blocked partially the flow, which was then reflected upstream and had enhanced sedimentation rate, and the current was totally blocked above a critical height that increased with the mass flow rate. Combined theoretical analysis suggested that dilute (parts of) PDC with typical flow rates of  $10^8$ - $10^9$  kg/s could scale barriers up to ~1000 m. Similar experiments of Andrews and Manga (2011) but with air as the ambient fluid revealed that currents with the same range of Reynolds numbers were blocked by topographic barriers higher than ~1.5 times their thickness. Doronzo and Dellino (2011) also showed that interaction with buildings could cause strong local turbulence increase as well as flow recirculation around the building and forced deposition in the back wall.

Erosion of granular substrates by PDC is increasingly recognized as a common phenomenon. In the dilute regime, wind tunnel experiments of Douillet et al. (2014) involving volcanic clasts of different morphologies showed that the critical air flow velocity and related shear stress required for remobilization of substrate particles depended weakly on the particle shape. In the dense regime, basal flow stresses may cause entrainment of large portions of the substrate rather than that of individual particles (e.g. Mangeney et al. 2010). Estep and Dufek (2012, 2013) used photoelastic techniques combined with discrete element simulations to investigate the network of contacts between the flow particles, defined as ‘force chains’ by granular physicists (Fig. 24a). Their experiments demonstrated that extreme forces were transmitted locally to the substrate and increased with the contact stiffness, suggesting that such forces were likely to cause erosion of natural substrates. Experiments of Roche et al. (2013) further showed that basal shear forces could cause extraction and entrainment at flow base of particles forming a granular substrate. Onset of uplift of these particles could then be promoted by a

local upward pore pressure gradient, and further upward motion into the flow interior was favored by internal forces. The pore pressure gradient arose as the flow head slid on the substrate and it was equal to

$$\Delta P = \gamma \rho U^2, \quad (80)$$

with  $\gamma$  an empirical constant dependent on the degree of fluidization of the flow,  $\rho$  the bulk flow density, and  $U$  the flow front velocity (Fig. 24b). It is possible to derive an empirical law that gives the flow velocity as a function of the characteristics of the particles uplifted and transported downstream,

$$U = \sqrt{\frac{\xi(\rho_p - \rho_g)gL}{\gamma\rho}}, \quad (81)$$

with  $\xi$  a shape factor that varies from 2/3 (ellipsoid) to 1 (parallelepiped) and  $L$  the shortest length of the particles. Application to natural cases showing evidence of entrainment of blocks of size up to ~1 m allows to infer typical velocities of dense basal parts of PDC of ~10-30 m/s (Roche et al. 2013, 2016).

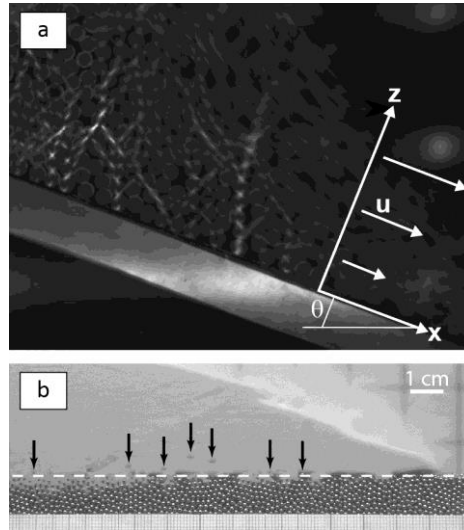


**Figure 24.** Interaction of dense granular flows with their substrate. (a) Force chains in a flow of 6 mm diameter beads, Estep and Dufek (2012). (b) Uplift of particles extracted from a granular substrate and dragged at flow base (arrows), Roche et al. (2013).

Water is another natural boundary with which PDC may interact (Dufek et al. 2009). Freundt (2003) investigated the entrance of dense PDC into the sea and found that high temperature and poor sorting of the volcanic material were essential in controlling the flow behavior. The experiments were scaled considering the dimensionless numbers typical of granular flows (see section 2), the ratios of geometric parameters involving the flow length and flow depth as well as the water depth ( $H_w$ ), and three additional numbers

$$t^* = \frac{t}{L/c}, \quad Fr^* = \frac{U}{c}, \quad q^* = \frac{Q}{cH_w}, \quad (82)$$

with  $t$  the flow duration,  $L$  and  $U$  the flow length and velocity,  $c=(gH_w)^{1/2}$  the speed of shallow water waves, and  $Q$  the volume flux. The values of the numbers in experiments were fairly close to those in nature, except for the dimensionless flux  $q^*$ . The experiments revealed tsunami waves in all cases and a clear partitioning between a fine ash cloud surge over the water surface and a dense basal flow that mixed with water and then formed a turbidity current. High material temperature led to the formation of a third flow component that propagated beneath the water surface and also to more powerful and laterally extended steam explosions. Dufek et al. (2007) investigated steam production by quantifying heat transfer when hot (100-700°C) pumices were dropped into water. They showed that ~10% of the thermal energy of the pumices caused steam production, whose rate varied inversely with the cube of the pumice diameter. Complementary modelling suggested that littoral blasts could be generated if particles were smaller than ~1-5 mm. Another possible scenario to explain the presence of welded ignimbrites in shallow submarine environment is the displacement of the shoreline by dense PDC. This issue was addressed by Legros and Druitt (2000) through experiments involving a fluid current flowing into a

slightly lighter or denser ambient fluid. They found that a steady current was able to push back the entire layer of ambient fluid over a distance

$$R = \frac{QH_w}{\alpha Fr \sqrt{g' H_w^5}}, \quad (83)$$

with  $Q$  volume flow rate,  $H_w$  the sea depth,  $\alpha$  the radial angle of entrance of the current into the ambient fluid,  $Fr$  the flow Froude number, and  $g'$  the reduced gravity. Application to natural cases suggested shoreline displacements of a few kilometers for dense PDC of the order of  $10 \text{ km}^3$ .

### 3.6 Lava flows and domes

Lava flows form where a dense mixture of silicate liquid, crystals and gas bubbles spread on the Earth's surface as hot, slow-moving gravity currents until cooling and complete solidification cause their arrest. Laboratory experiments have been extensively carried out to investigate the parameters that influence the flow behavior (Supplementary Table S4) and are now used to perform benchmarking exercises (Cordonnier et al. 2016, Dietterich et al. 2017). These experimental studies focused on four main objectives: (i) to determine the rheology of a lava flow, (ii) to interpret lava flow morphology and thermal signature in terms of eruption dynamics, (iii) to study the interactions of lava flows with their environment, and (iv) to understand the dynamics of lava domes formation.

#### 3.6.1 Lava rheology

The rheology of lava primarily depends on its composition, temperature, crystal and bubble contents, which are highly time-dependent as a result of cooling, crystallization and vesiculation during the flow propagation (Griffiths 2000). Several approximations have been tested experimentally to describe lava rheology by using Newtonian viscous fluids (Sakimoto and Gregg 2001) and non-Newtonian viscous fluids with a Bingham (Hulme 1974), Herschel-Bulkley (Castruccio et al. 2010, 2014) or thixotropic behavior (Bagdassarov and Pinkerton 2004). In a general form, the shear stress ( $\sigma$ ) and strain rate ( $\dot{\epsilon}$ ) of the flow are related by:

$$\sigma = \sigma_0 + K_v \dot{\epsilon}^n, \quad (84)$$

where  $K_v$  is the consistency (i.e., a measure of the effective viscosity),  $\sigma_0$  is the yield stress to overcome before flowing, and  $n$  is the flow index, which characterizes the degree of non-Newtonian behavior. For  $n > 1$ , the fluid rheology is shear-thickening, whereas for  $n < 1$  the fluid rheology is shear-thinning. The law reduces to the Newtonian case when  $\sigma_0 = 0$  and  $n = 1$ , and to the Bingham case when  $\sigma_0 > 0$  and  $n = 1$ .

Hulme et al. (1974) presented the first laboratory experiments to study the behavior of a suspension of fine particles of kaolin in water released through an orifice at the top of an inclined plane (Fig. 25a). They observed the formation of levées whose characteristics (width and depth) were compared to the predictions made with a model for the flow of a Bingham fluid. The relatively good agreement between the predictions and the measurements led the authors to apply their model to terrestrial and lunar lava flows in order to retrieve their yield stresses and flow rates from their morphology. Sakimoto and Gregg (2001) cast some doubts on these results and proposed new laboratory experiments in which polyethylene glycol (PEG) wax was released into a tank filled with sucrose solution (Fig. 25b). Measurements of flow velocity were compared to the predictions from an analytic solution for isothermal Newtonian flow in a rectangular channel. The analytic solution agreed well with the laboratory measurements, leading the authors to apply their model to several submarine and subaerial terrestrial and extraterrestrial channeled lava flows in order to estimate the viscosity from the measured channel dimensions and assumed lava properties.

Castruccio et al. (2010) pointed out that a Herschel-Bulkley rheology may be more appropriate to describe the behavior of a crystal-bearing lava flow. They performed dam-break experiments by releasing a mixture of golden syrup and syrup crystals. Measurements of the flow front position with time were used to parameterize the values of  $K_v$ ,  $n$  and  $\sigma_0$  in equation 84 as a function of the crystal content. The results showed a non-Newtonian shear-thinning behavior for crystal concentrations larger than 30% with  $n$  values decreasing from 1 (Newtonian behavior) to 0.5 at a concentration of 60%. Experiments also revealed that the rheology of suspensions depended on the particle size distribution.

Applying the new parametrizations to lava flows at Etna volcano gave predicted velocities in good agreement with natural velocities. Castruccio et al. (2014) extended this work with further experiments involving Herschel-Bulkley fluids released through a nozzle at the top of an inclined tank (Fig. 25d). The scaling analysis was made using the Reynolds number ( $Re = 10^{-8} - 10^{-3}$ ) and a modified Grashof number ( $10^{-1} - 10^3$ ), as well as a geometric aspect ratio ( $H/W = 0.05 - 0.3$ , where  $H$  and  $W$  are the flow thickness and width, respectively), and the Bingham number ( $B = 0 - 50$ ) such as:

$$B = \frac{\sigma_0 L}{\eta U}, \quad (85)$$

where  $U$  and  $L$  are the characteristic velocity and length scales, respectively, and  $\eta$  is the fluid viscosity. Measurements of flow thickness and velocity were compared to predictions made with a 2D model for the flow of a Herschel-Bulkley fluid and found in good agreement. The model was then applied to the Etna lava flows to calculate the flow velocity and effusion rate from the final flow dimensions and rheology based on the crystal content and glass composition of samples. The predicted flow rate was remarkably close to the actual measurements.

The effect of bubbles concentration on lava rheology was investigated experimentally by Bagdassarov and Pinkerton (2004) who used a rotational van-viscometer to measure the viscosity of aerated golden syrup suspensions. The stress-strain curves determined experimentally revealed that bubbly suspensions were thixotropic, visco-elastic fluids with yield strengths (i.e.,  $\sigma_0 > 0$  and  $n < 1$  in equation 84). The deformation of vesicles during the flow may therefore cause a decrease in apparent viscosity, resulting in acceleration and thinning of the flow. This phenomenon was expected to occur where the flow encountered a steep gradient, and its effect on the lava rheology was described by a bubble elongation parameter  $\lambda$  that depended on the capillary number ( $Ca$ ).

The difficulty of choosing analogue materials with the same rheology as lava flows has now been partially overcome by using actual lavas. Lev et al. (2012) presented large-scale laboratory experiments in which molten basalt at  $1300^\circ\text{C}$  was poured from a furnace on a sloping plane (Fig. 25c). The scaling analysis was made using the Reynolds ( $Re = 0.7$ ), Peclet ( $Pe = 10^5$ ), and Froude numbers ( $Fr = 10^{-2}$ ). Measurements of flow velocity and temperature were made and compared to theoretical predictions of various models with different rheologies. The results suggested that at high temperature a weakly shear-thinning or a Newtonian rheology best explained the data.

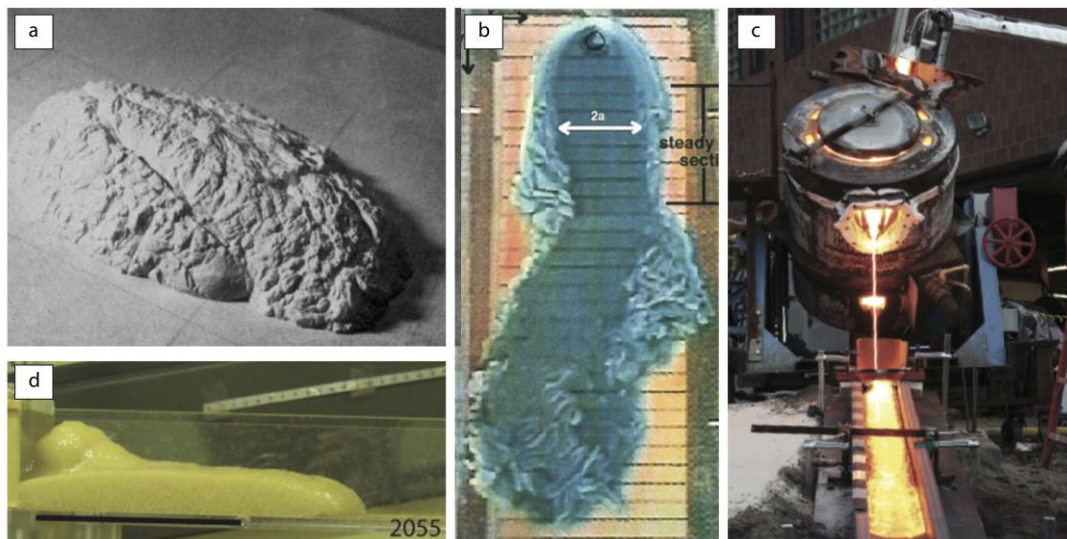


**Figure 25.** Laboratory lava flows. (a) Water and kaolin (modified from Hulme, 1974), (b) polyethylene glycol (modified from Sakimoto and Gregg, 2001), (c) molten basalt (modified from Lev et al., 2012), (d) particle-laden golden sugar (modified from Castruccio et al., 2014).

### 3.6.2 Lava flow dynamics

Laboratory experiments were designed to study the effect of a solidifying crust on the surface morphology and dynamics of lava flows. Fink and Griffiths (1990) injected polyethylene glycol wax (PEG) at the base of a tank containing cold sucrose water to reproduce the mechanism of heat loss in

lava flows. Their results showed that no solidification occurred in the warmest experiments, whereas reducing the initial temperature difference between the flow and the ambient or the intrusion rate gave rise a variety of surface morphologies. The main controls on the flow behavior were identified as the Peclet number ( $Pe = 10^2 - 10^3$ ) and the dimensionless timescale for solidification  $\Psi$ . Increasing progressively the  $\Psi$  number led to the formation of either bulbous lobate forms similar to pillow lava ( $\Psi < 0.7$ ), rigid plates with divergent rift structures ( $\Psi < 2.5$ ), folding plates with many small transverse structures ( $\Psi < 6$ ), levees at the edges of the flow ( $\Psi < 16$ ), or no solidification ( $\Psi > 16$ ) (Fig. 26a). Fink and Griffiths (1992) extended this work by performing additional experiments with a point source and a rough surface at the base of the tank, and with a linear source and a smooth or rough tank base. The results showed no significant effect of the source geometry and roughness of the ground on the surface morphology of the flows, reinforcing the confidence in the robustness of the  $\Psi$  criterion for the various morphologic transitions. Increasing the slope in these experiments led to decrease the transitional  $\Psi$  values by up to 50% (Gregg and Fink, 2000) but the conclusions remained unchanged. Stasiuk and Jaupart (1997) presented a new model to interpret the morphology of lava flows in terms of magma system conditions. They showed theoretically that the accumulation of lava above the vent tends to increase the pressure and to reduce the eruption rate, which in turn controls the evolution of the lava flow volume and thickness with time. The model was tested against a series of laboratory experiments in which glucose syrup, whose viscosity strongly varied with temperature, was injected into air. Comparison of the model predictions and measurements of flow shapes revealed a good agreement (Fig. 26b) suggesting that the model captured the controls of the physical conditions in the chamber on the dynamics of lava flows. Stasiuk et al. (1993) used a similar apparatus to inject glucose syrup at the base of a tank containing a cold aqueous solution in order to investigate the influence of cooling on the lava bulk viscosity. The results showed that the bulk viscosity primarily depended on the Peclet number, on the formation of a skin at the lava surface by cooling, and to a lesser extent on the eruption viscosity.

The formation of a crust by cooling was early identified as a critical phenomenon in lava flows, and its influence on the flow dynamics was largely studied experimentally. Griffiths et al. (2003) performed dam-break experiments in which PEG was injected into a sloping tank containing cold salt water, and they observed three dynamical regimes depending on the source conditions. In the 'tube' regime, a rigid solid roof formed over the flow while the melt continued to flow through an encased tube beneath. In the 'mobile crust' regime, a solid surface crust developed only in the axis of the channel but remained mobile. In the transitional regime, the behavior was intermediate. The transition between the regimes was mainly controlled by the Rayleigh number ( $Ra = Gr \times Pr$ ) and the dimensionless timescale for solidification  $\Psi$  identified by Fink and Griffiths (1990) (Fig. 26c). Combining these two parameters gave a single criterion  $\mathcal{G}$  separating the tube ( $\mathcal{G} < 25$ ) and mobile crust regimes ( $\mathcal{G} > 25$ ). Blake and Bruno (2000) used a similar experimental set-up to study the transition from a uniform lava flow to a compound lava flow where a succession of breakouts occurs at the flow front. The results showed that this morphological transition corresponded to a dynamical transition between a viscous flow regime and a surface crust controlled flow regime. Lyman et al. (2005) performed similar experiments with PEG or PEG-kaolin slurries and identified that four dynamical regimes can arise in spreading lava flows. In solidifying flows with no internal yield strength, the flow moved initially at a constant velocity in a slumping regime, and then decelerated in a viscous regime before entering a final regime where the yield strength of the growing crust stopped the flow. They also showed that solidifying flows with internal yield strength can be stopped by either the internal yield strength or the growing surface crust. Lyman and Kerr (2006) extended this work to investigate the effect of slope and identified four dynamical regimes for solidifying flows with no internal yield strength: an inertial slumping regime, a horizontal viscous regime, a sloping viscous regime, and a crust yield strength regime that finally stopped the flow. Flows with internal yield strength may also follow a sloping viscous regime, which arose immediately or followed the slumping regime. Box models predicted the runout distance reached by the flow in these different regimes.

The formation of channelized lava flows by cooling and its impact on the flow dynamics were also investigated experimentally. Kerr et al. (2006) extended the experiments of Griffiths et al. (2003) to a larger range of Peclet number ( $Pe = 10^4 - 10^5$ ) and Reynolds number ( $Re = 10^{-1} - 1$ ) in order to generate relatively wide flows. The experiments reproduced the tube, mobile crust and transitional regimes identified by Griffiths et al. (2003) with a critical parameter  $\mathcal{G} = 20$  separating the tube and

mobile crust regimes. In this new set of experiments, the flows spread rapidly down the slope but slowly across it, allowing the strength of the growing crust to stop the lateral motion and to form a channelized lava flow. Channel widths were observed to increase for smaller slopes and for larger flow rates, a result consistent with their scaling analysis. Cashman et al. (2006) also extended the experiments of Griffiths et al. (2003) to study the effect of channel irregularities (i.e., expanding, contracting, or meandering channels, and channel with bottom irregularities) on crust formation and disruption. Local changes in channel width, sinuosity, and topography forced the flow to decelerate or accelerate, promoting locally either the tube or mobile crust regime. Overall, the transition between the two regimes was found to be well captured by the criterion  $\Psi = 25$  determined by Griffiths et al. (2003) for straight, uniform channels.

Most of laboratory studies on lava flows were designed to interpret the experimental results on flow morphology in terms of eruptive parameters for the natural case (such as eruption rate, yield strength...). Garel et al. (2012) reproduced axisymmetric isoviscous gravity currents with hot silicone oil in order to find a link between eruption rates and surface thermal signals. They showed that the surface thermal signature of the flow became steady after an initial transient stage. Their new theoretical model was found to capture the experimental results and suggested that the order of magnitude of the effusion rate can be retrieved from radiated power of the lava flow. An additional set of experiments was designed to quantify the impact of wind on lava flow cooling and on the resulting link between surface thermal signal and effusion rate (Garel et al., 2013). The cooling induced by wind was found to reduce the thermal power radiated by lava flows for a given effusion rate. Garel et al. (2014) further investigated the feedback of cooling on the flow dynamics with a new set of laboratory experiments using PEG (Fig. 26d). The experiments revealed a large variety of flow morphologies for a given supply rate, but the supply rate of the PEG could still be retrieved from the surface thermal signature radiated from the hottest part of the flow, as in Garel et al. (2012). The authors pointed out, however, that the uncertainty in this estimation was always large (about 50%) because of the complexities associated with the solidifying lava flows. Garel et al. (2016) performed additional laboratory experiments and concluded that a thermal proxy could only yield a minimum and time-averaged estimate of the effusion rate.

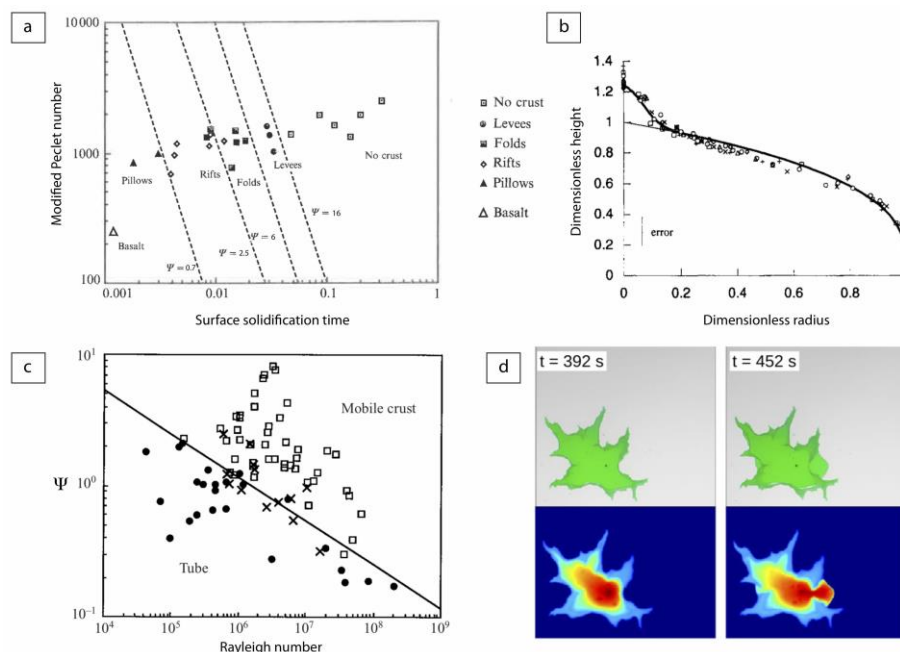


**Figure 26.** Dynamics of experimental lava flows. (a) Type of PEG flows as a function of the Peclet number and solidification time (modified from Fink and Griffiths, 1990). (b) Dimensionless flow shape from syrup experiments (symbols) compared to theories (lines) (modified from Stasiuk and Jaupart, 1997). (c) Type of PEG flows as a function of  $\Psi$  and the Rayleigh number (modified from Griffiths et al., 2003). (d) Visible and thermal images during a PEG experiment (modified from Garel et al., 2014).

### 3.6.3 Structures in lava flows

Internal strain within lava flows arises due to a combination of forces that may result in folds and fractures. Laboratory experiments were designed to interpret strain measurements in terms of emplacement mechanisms. Canon-Tapia and Pinkerton (2000) did measurements of the anisotropy of magnetic susceptibility (AMS) on lava samples that were melted and subjected to several strain rates and cooling histories. The results showed that the degree of anisotropy was closely related to their internal deformation, but also that the timing of shearing relative to solidification was important since only the last phase of deformation was detectable using AMS. The authors concluded that flow directions can be inferred confidently using this technique. Merle (1998) proposed a series of experiments to carefully observe the deformation of a silicon slab (Fig. 27a). The scaling analysis was made using the ratio of the gravity and viscous forces, the Reynolds number  $Re = 10^{-11}$ , and a geometric aspect ratio. Depending on the presence of a basal slope, the viscous flow produced either convex or complex (i.e., changing with time from convex through sigmoidal to concave) stretch trajectories. Strain components were measured in the experiments and provided an explanation for the formation of fold during motion. Lescinsky and Merle (2005) extended this work by adding a crust made of sand and plaster in their experiments to characterize the effect of surface crust rheology on the internal strain of lava flows (Fig. 27b). The scaling analysis was made using eight dimensionless numbers including the Reynolds number ( $Re = 10^{-8}$ ). The results suggested that changes in effusion rate had a major control on pure shear: whereas constant effusion rates produced simple shear, increasing or decreasing effusion rates caused compression or extension due to flow thickening or thinning, respectively. Experiments with a brittle crust were also found to reproduce fracture patterns similar to those of natural lava flows. Applegarth et al. (2010) built on these experiments and scaling analysis to investigate the effect of crustal thickness and basal slope on the propagation of channelized flows. The experiments exhibited two main behaviors depending on the ratio of the crustal thickness to total flow thickness ( $\Pi_1$ ). As  $\Pi_1$  increased, the influence of crustal strength with respect to viscous resisting force increased, leading to more deformation. At low  $\Pi_1$ , ductile structures were present (i.e., folds), whereas at intermediate and high  $\Pi_1$ , brittle structure appeared (i.e., crustal fracturing and avalanching). The influence of shear rate and crystallinity on the deformation regimes was investigated experimentally by Soule and Cashman (2005) who used a coaxial Couette rheometer. The results showed that high-concentration particle suspensions can reduce the flow velocity, localize shear stress, and promote break-up. The authors suggested that the transition from pahoehoe to aa lava flows may be controlled by a combination of shear rate and crystallinity dependence.

Fractures in lava flows commonly lead to the production of polygonal columnar joints. Desiccation experiments largely helped in understanding the mechanisms responsible for the formation of these intriguing features. Müller (1998a,b) desiccated starch-water mixtures and showed that columnar joints are essentially formed by contraction of lava flow during solidification (Fig. 27c). In the experiments, water was removed by diffusive processes producing tensile-crack patterns similar to those of natural flows. The results showed that the form of the columnar joints was mainly hexagonal (50% of the experiments), pentagonal (30%) or heptagonal (15%). Toramaru and Matsumoto (2004) performed more desiccation experiments to understand the effect of cooling rate on the morphology of the columnar joints. The dominant polygon shape was found to be pentagonal for high cooling rates, and hexagonal for low cooling rates. The authors proposed a simple model to link the average area of columns and the cooling rate for natural columnar joints. The effects of compressional and tensional forces on the formation of columnar joints were investigated experimentally by Lodge and Lescinsky (2009). Compressional experiments resulted in the formation of fractures with larger length parallel to the direction of deformation. Tensional experiments produced zones of horizontal columns that were similar to lava-ice contacts. The fracture patterns in their experiments can be used as an indicator for emplacement conditions of lava flows.

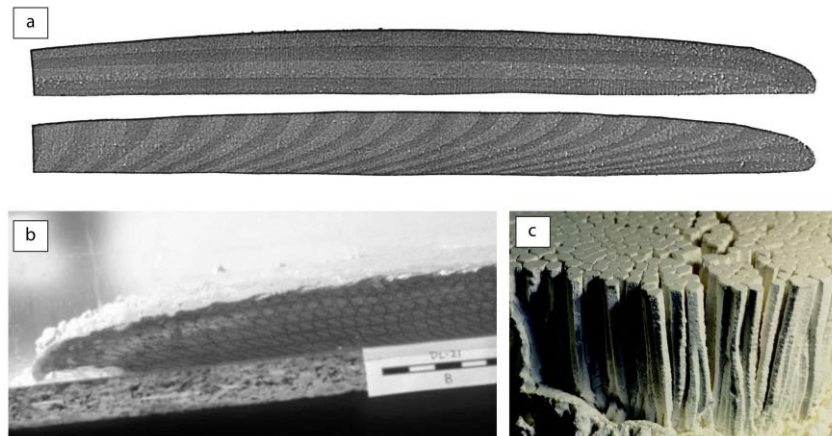


**Figure 27.** Structures in experimental lava flows. (a) Cross sections showing the deformation of horizontal and vertical markers (modified from Merle, 1998), (b) Side view of a flow of silicone with a plaster surface crust showing the deformation of strain grids (modified from Lescinsky and Merle, 2005), (c) Side view of starch columns (modified from Müller 1998a).

### 3.6.4 Lava interaction with environment

Lava flow commonly interact with natural (i.e., ice, seawater) and artificial (i.e., roads, houses) objects during their propagation. Dieterich et al. (2015) conducted laboratory experiments with syrup or molten basalt to study the interaction of lava flows with V-shaped and oblique obstacles with varying internal angles and orientations (Fig. 28a). The results suggested that tall orthogonal barriers or long V-shaped barriers with small internal angles could be used to slow down a lava flow. Highly oblique barriers were found to be the most efficient method to reroute a lava flow that will, in turn, accelerate. Kerr (2009) showed experimentally and theoretically that thermal erosion of the ground can occur where basaltic lava flows propagate. The experiments consisted in injecting a hot sucrose solution on top of a layer of solidifying wax. The flow of the sucrose solution caused thermal erosion of the underlying wax, which released in turn buoyant plumes of melted wax within the flow (Fig. 28c). A steady thermal erosion velocity was then reached, driven by the convective heat transfer from the lava to the ground and by natural compositional convection as the melted ground rose into the flow. This erosion velocity was limited near the source by the buoyant instability of the melted ground and by the freezing temperature of the flow at larger distances from the source. Similar results were obtained by Huppert et al. (1984) who studied the emplacement mechanisms of komatiite lavas. They used aqueous solutions cooled from above to reproduce the spinifex texture of komatiite by crystallization. Their results showed that komatiites probably behaved as turbulent flows and melted and assimilated underlying ground to form deep thermal erosion channels.

The interaction of lava flows with water (i.e., seawater or ice/snow) was investigated experimentally by Griffiths and Fink (1992), Gregg and Fink (1995), and Edwards et al. (2013). Griffiths and Fink (1992) used the same experimental device as Fink and Griffiths (1990) to produce various morphologies on the surface of wax extruded beneath cold water. The parameter  $\Psi$  introduced by Fink and Griffiths (1990) was then used to interpret the observed morphologies of submarine lava flows in terms of eruptive dynamics. The results showed that submarine lava flows mostly likely formed into pillow, whereas other morphologies could be attained if the eruption rate was increased or the viscosity was decreased. Gregg and Fink (1995) performed additional experiments to investigate the effect of a slope and found that increasing the latter parameter led to a progression of the flow type from pillows to lobate flows. The authors pointed out the difficulty of inferring eruptive parameters (i.e., effusion rate and emplacement times) from the morphology of submarine lava flows, which would require to know the total volume, viscosity, eruption temperature, and underlying slope. Edwards et al. (2013) investigated ice/snow-water interactions by pouring molten basalt on top of layers of ice using the same experimental device as Lev et al. (2012). The results showed that the lava was able to propagate on ice until the ice substrate melted and the lava sank into it (Fig. 28b). Close observations revealed that gas cavities in lava flows may arise as a result of the introduction of external water. The bubble production

was found to be more vigorous when the lava flowed directly on ice compared to experiments where a thin layer of sand was present above the ice.

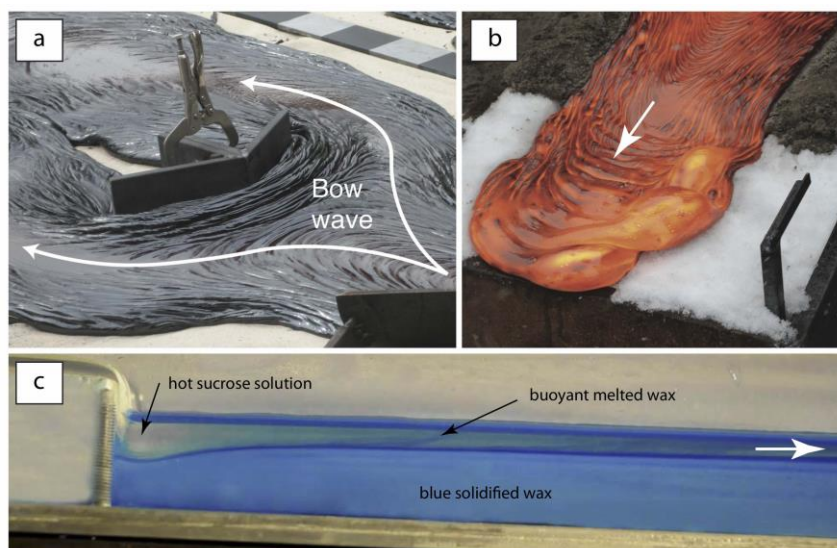


**Figure 28.** Interaction of lava flows with environment. (a) Post-emplacment photograph of molten basalt that encountered a V-shaped barrier (modified from Dieterich et al., 2015). (b) Laboratory molten basalt flowing over snow (modified from Edwards et al., 2013). (c) Thermal erosion experiment (modified from Kerr, 2009). White arrows indicate the main flow directions in all panels.

### 3.6.5 Lava domes

Experimental studies on lava domes mostly focused on the effects of lava rheology on the morphology of the resulting dome. Griffiths and Fink (1993) performed laboratory experiments in which PEG wax was injected at the base of a tank containing cold water. The formation of a thin crust by solidification due to cooling was found to be of primary importance on the flow dynamics. The dimensionless parameter  $\Psi$  identified by Fink and Griffiths (1990) for lava flows captured well the morphological transitions of the resulting lava domes. For  $\Psi > 80$ , a classical viscous-buoyancy balance controlled the flow dynamics. For lower  $\Psi$  values, the flow became dominated by the yield strength of the thin crust, which balanced the driving buoyancy force. At small effusion rates ( $\Psi < 3$ ), the dynamical balance became controlled by overpressure and tensile strength in the crust. Scaling analyses suggested that the rheology of the crust became dominant when the ratio of crust thickness to flow length was greater than the ratio of the crust's yield stress to the basal shear stress exerted on the flow. Comparison of the new scaling laws with the laboratory experiments and data for the Mount St-Helens and Soufriere lava domes revealed a fairly good agreement. Griffiths and Fink (1997) performed additional experiments with Bingham fluids in order to study the effect of a yield strength on their previous results. For this, they injected slurries of PEG and kaolin beneath cold water. The experiments revealed four dynamical regimes that were not observed in their previous study: axisymmetric, lobate, platy, and spiny. An equivalent  $\Psi_B$  number was found to capture well the transition between the flow regimes (Fig. 29a). However, the important difference of behaviors observed between the experiments with a Bingham or a Newtonian fluid clearly showed that the presence of a yield strength had a major impact on the flow dynamics. Balmforth et al. (2000) further investigated this effect by using water-kaolin slurries with a Herschel-Bulkley rheology. The experiments were scaled using the Reynolds ( $Re = 1$ ) and Bingham numbers ( $B = 100$ ). Laboratory measurements of dome height and radius were found to be in good agreement with their theory, confirming the importance of yield strength on the dynamics of lava domes.

The evolution of internal strain in lava domes was investigated experimentally in order to interpret observations of natural domes. Buisson and Merle (2002) produced laboratory lava domes by injecting silicone putty from a point source on a horizontal plane (Fig. 29b). Measurements of particle trajectories and velocity gradients showed that the overall geometry of the dome was controlled by a balance between the injection rate and gravity leading to a zonation of the dome in which flow direction

and strain rates differed. Zavada et al. (2009) performed similar experiments by injecting from a point source slurries of plaster and water on top of a layer of sand (Fig. 29c). Dilute mixtures of slurry were found to behave similarly to the previous laboratory domes (Buisson and Merle, 2002). However, concentrated mixtures with higher viscosity resulted in more complex dome evolutions similar to those of natural lava domes.

The morphologies of lava domes reproduced in the laboratory have been used to infer some important eruptive parameters from real time observations of actual lava domes. Huppert et al. (1982b) injected silicone oil from a point source on a horizontal plane and compared the measurements of dome height and radius as a function of time to their theoretical predictions of dome growth. The model was found to capture the experiments, and was then applied to estimate the effective viscosity of natural domes, which mainly controlled the dome geometry. Fink and Griffiths (1998) used their experimental results (Griffiths and Fink, 1997) to determine the  $\Psi_B$  number of several historical, prehistorical and extraterrestrial lava domes from their morphologies, and to estimate the yield strengths and eruption rates. Lyman et al. (2004) extended this work to include the effects of topography and they found that each morphology formed at lower values of  $\Psi_B$  number than it would on a horizontal surface (Griffiths and Fink, 1997), except for slopes larger than  $40^\circ$ , above which the transitions between morphologies became independent of the slope angle.

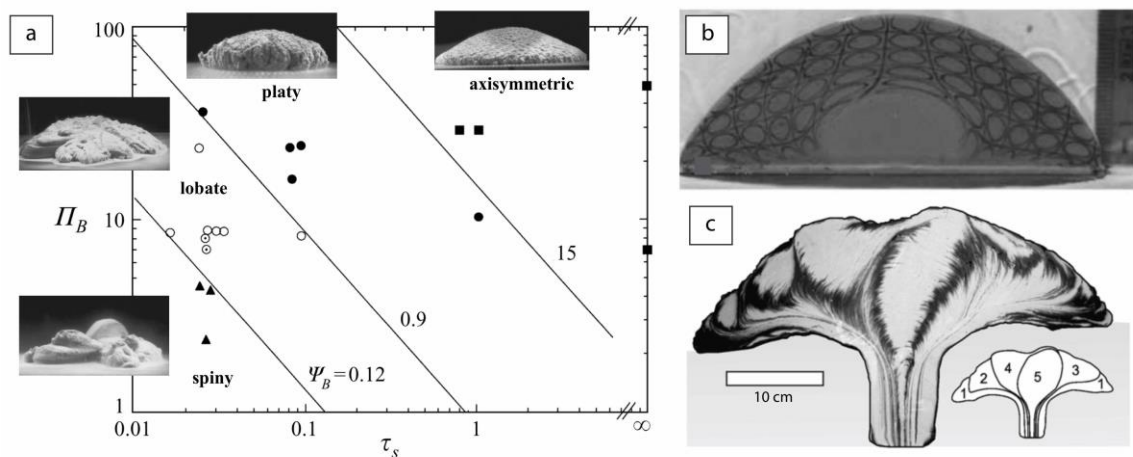


**Figure 29.** Laboratory lava domes. (a) Flow regimes for different values of  $\Psi_B$  number (modified from Griffiths and Fink, 1997). (b) Deformation in an analogue lava dome of silicone putty (modified from Buisson and Merle, 2002). (c) Deformation in an analogue lava dome of a slurry of plaster and water (modified from Zavada et al., 2009).

### 3.7 Studies on other volcanic phenomena

#### 3.7.1 Debris avalanches

The physics of debris avalanches, as well as that of other rock avalanches, is poorly understood. A well-known property of debris avalanches, however, is their high mobility characterized by runout distances up to several orders of magnitude longer than their drop height, which suggests low energy dissipation during emplacement. Flow mobility similar to that in nature cannot be reproduced in experiments involving dry granular materials, suggesting that (i) debris avalanches are granular mixtures but a scaling issue is unresolved yet and/or that (ii) phenomena such as basal melting and/or pore fluid pressure reduce friction. This is why steep inclines are used in experiments on debris avalanches in order to confer high flow inertia and generate elongated deposits. Experimental studies have evidenced two emplacement mechanisms.

The first mechanism is basal sliding and spreading of the granular mass with moderate internal motion. In experiments of Dufresne (2012) with various granular materials, sliding and associated stresses at the avalanche base could cause substrate entrainment, and the amount of erosion increased as

the frictional resistance and the roughness of the substrate decreased or increased, respectively. Tests on natural rock samples have shown that strain localization and associated heating could cause frictional melting, which decreased significantly the shear stress (Lavallée et al. 2012). Surface structures also provide insights into the emplacement mechanisms from flow initiation to deposition. Shea and van Wyk de Vries (2008) released cohesive granular materials on a curved smooth ramp and scaled their experiments considering the following dimensionless runout, strength, and initial energy

$$\frac{L}{V^{1/3}}, \quad \frac{\tau_0}{\rho g V^{1/3}}, \quad \frac{H}{V^{1/3}}, \quad (86)$$

with  $L$  and  $V$  the avalanche runout and volume,  $\tau_0$  the material cohesion, and  $H$  the fall height. They observed different types of surface structures (Fig. 30a). Hummocks formed as a consequence of different cohesions of the initial layers in the granular pile released, and they resulted from spreading and were delimited by normal faults (see also Paguican et al. 2012). Shear structures appeared at different times of emplacement. Normal faults formed preferentially at early stages as the material spread, thrust faults rather formed at late stages when the material accumulated on lower slopes, and strike-slip faults were caused by differential motion essentially at flow margins (see also Dufresne and Davies 2009). Similar structures in natural debris avalanche deposits support the model of a sliding brittle plug-like flow.

Longitudinal ridges oriented (sub-)parallel to the flow direction, aligned radially from the source and forming topographic highs are also found in some debris avalanche deposits. They suggest emplacement through a granular flow mechanism with significant internal motion, as demonstrated by some experimental studies (cf. Dufresne and Davis 2009). Valderrama et al. (2018) found that longitudinal ridges may result from the mechanism of granular fingering discovered by granular physicists (Fig. 30b). Their experimental flows of bidisperse mixtures revealed that particle size segregation caused front instabilities that generated series of adjacent internal secondary flows with coarse-rich static borders. These borders merged to finally form longitudinal ridges in the deposits once the material between the borders drained. Notice that the morphology of these secondary flows is similar to that of flows generated from a point source and forming levées-channel deposits (see Fig. 21c).

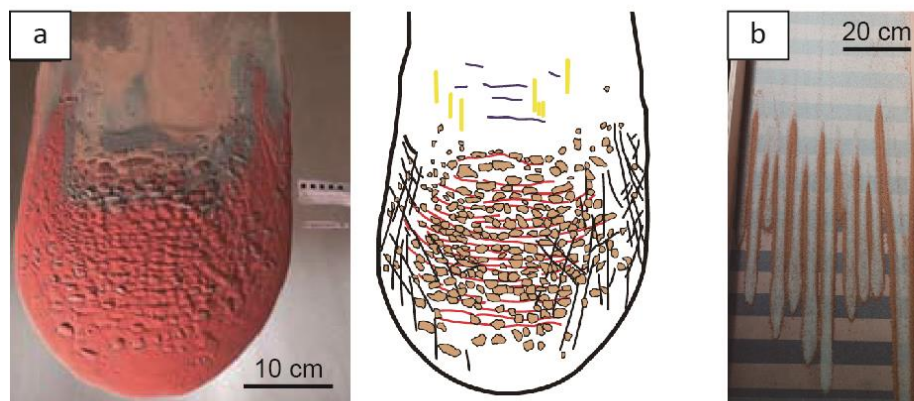


**Figure 30.** Surface structures of experimental debris avalanche deposits. (a) Hummocks and faults (Shea and van Wyk de Vries 2008). (b) Granular fingers (Valderrama et al. 2018).

### 3.7.2 Phreatomagmatic and hydrothermal eruptions

External water may contribute to trigger explosive eruptions when it is heated and transformed into vapor that expands rapidly. Direct interaction between water and a hot magma during phreatomagmatic eruptions causes fragmentation of the melt and disruption of the host rock, which generates maar-diatreme structures when explosions occur at relatively shallow levels. Fundamental aspects of thermal explosions involving mixing of water and magma as well as generation of steam, known as Molten Fuel Coolant Interaction, were investigated in small-scale experiments reproducing key natural conditions (Wohletz 1983). The tests consist of injecting water in a crucible filled with a remelted volcanic rock or a synthetic melt whose composition is generally close to that of basaltic magmas (Fig. 31a). Fragmentation is caused by brittle failure at high cooling rate and it generates

angular to subrounded fine particles of typical size of ~20-200  $\mu\text{m}$ , which decreases as explosivity increases, and that are ejected at velocities of ~200-400 m/s (Wohletz 1983, Zimanowski et al. 1991, 1997). Zimanowski et al. (1991) found that only a fraction of the melt reacted explosively with water and that a maximum amount of water was vaporized at water/melt ratios of 1/6 to 1/25. In similar experiments but at subliquidus temperatures, Trigila et al. (1997) observed that magma vesicularity favored explosivity. Notice that recent experiments revealed that the intensity of magma-water interaction may be length-scale dependent (Sonder et al. 2018).

The formation of maar-diatreme structures (and kimberlite pipes) was investigated through different methods. Underground explosion experiments involving charges buried at depth of the order of ~1 m in holes filled with granular materials were carried out to investigate the excavation processes and the crater morphology. The results of these studies were generally discussed in terms of the normalized explosion depth

$$d_e^* = d_e/E^{1/3}, \quad (87)$$

expressed in  $\text{m/J}^{1/3}$ , with  $d_e$  the depth of the explosive charge and  $E$  the energy of the explosion. For a given explosion energy the optimal depth was defined as that resulting in the maximum crater diameter. With granular materials, a negligible amount of energy was consumed to fragment the host medium, unless it had some significant strength (Macorps et al. 2016), in contrast to natural cases that involve coherent rocks. Experiments showed that explosions generated jets whose height was set by the normalized depth and which also controlled the distribution of ejecta from shallow levels outside (Graettinger et al. 2014). Structural analysis of the craters morphology and subsurface structures revealed that the deposits consisted of materials from different depths (Fig. 31b; Ross et al. 2013, Graettinger et al. 2014, Valentine et al. 2012, 2015). Goto et al. (2001) observed that the crater diameter ( $D$ ) increased with explosion energy according to

$$\log D = 0.32 \log E - 2.06, \quad (88)$$

and Sato and Taniguchi (1997) found that the relationship between the diameter and the volume of ejecta ( $V$ ) was

$$D = 0.97 V^{0.36} \quad (89)$$

and that 0.7-10% of the initial thermal energy was converted into kinetic energy. Strong host materials favored higher crater rims as well as larger and deeper craters with steep walls (Macorps et al. 2016). Multiple explosions, typical of phreatomagmatic eruptions, created craters of about the same size as that of individual events of similar energy but that were narrower and deeper (Valentine et al. 2012). They caused progressive mixing of the crater-filling material (Graettinger et al. 2014) and weakened the host medium, suggesting that material strength was important only at early stages (Macorps et al. 2016). Explosions were also simulated by injecting compressed air or air-particle mixtures from a point source into a granular material. In a cohesionless host medium the injected material had the shape of a bubble that expanded upwards and created a cavity topped by a surface dome, and deposits in the depression were conical and flared upward (Ross et al. 2008a, 2008b, Andrews et al. 2014). Experiments with cohesive material, however, revealed that the strength of the host medium controlled the excavation processes and structures (Galland et al. 2014, Fig. 31c) and they also allowed investigating the grain size distribution of the fragments (Haug et al. 2013). Considering the following dimensionless numbers

$$\frac{P}{\rho gh}, \quad \frac{P}{C}, \quad (90)$$

with  $P$  the gas overpressure,  $\rho gh$  the lithostatic pressure, and  $C$  the material cohesion, Galland et al. (2014) showed that at high values (i.e. high energy in the system) vertical vents formed and deformation occurred through plastic yielding, whereas at low values (i.e. low energy) vents were inclined and formed through fracturing. Other experiments consisting of air injected at low rates, simulating fluidization processes at final stages in kimberlite pipes, revealed internal zones of mixed material and efficient grain size sorting relevant to some natural cases (Walters et al. 2006, Gernon et al. 2008).

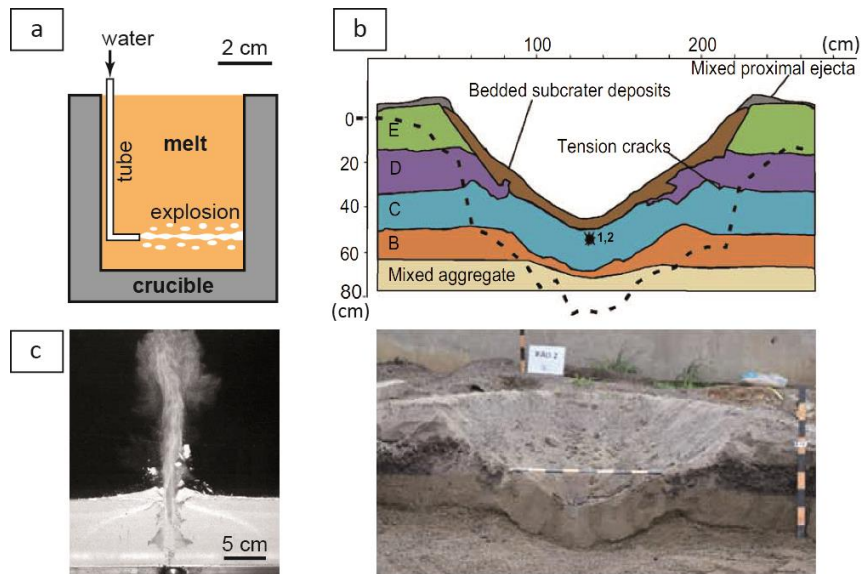


**Figure 31.** Experimental studies on phreatomagmatism. (a) Steam explosions by entrapment of water in a melt, from Zimanowski et al. (1991). (b) Analogue maar-diatreme caused by explosion of a charge in a cohesionless granular material, Graettinger et al. (2014). (c) Excavation caused by a pressurized air jet in a cohesive granular material, Galland et al. (2014).

Phreatic and hydrothermal events leading to fragmentation of water-saturated host rocks or to geyser eruptions were the focus of some recent studies. In rapid decompression shock-tube experiments (cf. section 3.3.2), Mayer et al. (2015) and Montanaro et al. (2016) showed that steam flashing released energy one order of magnitude higher than that from gas expansion and caused faster fragmentation of natural rock samples, finer grain sizes and higher ejection velocity, the latter increasing with porosity owing to higher potential energy. Geysers are common in volcanic settings and show a diversity of poorly understood eruptive styles, which were investigated using devices accounting for the possible complex natural configurations (Fig. 32). The setups consisted of a reservoir of cold water heated until it was vaporized, representing the deep hydrothermal system. The reservoir was connected to a conduit, and in some cases to more superficial reservoirs. In a simple configuration involving a straight vertical conduit, eruptions were often periodic and the expelled mass correlated with the repose time whereas the cumulative mass erupted increased linearly with time (Toramaru and Maeda 2013). Continuous discharge, however, was also observed depending on the balance between heat loss at conduit margins and heat supplied from hot reservoirs, and its rate was controlled by the length and radius of the conduit (Namiki et al. 2016). The process was complicated by the presence of shallow reservoirs that supplied cold water into the conduit, which inhibited boiling and hence controlled eruptions periodicity (Namiki et al. 2016). Experiments involving a complex conduit geometry revealed that a bubble trap favored vapor accumulation, heat transfer and hence boiling at shallow levels (Adelstein et al. 2014).

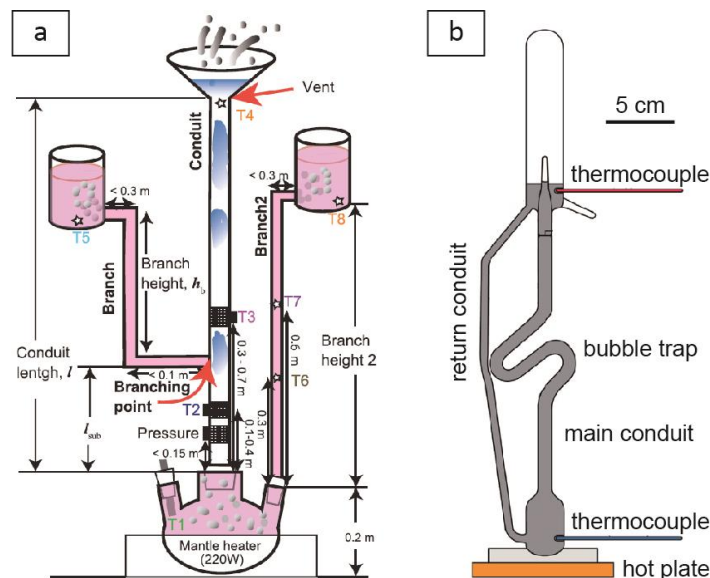


**Figure 32.** Experimental devices used to investigate geyser eruptions. (a) Conduit with connected reservoirs, Namiki et al. (2016). (c) Curved conduit with bubble trap, Adelstein et al. (2014).

### 3.7.3 Associated atmospheric phenomena

Electrical charging is known to occur during explosive eruptions and may cause spectacular events such as lightning. Its causes have been investigated in different experimental configurations in order to provide insights into eruptions mechanisms and to develop tools for monitoring. Büttner et al. (1997, 2000) compared the results of experiments simulating explosions caused by the MFCI process (see section 3.7.2.) or by release of a pressurized gas in a melt, which both involved a detector of charges and of electric field gradient. They concluded that fragmentation by magma/water interactions was the most efficient to generate electrical charging, and that the amplitude of the electric signals increased with the surface area of the fragments and hence with the intensity of the explosions. Other studies showed that charging could occur as well in conduits and in eruptive jets. James et al. (1998, 2000) investigated fracturing of pumices through collisions and they measured electrical charging, which increased with the impact velocity but varied little with ambient humidity. Rapid decompression experiments on volcanic jets (see section 3.3.1) involving natural or synthetic gas-particle mixtures revealed that relative movement of charged particles generated electric potential and lightning whose intensity increased with the amount of fine particles (Cimarelli et al. 2014, Fig. 33). They also helped estimating the total charge of the jet as well as the magnitude and number of jet-to-ground discharges (Gaudin and Cimarelli 2019). Other experiments showed that high-current electrical impulse altered the grain size distribution of fine ash samples, through melting, vesiculation and fragmentation of the particles, and also caused textures recognized in some natural fall deposits (Genareau et al. 2019).

Other atmospheric phenomena include airwaves generated in various contexts. Harmonic signals related to shallow conduit processes were studied by Lyons et al. (2013) and Ichihara et al. (2013). In their device a flow of compressed air controlled by an oscillating valve was injected into a viscoelastic analogue fluid through which harmonic signals similar to those recorded at some volcanoes were created. The signals were transmitted into the atmosphere and recorded by sensors, provided the fluid viscosity was sufficiently high and a stable open conduit could form, and they could be compared with natural data. In nature, airwaves are also generated by shallow underwater volcanic explosions. These were investigated by Ichihara et al. (2009) who conducted large-scale experiments in a lake or a natural pool, using explosive charges at depth of a few meters. The results revealed that the airwaves had characteristics controlled by the scaled depth (see equation 87) and their transmission from water to air depended on both the explosion source and on the behavior of the water above.

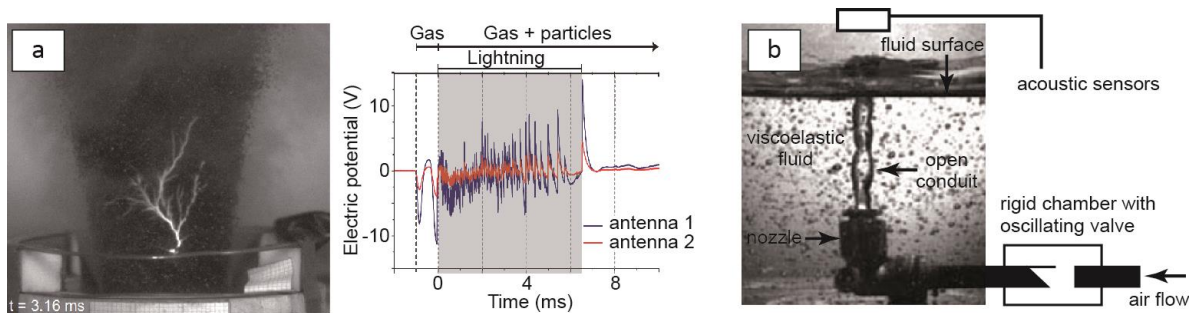


**Figure 33.** Experiments on atmospheric phenomena of volcanic origin. (a) Gas-particle jet with flashes (*left*) and associated electric potential recorded by antennas (*right*), modified from Cimarelli et al. (2014). (b) Experiment on gas flow in a stable open conduit in a fluid of high viscosity and generating airwaves, modified from Lyons et al. (2013).

#### 4. Summary and perspectives

This review shows that the experimental work devoted to the study of volcanic processes is becoming more and more sophisticated due to growing expertise and knowledge of the experimental procedures, materials, and measurement techniques. It appears that the choice of the materials (natural or analogue) may be based on technical constraints, but it is often part of a conceptual approach. Experimentalists use analogue materials mainly to broaden the range of parameter values and to explore physical regimes in more detail. Another important point is that there is a disparity in the quantitative treatment of the results according to the degree of knowledge of the physics of the natural system considered. In general, physical regimes can be accurately mapped using dimensionless numbers in works involving fluids (or highly dilute two-phase systems) or continuous solids whose fundamental laws are well known. Most of the studies presented above on magmatic chambers, magma intrusions, lava flows or domes, eruptive jets or plumes, and dilute PDCs illustrates this point well. In contrast, the physical regimes of systems in which particles have a crucial effect and whose basic principles are still poorly understood, such as granular flows (i.e. with negligible pore fluid pressure) or hyper-concentrated fluid-particle flows, are less well characterized. In this context, there is considerable scope for progress in understanding the mechanisms of dense PDCs and debris avalanches, and this will depend in particular on the continuous progress made by the granular physics community. This review highlights also the growing number of large-scale experiments, as illustrated by several studies on conduit flows, plumes, PDCs, lava flows, and phreatomagmatic eruptions. There are two main reasons for using the large scale: greater ease of direct observation and sensor measurements, and higher Reynolds numbers to reach dynamic similarity with the natural phenomena.

This review emphasizes criteria for evaluating the dynamic similarity between the natural and laboratory cases, which can be used to design an experiment. It is crucial, however, to consider some important experimental restrictions for all types of volcanic processes, including in particular initial and boundary conditions. For instance, many laboratory experiments on the dynamics of magma chambers impose initial static conditions that may influence processes in subsequent dynamic conditions; dam-break experiments are also commonly used to simulate PDCs and debris avalanches, but such a set-up does not strictly reproduce the onset of the natural phenomenon. Below is a non-exhaustive list of examples where methodological and/or conceptual bias can significantly affect the quality of studies. In experiments on magmas, the increase in viscosity as volatiles exsolve and the temperature-dependent rheology are rarely taken into account. For intrusions, it is necessary to find more appropriate materials with lower fracture strength and less ductile behavior at crack tip and also capable of simulating continuous mechanical heterogeneities; more experiments with continuous fluid injection are needed to study the kinematics and shape of intrusions in three dimensions. Scaling issues are rarely taken into account in experiments on vesiculation and magma fragmentation. However, the size and shape of particles can depend on the length scale of the apparatus (Kueppers et al., 2006b), which can be critical when comparing analog pyroclasts to natural samples. Various uncertainties remain regarding the study of turbulent biphasic mixtures. In general, the Reynolds number independence principle is used to treat turbulent flows but this assumption may not be always valid. This question may be crucial when

considering the possible dependence of fluid-particle interactions with the degree of turbulence (e.g., Weit et al., 2019). More specifically, the absence of particles in experiments simulating turbulent flows can be problematic as particles are known to affect the formation of eddies (Jessop and Jellinek 2014) while particle-particle interactions, which increase in areas with high particle concentrations, can control the dynamics of the mixture. Boundary conditions also play a critical role in designing laboratory experiments. Geometrical effects of a sloping boundary at the edge of an analog magma chamber can considerably affect compositional convection, tending to either homogenize or maintain a stable stratification in the experimental chamber (Turner and Campbell, 1986). For plume studies, the lateral propagation of the analog umbrella cloud may be inhibited by boundaries, which promote the formation of a return flow that can modify the cloud dynamics (Kotsonivos, 2000). Experiments should be conducted in large water reservoirs or in the ambient atmosphere to avoid this problem, but this strategy is challenging as it requires to adapt the measurement techniques. Studies on PDCs may also have significant limitations. Experiments on dilute PDCs should be performed with ambient air to ensure proper scaling and reliable study of air entrainment and heating as well as unsteady sedimentation (Andrews and Manga 2011, 2012). The study of dense granular flows in channel configuration should be considered with caution because lateral boundaries can have serious influence on flow dynamics (see Brodu et al. 2015); this is important in the context of unconfined flows such as most high volume PDCs and debris avalanches. In addition, the temporal dynamics of these flows are often difficult to reproduce in experiments under controlled conditions, making it important of complementing the experiments with numerical simulations.

Modeling is an ideal complement to laboratory experiments in many circumstances as it helps to interpret the experimental results and explore broader physical regimes under steady or unsteady conditions. In turn, results of experiments of phenomena not yet recognized define a conceptual framework that assists in the development of models, as shown for instance by the works on the dynamics of fire-fountain and strombolian eruptions triggered by foam destabilization at the top of a magma chamber (Jaupart and Vergnolle 1989). They also serve to validate and/or constrain the fundamental assumptions made for model development, and they can be used for benchmarking exercises. Examples include studies on magma chambers (Huppert and Sparks 1988a, Koyaguci et al. 1993), bubble number density and bubble growth in magmas (Toramaru 1996, 2006, Lensky et al. 2004), foam instability (Thomas et al. 1993), propagation of intrusions (Takada 1990, McLeod and Tait 1999), eruptive jets and plumes (Sparks et al. 1991, Mier-Torecilla et al. 2012), lava flows and domes (Huppert et al. 1982b, Cordonnier et al. 2016, Dietterich et al. 2017), lava dome growth (Balmforth et al. (2000), and dense PDCs with pore pressure (Gueugneau et al. 2017). Experimental results also help to constrain specific physical parameters. For example, Carazzo et al (2014) and Aubry et al (2017) used laboratory experiments on turbulent jets in a windy atmosphere to empirically constrain the wind entrainment coefficient in 1D models of volcanic plumes, while Aubry et al (2017) tested four entrainment models and concluded with a better recommendation by comparing their 1D model to laboratory data.

Many fundamental questions about eruptive processes remain (see National Academies 2017 for review). We present below some ideas for future experimental works that may have a strong potential:

- (1) Although it is increasingly well accepted that the structure of most magmatic chambers is a mush relatively shortly before an eruption, the processes of destabilizing the mush and mobilizing the interstitial liquid remain poorly understood and studies on magmatic mush are rare yet (see section 3.1.2). The experimental approach may provide a better understanding of the mechanisms that cause the separation of the liquid (magma) and solid (crystals) phases, which can lead to the activation of the magmatic system.
- (2) The fragmentation of magma (ductile or fragile) and the emplacement of PDC (dilute turbulent or granular concentrated flow) are examples of volcanic phenomena in which end-member mechanisms define a range of eruptive conditions. Further experimental studies should clarify the limits of the physical regimes and consequently should help to identify at which spatial and temporal scales the mechanisms can operate during an eruption.
- (3) Many aspects of the physics of gas-particle flows, which are ubiquitous in explosive volcanic eruptions at various solid concentrations, remain poorly understood. These include (i) the coupling between the fluid and solid phases and its consequences for the particle concentration and structure of the mixtures (e.g., Breard et al. 2016, Weit et al. 2019), and (ii) the interaction between these flows and

their surrounding environment such as a solid substrate, a water body or the atmosphere (e.g., Jessop and Jellinek 2014).

(4) Experimental work related to monitoring studies is likely to increase in the near future as it will help to better understand the relationship between observed signals and eruptive dynamics. Recent studies on the intensity of surface deformation caused by magma intrusions (Kavanagh et al. 2018), on flow-induced oscillations of vent dynamics (Kanno and Ichihara 2018), and on the link between acoustic emissions and magma/rock fracturing (Vasseur et al. 2018, Clarke et al. 2019), between radio frequency emissions and expansion of an overpressured jet (Méndez Harper et al. 2018) or between large earthquakes and volcanic unrest (Namiki et al. 2018) are examples of this emerging theme.

### Acknowledgements

Editor Joan Martí gave us the opportunity to provide this challenging but stimulating review to the scientific community. We warmly thank Mie Ichihara and Adelina Geyer for their thorough and constructive reviews, which greatly improved the manuscript. We thank Aldo Tamburrino (University of Chile) for useful discussions on dimensional analysis. This is ClerVolc contribution number XXX.

### Appendix – Dimensional analysis and dimensionless numbers

This appendix presents the fundamental principles of dimensional analysis and the methods commonly used to derive dimensionless numbers. It is important to keep in mind that dimensional analysis implies a simplified view of a natural phenomenon, and that dimensionless numbers are relevant only if the same physics applies at both laboratory and natural scale and if they have some physical meaning. Physical parameters have fundamental units, which are fundamental entities independent of each other. The fundamental units for length (meter), mass (kilogram), and time (second) are used to quantify most phenomena and can be combined to give derived units (e.g. meter per second for velocity). Other units such as those of temperature, light or electric intensity are more rarely used. If physical parameters have  $n$  fundamental units,  $u$ , then their derived units are given by

$$[u_d] = [u_1]^a [u_2]^b \dots [u_n]^m \quad (A1)$$

where  $[x]$  reads dimension of  $x$ . For instance, considering the dimensions of length L, mass M and time T, the dimension of velocity is denoted  $[U]=L^1M^0T^{-1}$ . Physical parameters are involved in equations that describe the phenomena and must be dimensionally homogeneous. A simple case is the equation of the motion of an object in free fall in which all the terms have the dimension of length,

$$x = x_0 + vt + \frac{1}{2}gt^2 \quad , \quad (A2)$$

and assuming  $x_0=0$  it can be expressed as

$$f(x, vt, gt^2) = 0. \quad (A3)$$

It is possible to make this equation dimensionless and to reduce the number of parameters by dividing each term of equation A2 by  $vt$ , which has the same dimension of  $x$ , so that

$$\frac{x}{vt} = 1 + \frac{1}{2} \frac{gt}{v} \quad , \quad (A4)$$

which can be expressed as

$$\varphi\left(\frac{x}{vt}, \frac{gt}{v}\right) = 0. \quad (A5)$$

This simple example illustrates the notion of dimensionless number, which is the base of dimensional analysis. Dimensionless numbers can be obtained using three methods, depending on the degree of knowledge on the physics of the system addressed, which are presented below.

The first method is the so-called matrix of dimensions, which is used when the fundamental physics of a phenomenon is poorly known and it is particularly relevant for exploratory experiments. It relies on the Vaschy-Buckingham theorem (Vaschy 1892, Buckingham 1914), based on earlier work of Bertrand (1878), which states that if a phenomenon is described by  $m$  variables involving  $n$  fundamental units, then  $m-n$  dimensionless numbers may be considered. In other words, if a variable  $a_1$  depends on  $m-1$  variables through

$$f(a_1, a_2, \dots, a_m) = 0 \quad (A6)$$

where  $[a_i] = [u_1]^a [u_2]^b \dots [u_n]^n$  and  $i=1,2,\dots,m$ , with at least one non-zero exponent, then the phenomenon can be expressed as

$$\varphi(\pi_1, \pi_2, \dots, \pi_{m-n}) = 0. \quad (A7)$$

This method has pros and cons. It is convenient for addressing complex problems as it requires little initial information on the physics. However, though  $m-n$  dimensionless numbers instead of  $m$  variables may be considered, the function  $\varphi$  is unknown. The dimensionless numbers are obtained in three steps in which inadequate choices will result in possible errors. The first step consists of choosing the relevant variables, and any mistake in the choice of the  $m$  variables will result in an incorrect analysis. The second step is the construction of the matrix of dimension, which consists of assigning appropriate exponents to the fundamental units of each variable. For instance, density is expressed as  $[\rho]=M^1L^{-3}T^0$ , and the exponents are reported in a table with the fundamental units in the first column and all variables in the first row. In the third step, a so-called *base* of three variables (having together the three fundamental units) is chosen arbitrarily and associated with the variables remaining to obtain dimensionless numbers (note that here also inadequate choice of the base is a possible source of error). For instance, a base consisting of  $[g]=M^0L^1T^{-2}$ ,  $[h]=M^0L^1T^0$ , and  $[\rho]=M^1L^{-3}T^0$ , is combined with velocity  $[U]=M^0L^1T^{-1}$ . A first dimensionless number,  $N$ , is obtained from

$$[N] = [M^0L^1T^{-1}] [M^0L^1T^{-2}]^a [M^0L^1T^0]^b [M^1L^{-3}T^0]^c \quad (A8)$$

and considering the exponents for each fundamental units, i.e.  $c=0$  for  $[M]$ ,  $1+a+b-3c=0$  for  $[L]$ , and  $-1-2a=0$  for  $[T]$ . Solving the system of equations gives  $a=-1/2$  and  $b=-1/2$ , so that  $N=U/(gh)^{1/2}$  (note that  $N$  is a Froude number).

The second method to obtain dimensionless numbers may be used when some fundamental physics of the system addressed is known and dimensionless ratios of given physical parameters can be readily defined. This procedure was employed by Iverson (1997) who considered frictional and collisional interparticle stresses, inertial and viscous fluid stresses, and viscous solid-fluid stresses at micro-scale in gravitational fluid-particle flows. For instance, the ratio of solid collisional stresses,  $\varepsilon_s \rho_s \gamma^2 d^2$ , over fluid viscous stresses,  $\varepsilon_f \gamma \mu$ , with  $\varepsilon_s$  and  $\rho_s$  the solid volume fraction and density,  $\gamma$  the shear rate,  $d$  the particle size,  $\varepsilon_f$  and  $\mu$  the fluid volume fraction and dynamic viscosity, is  $\varepsilon_s \rho_s \gamma d^2 / \varepsilon_f \mu$  and is similar to the Bagnold number.

Finally, dimensionless numbers can be obtained using a third method when fundamental equations of a physical system are known. Let's consider the Navier-Stokes equation that describes a fluid flow (for the  $x$  direction component),

$$u \frac{\partial u}{\partial x} + v \frac{\partial u}{\partial y} = -\frac{1}{\rho} \frac{\partial P}{\partial x} + g_x + \frac{\mu}{\rho} \left( \frac{\partial^2 u}{\partial x^2} + \frac{\partial^2 u}{\partial y^2} \right) \quad (A9)$$

with  $u$  and  $v$  the velocity components in directions  $x$  and  $y$ ,  $\rho$  and  $\mu$  the fluid density and viscosity,  $P$  the pressure, and  $g$  the gravity acceleration. Typical length ( $L$ ) and velocity ( $U$ ) scales may be defined to give dimensionless lengths,  $x^*=x/L$  and  $y^*=y/L$ , and velocities,  $u^*=u/U$  and  $v^*=v/U$ , which are included in equation A9 to give

$$u^* \frac{U^2}{L} \frac{\partial u^*}{\partial x^*} + v^* \frac{U^2}{L} \frac{\partial u^*}{\partial y^*} = -\frac{1}{\rho L} \frac{\partial P}{\partial x^*} + g_x + \frac{\mu}{\rho L^2} \left( \frac{\partial^2 u^*}{\partial x^{*2}} + \frac{\partial^2 u^*}{\partial y^{*2}} \right). \quad (A10)$$

Dividing each term by  $U^2/L$ , and stating  $P^*=P/(\rho U^2)$  and  $g_x=-g \sin \alpha$ , gives

$$u^* \frac{\partial u^*}{\partial x^*} + v^* \frac{\partial u^*}{\partial y^*} = -\frac{\partial P^*}{\partial x^*} - \frac{gL}{U^2} \sin \alpha + \frac{\mu}{\rho UL} \left( \frac{\partial^2 u^*}{\partial x^{*2}} + \frac{\partial^2 u^*}{\partial y^{*2}} \right). \quad (A11)$$

This example demonstrates that the Froude,  $U/(gL)^{1/2}$ , and the Reynolds,  $\rho UL/\mu$ , numbers are relevant for the specific case addressed and also shows how fundamental equations can be made dimensionless.

## References

- Acocella, V., 2007. Understanding caldera structure and development: An overview of analogue models compared to natural calderas. *Earth Sci. Rev.*, 85: 125-160, doi:10.1016/j.earscirev.2007.08.004.
- Adelstein, E., Tran, A., Muñoz Saez, C., Shteinberg, A. and Manga, M., 2014. Geysir preplay and eruption in a laboratory model with a bubble trap. *J. Volcanol. Geotherm. Res.* 285: 129-135, doi: <http://dx.doi.org/10.1016/j.jvolgeores.2014.08.005>.
- Alatorre-Ibargüenotia, M., Scheu, B., Dingwell, D.B., Delgado-Granados, H., Taddeucci, J., 2010. Energy consumption by magmatic fragmentation and pyroclast ejection during Vulcanian eruptions. *Earth Planet. Sci. Lett.* 291: 60-69, doi: 10.1016/j.epsl.2009.12.051.
- Alidibirov, M., Dingwell, D.B., 1996. Magma fragmentation by rapid decompression. *Nature*, 380: 146-148.
- Andrews, B., Manga, M., 2011. Effects of topography on pyroclastic density current runout and formation of coignimbrites. *Geology*, 39(12): 1099-1103, doi: 10.1130/G32226.1.
- Andrews, B., Manga, M., 2012. Experimental study of turbulence, sedimentation, and coignimbrite mass partitioning in dilute pyroclastic density currents. *J. Volcanol. Geotherm. Res.* 225-226: 30-44, doi: 10.1016/j.jvolgeores.2012.02.011.
- Andrews, B., 2014. Dispersal and air entrainment in unconfined dilute pyroclastic density currents. *Bull. Volcanol.* 76: 852- , doi: 10.1007/s00445-014-0852-4.
- Andrews, R.G., White, J.D.L., Dürig, T., Zimanowski, B., 2014. Discrete blasts in granular material yield two-stage process of cavitation and granular fountaining. *Geophys. Res. Lett.*, 41: 422–428, doi: 10.1002/2013GL058526.
- Anilkumar, A.V., Sparks, R.S.J., Sturtevant, B., 1993. Geological implications and applications of high-velocity two-phase flow experiments. *J. Volcanol. Geotherm. Res.* 56: 145-160.
- Annen, C., Blundy, J.D., Leuthold, J., Sparks, R.S.J., 2015. Construction and evolution of igneous bodies: Towards an integrated perspective of crustal magmatism. *Lithos* 230: 206-221.
- Applegarth, L.J., James, M.R., van Wyk de Vries, B., Pinkerton, H., 2010. Influence of surface clinker on the crustal structures and dynamics of 'a'a lava flows. *J. Geophys. Res.* 115, B07210, doi: 10.1029/JB006965.
- Aubry, T.J., Carazzo, G. and Jellinek, A.M., 2017. Turbulent entrainment into volcanic plumes: new constraints from laboratory experiments on buoyant jets rising in a stratified crossflow. *Geophys. Res. Lett.* 44: 10,198-10,207, <https://doi.org/10.1002/2017GL075069>.
- Bagdassarov, N.S., Dingwell, D.B., 1992. A rheological investigation of vesicular rhyolite. *J. Volcanol. Geotherm. Res.* 50: 307-322.
- Bagdassarov, N.S., Pinkerton, H., 2004. Transient phenomena in vesicular lava flows based on laboratory experiments with analogue materials. *J. Volcanol. Geotherm. Res.* 132, 115-136.
- Bagnold, R.A., 1954. Experiments on a gravity-free dispersion of large solid spheres in a Newtonian fluid under shear. *Proceedings of the Royal Society, London A*, 225: 49-63.
- Balmforth, N.J., Burbidge, A.S., Craster, R.V., Salzig, J., Shen, A., 2000. Visco-plastic models of isothermal lava domes. *J. Fluid Mech.* 403, 37-65.
- Bareschino, P., Lirer, L., Marzocchella, A., Petrosino, P., Salatino, P., 2008. Self-fluidization of subaerial rapid granular flows. *Powder Technol.* 182: 323-333, doi: doi:10.1016/j.powtec.2007.12.010.
- Batchelor, G.K., 1953. The conditions for dynamical similarity of motions of a frictionless perfect-gas atmosphere. *Quart. J. Roy. Met. Soc.* 79, 224-235.
- Benjamin, T.B., 1968. Gravity currents and related phenomena. *J. Fluid Mech.* 31: 209-248.
- Bertrand, J., 1878. Sur l'homogénéité dans les formules de physique. *Comptes Rendus* 86: 916-920.
- Blake, S., Bruno, B.C., 2000. Modeling the emplacement of compound lava flows. *Earth Planet. Sci. Lett.* 184: 181-197.
- Breard, E.C.P., Lube, G., Jones, J.R., Dufek, J., Cronin, S.J., Valentine, G.A., Moebis, A., 2016. Coupling of turbulent and non-turbulent flow regimes within pyroclastic density currents. *Nat. Geosci.* 9: 767-771, doi: 10.1038/NGEO2794.
- Breard, E.C.P., Dufek, J., Lube, G., 2018. Enhanced mobility in concentrated pyroclastic density currents: An examination of a self-fluidization mechanism. *Geophys. Res. Lett.* 45: 654–664, doi: 10.1002/2017GL075759.
- Breard, E.C.P., Jones, J., Fullard, L., Lube, G., Davies, C., Dufek, J., 2019. The permeability of volcanic mixtures - Implications for pyroclastic currents. *J. Geophys. Res.: Solid Earth*, 124: 1343–1360. <https://doi.org/10.1029/2018JB016544>.
- Breard, E.C.P., Lube, G., 2017. Inside pyroclastic density currents – uncovering the enigmatic flow structure and transport behaviour in large-scale experiments. *Earth Planet. Sci. Lett.* 458: 22–36.
- Brennen, C.E., 1995. Cavitation and bubble dynamics. Oxford Engineering Science series 44, Oxford University Press.
- Brodu, N., Delannay, R., Valance, A., Richard, P., 2015. New patterns in high speed granular flows. *J. Fluid Mech.* 769, 218-228, doi:10.1017/jfm.2015.10.
- Brown, M.C., 1962. Discussion, Nuées ardentes and fluidization. *Am. J. Sci.* 260: 467-470.
- Buckingham, E., 1914. On physically similar systems. Illustrations of the use of dimensional equations. *Phys. Rev.* 4: 345-376.
- Buisson, C., Merle, O., 2002. Experiments on internal strain in lava dome cross sections. *Bull. Volcanol.* 64: 363-371.
- Burgisser, A. and Bergantz, G.W., 2002. Reconciling pyroclastic flow and surge: the multiphase physics of pyroclastic density currents. *Earth Planet. Sci. Lett.* 202: 405-418.
- Burgisser, A., Bergantz, G.W., Breidenthal, R.E., 2005. Addressing the complexity in laboratory experiments: the scaling of dilute multiphase flows in magmatic systems. *J. Volcanol. Geotherm. Res.* 141: 245-265.
- Bursik, M.I., Woods, A.W., 2000. The effect of topography on sedimentation from particle-laden turbulent density currents. *J. Sed. Res.*, 70(1): 53-63.
- Büttner, R., Röder, H., Zimanowski, B., 1997. Electrical effects generated by experimental volcanic explosions. *Appl. Phys. Lett.* 70(14): 1903-1905.
- Büttner, R., Zimanowski, B., Röder, H., 2000. Short-time electrical effects during volcanic eruption: Experiments and field measurements. *J. Geophys. Res.* 105(B2): 2819-2827.

- Cagnoli, B., Barmin, A., Melnik, O., Sparks, R.S.J., 2002. Depressurization of fine powders in a shock tube and dynamics of fragmented magma in volcanic conduits. *Earth Planet. Sci. Lett.* 204: 101-113.
- Cagnoli, B., Manga, M., 2003. Pumice-pumice collisions and the effect of the impact angle. *Geophys. Res. Lett.* 30(12): 1636, doi: 10.1029/2003GL017421.
- Cagnoli, B., Manga, M., 2004. Granular mass flows and Coulomb's friction in shear cell experiments: implications for geophysical flows. *J. Geophys. Res.* 109: F04005, doi: 10.1029/2004JF000177.
- Cagnoli, B., Romano, G.P., 2010. Effect of grain size on mobility of dry granular flows of angular rock fragments: an experimental determination. *J. Volcanol. Geotherm. Res.* 193: 18-24, doi: 10.1016/j.jvolgeores.2010.03.003.
- Cagnoli, B., Romano, G.P., 2012. Effects of flow volume and grain size on mobility of dry granular flows of angular fragments: A functional relationship of scaling parameters. *J. Geophys. Res.* 117: B02207, doi: 10.1029/2011JB008926.
- Campbell, I.H., Turner, J.S., 1987. A laboratory investigation of assimilation at the top of a basaltic magma chamber. *J. Geology* 95: 155-172.
- Canon-Tapia, E., Pinkerton, H., 2000. The anisotropy of magnetic susceptibility of lava flows: an experimental approach. *J. Volcanol. Geotherm. Res.* 98, 219-233.
- Capponi, A., Lane, S.J., James, M.R., 2017. The implications of gas slug ascent in a stratified magma for acoustic and ground deformation source mechanisms in Strombolian eruptions. *Earth Planet. Sci. Lett.* 468: 101-111, <http://dx.doi.org/10.1016/j.epsl.2017.04.008>.
- Carazzo, G., Jellinek, A.M., 2012. A new view of the dynamics, stability and longevity of volcanic clouds. *Earth Planet. Sci. Lett.* 325-326, 39-51, doi:10.1016/j.epsl.2012.01.025.
- Carazzo, G., Jellinek, A.M., 2013. Particle sedimentation and diffusive convection in volcanic ash-clouds. *J. Geophys. Res.* 118, 1420-1437, doi:10.1002/jgrb.50155.
- Carazzo, G., Girault, F., Aubry, T., Bouquerel, H., Kaminski, E., 2014. Laboratory experiments of forced plumes in a density-stratified crossflow and implications for volcanic plumes. *Geophys. Res. Lett.* 41, 8759-8766, doi: 10.1002/GL2014GL061887.
- Carazzo, G., Kaminski, E., Tait, S., 2015. The timing and intensity of column collapse during explosive volcanic eruptions. *Earth Planet. Sci. Lett.* 411, 208-217, doi:10.1016/j.epsl.2014.12.006.
- Cardoso, S.S.S., Zarrebini, M., 2001a. Convection driven by particle settling surrounding a turbulent plume. *Chem. Eng. Sci.* 56, 3365-3375.
- Cardoso, S.S.S., Zarrebini, M., 2001b. Sedimentation of polydispersed particles from a turbulent plume. *Chem. Eng. Sci.* 56, 4725-4736.
- Carey, S.N., Sigurdsson, H., Sparks, R.S.J., 1988. Experimental studies of particle-laden plumes. *J. Geophys. Res.* 93, B12, 15,314-15,328.
- Caricchi, L., Pommier, A., Pistone, M., Castro, J., Burgisser, A., Perugini, D., 2011. Strain-induced magma degassing: insights from simple-shear experiments on bubble bearing melts. *Bull. Volcanol.* 73: 1245-1257, doi: 10.1007/s00445-011-0471-2.
- Cashman, K.V., Kerr, R.C., Griffiths, R.W., 2006. A laboratory model of surface crust formation and disruption on lava flows through non-uniform channels. *Bull. Volcanol.* 68, 753-770.
- Cashman, K.V., Scheu, B., 2015. Magmatic fragmentation. In: H. Sigurdson et al. (Editor), *Encyclopedia of volcanoes*, second edition. Academic Press, pp. 459-472.
- Castruccio, A., Rust, A.C., Sparks, R.S.J., 2010. Rheology and flow of crystal-bearing lavas: insights from analogue gravity currents. *Earth Planet. Sci. Lett.* 297, 471-480.
- Castruccio, A., Rust, A.C., Sparks, R.S.J., 2014. Assessing lava flow evolution from post-eruption data using Herschel-Bulkley rheology. *J. Volcanol. Geotherm. Res.* 275, 71-84.
- Chanceaux, L., Menand, T., 2014. Solidification effects on sill formation: An experimental approach. *Earth Planet. Sci. Lett.* 403: 79-88, <http://dx.doi.org/10.1016/j.epsl.2014.06.018>.
- Chanceaux, L., Menand, T., 2016. The effects of solidification on sill propagation dynamics and morphology. *Earth Planet. Sci. Lett.* 442: 39-50.
- Chédeville, C., Roche, O., 2014. Autofluidization of pyroclastic flows propagating on rough substrates as shown by laboratory experiments. *J. Geophys. Res.* 119: 1764-1776, doi: 10.1002/2013JB010554
- Chojnicki, K., Clarke, A.B., Phillips, J.C., 2006. A shock-tube investigation of the dynamics of gas-particle mixtures: Implications for explosive volcanic eruptions. *Geophys. Res. Lett.* 33, L15309.
- Chojnicki, K.N., Clarke, A.B., Adrian, R.J., Phillips, J.C., 2014. The flow structure of jets from transient sources and implications for modeling short-duration explosive volcanic eruptions. *Geochem. Geophys. Geosyst.* 15, 4831-4845.
- Chojnicki, K.N., Clarke, A.B., Phillips, J.C., Adrian, R.J., 2015. Rise dynamics of unsteady laboratory jets with implications for volcanic plumes. *Earth Planet. Sci. Lett.* 412, 186-196.
- Choux, C., Druitt, T.H. and Thomas, N., 2004. Stratification and particle segregation in flowing polydisperse suspensions, with applications to the transport and sedimentation of pyroclastic density currents. *J. Volcanol. Geotherm. Res.* 138: 223-241.
- Choux, C.M. and Druitt, T.H., 2002. Analogue study of particle segregation in pyroclastic density currents, with implications for the emplacement mechanisms of large ignimbrites. *Sedimentology*, 49: 907-928.
- Cigala, V., Kueppers, U., Peña Fernandez, J.J., Taddeucci, J., Sesterhenn, J., Dingwell, D.B., 2017. The dynamics of volcanic jets: Temporal evolution of particles exit velocity from shock-tube experiments. *J. Geophys. Res.* 122: 6031-6045, doi: 10.1002/2017JB014149.
- Cimarelli, C., Costa, A., Mueller, S., Mader, H.M., 2011. Rheology of magmas with bimodal crystal size and shape distributions: Insights from analog experiments. *Geochemistry, Geophysics, Geosystems* 12(7), Q07024, doi: 10.1029/2011GC003606.
- Cimarelli, C., Alatorre-Ibargüengoitia, M.A., Kueppers, U., Scheu, B., Dingwell, D.B., 2014. Experimental generation of volcanic lightning. *Geology*, 42(1): 79-82, doi:10.1130/G34802.1.

- Clarke, A.B., Phillips, J.C., Chojnicki, K.N., 2009. An investigation of Vulcanian eruption dynamics using laboratory analogue experiments and scaling analysis. In: Thordarson, T., Self, S., Larsen, G., Rowland, S.K., Hoskuldsson, A. (Eds.), *Studies in Volcanology: the Legacy of George Walker*. In: *Spec. Publ. IAVCEI*, vol. 2. Geological Society, London, pp. 155-166.
- Clarke, J., Adam, L., Sarout, J., van Wijk, K., Kennedy, B., Dautriat, J., 2019. The relation between viscosity and acoustic emissions as a laboratory analogue for volcano seismicity. *Geology*, 47(6): 499-503, <https://doi.org/10.1130/G45446.1>.
- Clift, R., Grace, J.R., Weber, M.E., 1978. *Bubbles, drops, and particles*. Academic Press, New-York, p. 792.
- Cordonnier, B., Caricchi, L., Pistone, M., Castro, J., Hess, K.-U., Gottschaller, S., Manga, M., Dingwell, D.B., 2012. The viscous-brittle transition of crystal-bearing silicic melt: Direct observation of magma rupture and healing. *Geology* 40(7): 611-614.
- Cordonnier, B., Lev, E., Garel, F., 2016. Benchmarking lava-flow models. *Geol. Soc. London Spec. Publ.* 426(1), 425-445.
- Dade, W.B., Huppert, H.H., 1995. Runout and fine-sediment deposits of axisymmetric turbidity currents. *J. Geophys. Res.* 100(C9): 18597-18609.
- Daniels, K.A., Menand, T., 2015. An experimental investigation of dyke injection under regional extensional stress. *J. Geophys. Res.* 120: 2014–2035, doi: 10.1002/2014JB011627.
- Del Bello, A., Lane, S.J., James, M.R., Llewellyn, E.W., Taddeucci, J., Scarlato, Capponi, A., 2015. Viscous plugging can enhance and modulate explosivity of strombolian eruptions. *Earth Planet. Sci. Lett.* 423: 210–218, <http://dx.doi.org/10.1016/j.epsl.2015.04.034>.
- Del Bello, E., Taddeucci, J., Scarlato, E., Cesaroni, C., 2015. Experimental investigation of the aggregation-disaggregation of colliding volcanic ash particles in turbulent, low-humidity suspensions. *Geophys. Res. Lett.* 42, 1068-1075.
- Del Bello, E., Taddeucci, J., de' Michieli Vitturi, M., Scarlato, P., Andronico, D., Scollo, S., Kueppers, U., Ricci, T., 2017. Effect of particle volume fraction on the settling velocity of volcanic ash particles: insights from joint experimental and numerical simulations. *Scientific reports* 7, 39620.
- Dellino, P., Büttner, R., Dioguardi, F., Doronzo, D.M., La Volpe, L., Mele, D., Sonder, I., Sulpizio, R., Zimanowski, B., 2010. Experimental evidence links volcanic particle characteristics to pyroclastic flow hazard. *Earth Planet. Sci. Lett.*, 295: 314-320, doi: 10.1016/j.epsl.2010.04.022.
- Dellino, P., Dioguardi, F., Zimanowski, B., Büttner, R., Mele, D., La Volpe, L., Sulpizio, R., Doronzo, D.M., Sonder, I., Bonasia, R., Calvari, S., Marotta, E., 2010. Conduit flow experiments help constraining the regime of explosive eruptions. *J. Geophys. Res.* 115: B04204, doi: 10.1029/2009JB006781.
- Dellino, P., Zimanowski, B., Büttner, R., La Volpe, L., Mele, D., Sulpizio, R., 2007. Large-scale experiments on the mechanics of pyroclastic flows: design, engineering, and first results. *J. Geophys. Res.* 112(B04202).
- Dellino, P., Dioguardi, F., Mele, D., D'Addabbo, M., Zimanowski, B., Büttner, R., Doronzo, D.M., Sonder, I., Sulpizio, R., Dürig, T., La Volpe, L., 2014. Volcanic jets, plumes, and collapsing fountains: evidence from large-scale experiment, with particular emphasis on the entrainment rate. *Bull. Volcanol.* 76, 834-852.
- Dietterich, H.R., Cashman, K.V., Rust A.C., Lev, E., 2015. Diverting lava flow in the lab. *Nature geoscience* 8, 494-496.
- Doronzo, D.M., Dellino, P., 2011. Interaction between pyroclastic density currents and buildings: Numerical simulation and first experiments. *Earth Planet. Sci. Lett.* 310: 286-292, doi: 10.1016/j.epsl.2011.08.017.
- Douillet, G.A., Rasmussen, K.R., Kueppers, U., Lo Castro, D., Merrisson, J.P., Iversen, J.J., Dingwell, D.B., 2014. Saltation threshold for pyroclasts at various bedslopes: Wind tunnel measurements. *J. Volcanol. Geotherm. Res.* 278–279 (2014) 14–24, 278-279: 14-24, <http://dx.doi.org/10.1016/j.jvolgeores.2014.03.011>.
- Druitt, T.H., Avard, G., Bruni, G., Lettieri, P., Maez, F., 2007. Gas retention in fine-grained pyroclastic flow materials at high temperatures. *Bull. Volcanol.* 69: 881-901.
- Dufek, J., 2016. The fluid mechanics of pyroclastic density currents. *Ann. Rev. Fluid Mech.* 48: 459-485, doi: 10.1146/annurev-fluid-122414-034252.
- Dufek, J., Manga, M., 2008. In situ production of ash in pyroclastic flows. *J. Geophys. Res.* 113: B09207, doi: 10.1029/2007JB005555.
- Dufek, J., Manga, M., Patel, A., 2012. Granular disruption during explosive volcanic eruptions. *Nat. Geosci.* 5: 561-564, doi: 10.1038/NGEO1524.
- Dufek, J., Manga, M., Staeder, M., 2007. Littoral blasts: Pumice-water heat transfer and the conditions for steam explosions when pyroclastic flows enter the ocean. *J. Geophys. Res.* 112: B11201, doi: 10.1029/2006JB004910.
- Dufek, J., Wexler, J., Manga, M., 2009. Transport capacity of pyroclastic density currents: Experiments and models of substrate-flow interaction. *J. Geophys. Res.* 114: B11203, doi: 10.1029/2008JB006216.
- Dufresne, A., 2012. Granular flow experiments on the interaction with stationary runout path materials and comparison to rock avalanche events. *Earth Surf. Process. Landforms* 37: 1527–1541, doi: 10.1002/esp.3296.
- Dufresne, A. and Davies, T.R., 2009. Longitudinal ridges in mass movement deposits. *Geomorphology*, 105: 171-181, doi: 10.1016/j.geomorph.2008.09.009.
- Dürig, T., Zimanowski, B., 2012. "Breaking news" on the formation of volcanic ash: Fraction dynamics in silicate glass. *Earth Planet. Sci. Lett.* 335-336: 1-8, doi: 10.1016/j.epsl.2012.05.001.
- Edwards, B.R., Karson, J., Wysocki, R., Lev, E., Bindeman, I., Kueppers, U., 2013. Insights on lava-ice/snow interactions from large-scale basaltic melt experiments. *Geology* 41 (8), 851-854.
- Elghobashi, S., 1994. On predicting particle-laden turbulent flows. *App. Scientif. Res.* 52, 309-329.
- Ernst, G.G.J., Davis, J.P., Sparks, R.S.J., 1994. Bifurcation of volcanic plumes in a crosswind. *Bull. Volcanol.* 56, 159-169.
- Ernst, G.G.J., Sparks, R.S.J., Carey, S.N., Bursik M.I., 1996. Sedimentation from turbulent jets and plumes. *J. Geophys. Res.* 101, B3, 5575-5589.
- Estep, J., Dufek, J., 2012. Substrate effects from force chain dynamics in dense granular flows. *J. Geophys. Res.* 117: F01028, doi: 10.1029/2011JF002125.
- Estep, J., Dufek, J., 2013. Multiphase flow dynamics of pyroclastic density currents during the May 18, 1980 lateral blast of Mount St. Helens. *J. Volcanol. Geotherm. Res.* 254: 108–117, doi 10.1016/j.jvolgeores.2012.12.023.

- Félix, G., Thomas, N., 2004. Relation between dry granular flow regimes and morphology of deposits: formation of levées in pyroclastic deposits. *Earth Planet. Sci. Lett.* 221: 197-213.
- Fink, J.H., Griffiths, R.W., 1990. Radial spreading of viscous-gravity currents with solidifying crust. *J. Fluid Mech.* 221, 485-509.
- Fink, J.H., Griffiths, R.W., 1992. A laboratory analog study of the surface morphology of lava flows extruded from point and line source. *J. Volcanol. Geotherm. Res.* 54, 19-32.
- Fink, J.H., Griffiths, R.W., 1998. Morphology, eruption rates, and rheology of lava domes: Insights from laboratory models. *J. Geophys. Res.* 103 (B1), 527-545.
- Fiske, R.S., Jackson, E.D., 1972. Orientation and growth of hawaiian volcanic rifts: the effect of regional structure and gravitational stresses. *Proc. Roy. Soc. London A*, 329(1578): 299-326.
- Fowler, A.C., Scheu, B., Lee, W.T., McGuinness, M.J., 2010. A theoretical model of the explosive fragmentation of vesicular magma. *Proc. Roy. Soc. London A*, 466: 731-752, doi:10.1098/rspa.2009.0382.
- Freundt, A., 1998. The formation of high grade ignimbrites, I: Experiments on high- and low concentration transport system containing sticky particles. *Bull. Volcanol.* 59: 414-435.
- Freundt, A., 2003. Entrance of pyroclastic flows into the sea: experimental observation. *Bull. Volcanol.* 65: 144-164.
- Galland, O., Cobbold, P.R., Hallot, E., de Bremond d'Ars, J., Delavaud, G., 2006. Use of vegetable oil and silica powder for scale modelling of magmatic intrusion in a deforming brittle crust. *Earth Planet. Sci. Lett.* 243: 786-804, doi:10.1016/j.epsl.2006.01.014.
- Galland, O., Gislér, G.R., Haug, Ø.T., 2014. Morphology and dynamics of explosive vents through cohesive rock formations. *J. Geophys. Res.* 119: doi: 10.1002/2014JB011050.
- Galland, O., Holohan, E., van Wyk de Vries, B., Burchardt, S., 2015. Laboratory modelling of volcano plumbing systems: a review. *Advances in volcanology*: doi: 10.1007/11157\_2015\_9.
- Gardner, J.E., Hilton, M., Carroll, M.R., 1999. Experimental constraints on degassing of magma: isothermal bubble growth during continuous decompression from high pressure. *Earth Planet. Sci. Lett.* 168: 201-218.
- Garel, F., Kaminski, E., Tait, S., Limare, A., 2012. An experimental study of the surface thermal signature of hot subaerial isoviscous gravity currents; Implications for thermal monitoring of lava flows and domes. *J. Geophys. Res.* 117, B02205, doi: 10.1029/2011JB008698.
- Garel, F., Kaminski, E., Tait, S., Limare, A., 2013. The influence of wind on the estimation of lava effusion rate from thermal remote-sensing. *J. Volcanol. Geotherm. Res.* 264, 223-230.
- Garel, F., Kaminski, E., Tait, S., Limare, A., 2014. An analogue study of the influence of solidification on the advance and surface thermal signature of lava flows. *Earth Planet. Sci. Lett.* 396, 46-55.
- Garel, F., Kaminski, E., Tait, S., Limare, A., 2016. A fluid dynamics perspective on the interpretation of the thermal signal of lava flows. *Geol. Soc. Lond. Spec. Publ.* 426(1), 243-256.
- Gaudin, D., Cimarelli, C., 2019. The electrification of volcanic jets and controlling parameters: A laboratory study. *Earth Planet. Sci. Lett.* 513: 69-80, <https://doi.org/10.1016/j.epsl.2019.02.024>.
- Genareau, K., Wallace, K.L., Gharghabi, P., Gafford, J., 2019. Lightning effects on the grain size distribution of volcanic ash. *Geophys. Res. Lett.* 46: 3133–3141. <https://doi.org/10.1029/2018GL081298>.
- Gernon, T.M., Gilbertson, M.A., Sparks, R.S.J., Field, M., 2008. Gas-fluidisation in an experimental tapered bed: Insights into processes in diverging volcanic conduits. *J. Volcanol. Geotherm. Res.* 174: 49-56, doi:10.1016/j.jvolgeores.2007.12.034.
- Geyer, A., Martí, J., 2014. A short review of our current understanding of the development of ring faults during collapse caldera formation. *Frontiers in Earth Sciences*, 2: 22. doi:10.3389/feart.2014.00022.
- Gilbert, J.S., Lane, S.J., 1994. The origin of accretionary lapilli. *Bull. Volcanol.* 56, 398-411.
- Girard, G., Stix, J., 2009. Buoyant replenishment in silicic magma reservoirs: Experimental approach and implications for magma dynamics, crystal mush remobilization, and eruption. *J. Geophys. Res.* 114, B08203, doi: 10.1029/2008JB005791.
- Girolami, L., Druit, T.H., Roche, O., Khrabrykh, Z., 2008. Propagation and hindered settling of laboratory ash flows. *J. Geophys. Res.* B113: doi: 10.1029/2007JB005074.
- Girolami, L., Druitt, T.H., Roche, O., 2015. Towards a quantitative understanding of pyroclastic flows: Effects of expansion on the dynamics of laboratory fluidized granular flows. *J. Volcanol. Geotherm. Res.* 296: 31-39, <http://dx.doi.org/10.1016/j.jvolgeores.2015.03.008>.
- Gonnermann, H.M., 2015. Magma fragmentation. *Ann. Rev. Earth Planet. Sci.* 43: 431-458, doi: 10.1146/annurev-earth-060614-105206.
- Gonnermann, H.M., Gardner, J.E., 2013. Homogeneous bubble nucleation in rhyolitic melt: Experiments and nonclassical theory. *Geoch. Geophys. Geosyst.* 14: 4758–4773, doi:10.1002/ggge.20281.
- Gonnermann, H.M., Taisne, B., 2015. Magma transport in dikes. In: H. Sigurdsson et al. (Editor), *The encyclopedia of volcanoes*, second edition. Academic Press, pp. 215-224.
- Goto, A., Taniguchi, H., Yoshida, M., Ohba, T., Oshima, H., 2001. Effects of Explosion Energy and Depth to the Formation of Blast Wave and Crater: Field Explosion Experiment for the Understanding of Volcanic Explosion. *Geophys. Res. Lett.* 28(22): 4287-4290.
- Graettinger, A.H., Valentine, G.A., Sonder, I., Ross, P.S., White, J.D.L., Taddeucci, J., 2014. Maar-diatreme geometry and deposits: Subsurface blast experiments with variable explosion depth. *Geochem. Geophys. Geosyst.* 15: 740–764, doi: 10.1002/2013GC005198.
- Gregg, T.K.P., Fink, J.H., 1995. Quantification of submarine lava-flow morphology through analog experiments. *Geology* 23 (1), 73-76.
- Gregg, T.K.P., Fink, J.H., 2000. A laboratory investigation into the effects of slope on lava flows morphology. *J. Volcanol. Geotherm. Res.* 96, 145-159.
- Griffiths, R.W., 2000. The dynamics of lava flows. *Annu. Rev. Fluid Mech.* 32, 477-518.

- Griffiths, R.W., Fink, J.H., 1992. Solidification and morphology of submarine lavas: A dependence on extrusion rate. *J. Geophys. Res. Solid Earth* 97 (B13), 19,729-19,737.
- Griffiths, R.W., Fink, J.H., 1993. Effects of surface cooling on the spreading of lava flows and domes. *J. Fluid Mech.* 252, 667-702.
- Griffiths, R.W., Fink, J.H., 1997. Solidifying Bingham extrusions: a model for the growth of silicic lava domes. *J. Fluid Mech.* 347, 13-36.
- Griffiths, R.W., Kerr, R.C., Cashman, K.V., 2003. Patterns of solidification in channel flows with surface cooling. *J. Fluid Mech.* 496, 33-62.
- Grunder, A.L., Laporte, D., Druitt, T.H., 2005. Experimental and textural investigation of welding: effects of compaction, sintering, and vapor-phase crystallization in the rhyolitic Rattlesnake Tuff. *J. Volcanol. Geotherm. Res.* 142: 89-104, doi:10.1016/j.jvolgeores.2004.10.018.
- Gueugneau, V., Kelfoun, K., Roche, O., Chupin, L., 2017. Effects of pore pressure in pyroclastic flows: Numerical simulation and experimental validation. *Geophys. Res. Lett.* 44, 2194–2202, doi: 10.1002/2017GL072591.
- Hallworth, M.A., Phillips, J.C., Huppert, H.E., Sparks, R.S.J., 1993. Entrainment in turbulent gravity currents. *Nature*, 362: 829-831.
- Hamada, M., Laporte, D., Cluzel, N., Koga, K.T., Kawamoto, T., 2010. Simulating bubble number density of rhyolitic pumices from Plinian eruptions: constraints from fast decompression experiments. *Bull. Volcanol.* 72: 735-746, doi: 10.1007/s00445-010-0353-z.
- Hammer, J.E., Manga, M., Cashman, K.V., 1998. Non-equilibrium and unsteady fluid degassing during slow decompression. *Geophys. Res. Lett.* 25(24): 4565-4568.
- Hammer, J.E., Rutherford, M.J., 2003. Petrologic indicators of pre-eruption magma dynamics. *Geology* 31(1): 79-82.
- Haug, Ø.T., Galland, O., Gisler, G.R., 2013. Experimental modelling of fragmentation applied to volcanic explosions. *Earth Planet. Sci. Lett.* 384: 188–197, doi 10.1016/j.epsl.2013.10.004.
- Hess, K.-U., Cordonnier, B., Lavallée, Y., Dingwell, D.B., 2008. Viscous heating in rhyolite: An in situ experimental determination. *Earth Planet. Sci. Lett.* 275: 121-126.
- Hodge, K.F., Carazzo, G. and Jellinek, A.M., 2012. Experimental constraints on the deformation and breakup of injected magma. *Earth Planet. Sci. Lett.* 325-326: 52-62, doi:10.1016/j.epsl.2012.01.031.
- Holasek, R.E., Woods, A.W., Self, S., 1996. Experiments on gas-ash separation processes in volcanic umbrella clouds. *J. Volcanol. Geotherm. Res.* 70, 169-181.
- Hort, M., Marsh, B.D., Resmini, R.G., Smith, M.K., 1999. Convection and crystallization in a liquid cooled from above: an experimental and theoretical study. *J. Petrology* 40(8), 1271-1300.
- Hulme, G., 1974. The interpretation of lava morphology. *Geophys. J. R. Astro. Soc.* 39, 361-383.
- Huppert H.E., Turner, J.S., 1981. A laboratory model of a replenished magma chamber. *Earth Planet. Sci. Lett.* 54: 144-152.
- Huppert, H.E., Sheperd, J.B., Sigurdsson, H., Sparks, R.S.J., 1982b. On lava dome growth, with application to the 1979 lava extrusion of the Soufrière of St. Vincent. *J. Volcanol. Geoth. Res.* 14, 199-222.
- Huppert, H.E., Turner, J.S., Sparks, R.S.J., 1982a. Replenished magma chambers: effects of compositional zonation and input rates. *Earth Planet. Sci. Lett.* 57: 345-357.
- Huppert, H.E., Sparks, R.S.J., 1984. Double-diffusive convection due to crystallization in magmas. *Ann. Rev. Earth Planet. Sci.* 12, 11-37.
- Huppert, H.E., Sparks, R.S.J., Turner, J.S., Arndt, N.T., 1984. Emplacement and cooling of komatiite lavas. *Nature* 309, 19-22.
- Huppert, H.E., Turner, J.S., Carey, S.N., Sparks, R.S.J., Hallworth, M.A., 1986. A laboratory simulation of pyroclastic flows down slopes. *J. Volcanol. Geotherm. Res.* 30: 179-199.
- Huppert, H.E., Sparks, R.S.J., 1988a. The generation of granitic magmas by intrusion of basalt into continental crust. *J. Petrology* 29(3): 599-624.
- Huppert, H.E., Sparks, R.S.J., 1988b. Melting the roof of a chamber containing a hot, turbulently convecting fluid. *J. Fluid Mech.* 188: 107-131.
- Huppert, H.E., 2006. Gravity currents: a personal perspective. *J. Fluid Mech.* 554: 299-322.
- Hurwitz, S., Navon, O., 1994. Bubble nucleation in rhyolitic melts: Experiments at high pressure, temperature, and water content. *Earth Planet. Sci. Lett.* 122: 267-280.
- Ichihara, M., 2008. Dynamics of a spherical viscoelastic shell: Implications to a criterion for fragmentation/expansion of bubbly magma. *Earth Planet. Sci. Lett.* 265: 18-32, doi:10.1016/j.epsl.2007.09.033.
- Ichihara, M., Ripepe, M., Goto, A., Oshima, H., Aoyama, H., Iguchi, M., Tanaka, K., Taniguchi, H., 2009. Airwaves generated by an underwater explosion: Implications for volcanic infrasound. *J. Geophys. Res.* 114: B03210, doi: 10.1029/2008JB005792.
- Ichihara, M., Lyons, J.J., Yokoo, A., 2013. Switching from seismic to seismo-acoustic harmonic tremor at a transition of eruptive activity during the Shinmoe-dake 2011 eruption. *Earth Planets Space*, 65: 633–643, doi:10.5047/eps.2013.05.003.
- Ichihara, M., Rittel, D., Sturtevant, B., 2002. Fragmentation of a porous viscoelastic material: Implications to magma fragmentation. *J. Geophys. Res.* 107(B10): 2229, doi: 10.1029/2001JB000591.
- Ichihara, M., Ohkunitani, I., Ida, Y., Kameda, M., 2004. Dynamics of bubble oscillation and wave propagation in viscoelastic liquids. *J. Volcanol. Geotherm. Res.* 129: 37-60.
- Ito, G., Martel, S.J., 2002. Focusing of magma in the upper mantle through dike interaction. *J. Geophys. Res.* 107, B102223, doi: 10.1029/2001JB000251.
- Iverson, R.M., 1997. The physics of debris flows. *Rev. Geophys.* 35(3): 245-296.
- Iverson, R.M., 2015. Scaling and design of landslide and debris-flow experiments. *Geomorphology* 244, 9-20.
- Iverson, R.M., Denlinger, R.P., 2001. Flow of variably fluidized granular masses across three-dimensional terrain I. Coulomb mixture theory. *J. Geophys. Res.* 106(B1): 537-552.

- Iverson, R., Logan, M., LaHusen, R.G., Berti, M., 2010. The perfect debris flow? Aggregated results from 28 large-scale experiments. *J. Geophys. Res.* 115: F03005, doi: 10.1029/2009JF001514.
- James, M.R., Lane, S.J., Chouet, B., Gilbert, J.S., 2004. Pressure changes associated with the ascent and bursting of gas slugs in liquid-filled vertical and inclined conduits. *J. Volcanol. Geotherm. Res.* 129: 61-82, doi: 10.1016/S0377-0273(03)00232-4.
- James, M.R., Lane, S.J., Gilbert, J.S., 1998. Volcanic plume monitoring using atmospheric electric potential gradients. *J. Geol. Soc. London*, 155: 587-590.
- James, M.R., Lane, S.J., Gilbert, J.S., 2000. Volcanic plume electrification: Experimental investigation of a fracture-charging mechanism. *J. Geophys. Res.* 105(B7): 16641-16649.
- James, M.R., Gilbert J.S., Lane, S.J., 2002. Experimental investigation of volcanic particle aggregation in the absence of a liquid phase. *J. Geophys. Res.* 107, B9, 2191.
- James, M.R., Lane, S.J., Gilbert, J.S., 2003. Density, construction, and drag coefficient of electrostatic volcanic ash aggregates. *J. Geophys. Res.* 108, B9, 2435.
- Jaupart, C., Vergnolle, S., 1988. Laboratory models of Hawaiian and Strombolian eruptions. *Nature*, 331(6151): 58-60.
- Jaupart, C., Vergnolle, S., 1989. The generation and collapse of a foam layer at the roof of a basaltic magma chamber. *J. Fluid Mech.* 203: 347-380.
- Jellinek, A.M., Kerr, R.C., Griffiths, R.W., 1999. Mixing and compositional stratification produced by natural convection. 1. Experiments and their application to Earth's core and mantle. *J. Geophys. Res.* 104(B4): 7183-7201.
- Jellinek, A.M., Kerr, R.C., 1999. Mixing and compositional stratification produced by natural convection. 2. Applications to the differentiation of basaltic and silicic magma chambers and komatiite lava flows. *J. Geophys. Res.* 104(B4): 7203-7218.
- Jessop, D.E., Gilchrist, J., Jellinek, A.M., Roche, O., 2016. Are eruptions from linear fissures and caldera ring more likely to produce pyroclasts flows? *Earth Planet. Sci. Lett.* 454, 142-153.
- Jessop, D.E., Jellinek, A.M., 2014. Effects of particle mixtures and nozzle geometry on entrainment into volcanic jets. *Geophys. Res. Lett.* 41, doi: 10.1002/2014GL060059.
- Jessop, D.E., Kelfoun, K., Labazuy, P., Mangeny, A., Roche, O., Tilliere, J.-L., Trouillete, Thibault, M.G., 2012. LiDAR derived morphology of the 1993 Lascar pyroclastic flow deposits, and implication for flow dynamics and rheology. *J. Volcanol. Geotherm. Res.*, 245-246: 81-97, doi: 10.1016/j.jvolgeores.2012.06.030.
- Kameda, M., Ichihara, M., Maruyama, S., Kurokawa, N., Aoki, Y., Okumura, S., Uesugi, K., 2017. Advancement of magma fragmentation by inhomogeneous bubble distribution. *Scientific Reports*, 7: 16755, doi: 10.1038/s41598-017-16941-x.
- Kameda, M., Ichihara, M., Shimanuki, S., Okabe, W., Shida, T., 2013. Delayed brittle-like fragmentation of vesicular magma analogue by decompression. *J. Volcanol. Geotherm. Res.* 258: 113-125, doi 10.1016/j.jvolgeores.2013.04.008.
- Kameda, M., Kuribara, H., Ichihara, M., 2008. Dominant time scale for brittle fragmentation of vesicular magma by decompression. *Geophys. Res. Lett.* 35: L14302, doi: 10.1029/2008GL034530.
- Kaminski, E., Tait, S., Carazzo, G., 2005. Turbulent entrainment in jets with arbitrary buoyancy. *J. Fluid Mech.* 526, 361-376.
- Kaneko, K., Koyaguchi, T., 2000. Simultaneous crystallization and melting at both the roof and floor crustal magma chambers: Experimental study using NH<sub>4</sub>Cl-H<sub>2</sub>O binary eutectic system. *J. Volcanol. Geotherm. Res.* 96: 161-174.
- Kaneko, K., Koyaguchi, T., 2004. Experimental study on the effects of crustal temperature and composition on assimilation with fractional crystallization at the floor of magma chambers. *J. Volcanol. Geotherm. Res.* 129: 155-172.
- Kanno, Y., Ichihara, M., 2018. Sawtooth wave-like pressure changes in a syrup eruption experiment: implications for periodic and nonperiodic volcanic oscillations. *Bulletin of Volcanology*, 80: 65, <https://doi.org/10.1007/s00445-018-1227-z>.
- Kavanagh, J.L., Boutelier, D., Cruden, A.R., 2015. The mechanics of sill inception, propagation and growth: Experimental evidence for rapid reduction in magmatic overpressure. *Earth Planet. Sci. Lett.* 421: 117-128, <http://dx.doi.org/10.1016/j.epsl.2015.03.038>.
- Kavanagh, J.L., Engwell, S.L., Martin, S.A., 2018. A review of laboratory and numerical modelling in volcanology. *Solid Earth*, 9: 531-571, <https://doi.org/10.5194/se-9-531-2018>.
- Kavanagh, J.L., Menand, T., Daniels, K.A., 2013. Gelatine as a crustal analogue: Determining elastic properties for modelling magmatic intrusions. *Tectonophysics*, 582: 101-111, <http://dx.doi.org/10.1016/j.tecto.2012.09.032>.
- Kavanagh, J.L., Menand, T., Sparks, R.S.J., 2006. An experimental investigation of sill formation and propagation in layered elastic media. *Earth Planet. Sci. Lett.* 245: 799-813, doi:10.1016/j.epsl.2006.03.025.
- Kavanagh, J.L., Burns, A.J., Hilmi Hazima, S., Wood, E.P., Martin, S.A., Hignett, S., Dennis, D.J.C., 2018. Challenging dyke ascent models using novel laboratory experiments: Implications for reinterpreting evidence of magma ascent and volcanism. *J. Volcanol. Geotherm. Res.*, 354: 87-101, <https://doi.org/10.1016/j.jvolgeores.2018.01.002>.
- Kennedy, B.M., Jellinek, A.M., Stix, J., 2008. Coupled caldera subsidence and stirring inferred from analogue models. *Nature Geoscience* 1: 385-389.
- Kerr, R.C., 2009. Thermal erosion of felsic ground by the laminar flow of a basaltic lava, with application to the cave Basalt, Mount St. Helens, Washington. *J. Geophys. Res.* 114, B09204, doi: 10.1029/2009JB006430.
- Kerr, R.C., Griffiths, R.W., Cashman, K.V., 2006. Formation of channelized lava flows on an unconfined slope. *J. Geophys. Res.* 111, B10206, doi: 10.1029/2005JB004225.
- Kervyn, M., Ernst, G.G.J., van Wyk de Vries, B., Mathieu, L., Jacobs, P., 2009. Volcano load control on dyke propagation and vent distribution: Insights from analogue modeling. *J. Geophys. Res.* 114: B03401, doi: 10.1029/2008JB005653.
- Kieffer, S.W., Sturtevant, B., 1984. Laboratory studies of volcanic jets. *J. Geophys. Res.* 89, B10, 8253-8268.
- Kitamura, S., Sumita, I., 2011. Experiments on a turbulent plume: Shape analyses. *J. Geophys. Res.* 116, B032208, doi: 10.1029/2010JB007633.
- Kotsovinos, N.E., 2000. Axisymmetric submerged intrusion in stratified fluid. *J. Hydraulic Eng.* 1265: 446-456.
- Koyaguchi, T., Hallworth, M.A., Huppert, H.E., 1993. An experimental study on the effects of phenocrysts on convection in magmas. *J. Volcanol. Geotherm. Res.* 55: 15-32.

- Koyaguchi, T., Scheu, B., Mitani, N.K. and Melnik, O., 2008. A fragmentation criterion for highly viscous bubbly magmas estimated from shock tube experiments. *J. Volcanol. Geotherm. Res.* 178: 58-71, doi: 10.1016/j.volgeores.2008.02.008.
- Koyaguchi, T., Ochiai, K., Suzuki, Y.J., 2009. The effect of intensity of turbulence in umbrella cloud on tephra dispersion during explosive volcanic eruptions: Experimental and numerical approaches. *J. Volcanol. Geotherm. Res.* 186, 68-78.
- Kueppers, U., Perugini, D., Dingwell, D.B., 2006a. "Explosive energy" during volcanic eruptions from fractal analysis of pyroclasts. *Earth Planet. Sci. Lett.* 248: 800-807, doi:10.1016/j.epsl.2006.06.033.
- Kueppers, U., Scheu, B., Spieler, O., Dingwell, D.B., 2006b. Fragmentation efficiency of explosive volcanic eruptions: A study of experimentally generated pyroclasts. *J. Volcanol. Geotherm. Res.*, 153: 125-135, doi:10.1016/j.volgeores.2005.08.006.
- Lane, S.J., Chouet, B., Phillips, J.C., Dawson, P., Ryan, G.A., Hurst, E., 2001. Experimental observations of pressure oscillations and flow regimes in an analogue volcanic system. *J. Geophys. Res.* 106(B4): 6461-6476.
- Lane, S.J., James, M.R., 2011. Volcanic Eruptions, Explosive: Experimental Insights. In: R.A. Meyers (Editor), *Extreme environmental events - Complexity in forecasting and early warning*. Springer, pp. 1035-1081.
- Lane, S.J., Phillips, J. and Ryan, G.A., 2008. Dome-building eruptions: insights from analogue experiments. In: S.J. Lane and J.S. Gilbert (Editors), *Fluid Motions in Volcanic Conduits: A Source of Seismic and Acoustic Signals*. Geol. Soc. London, Spec. Pub., pp. 207-237, doi: 10.1144/SP307.
- Lavallée, Y. et al., 2012. Experimental generation of volcanic pseudotachylytes: Constraining rheology. *J. Struct. Geol.* 38: 222-233, doi:10.1016/j.jsg.2012.02.001.
- Le Corvec, N., Menand, T., Lindsay, J., 2013. Interaction of ascending magma with pre-existing crustal fractures in monogenetic basaltic volcanism: an experimental approach. *J. Geophys. Res.* 118: 968-984, doi:10.1002/jgrb.50142.
- Legros, F., Druitt, T.H., 2000. On the emplacement of ignimbrite in submarine environments. *J. Volcanol. Geotherm. Res.* 95: 9-22.
- Leitch, A.M., 2004. Analog experiments on melting and contamination at the roof and walls of magma chambers. *J. Volcanol. Geotherm. Res.* 129: 173-197.
- Lensky, N.G., Navon, O., Lyakhovskiy, V., 2004. Bubble growth during decompression of magma: experimental and theoretical investigation. *J. Volcanol. Geotherm. Res.* 129: 7-22, doi: 10.1016/S0377-0273(03)00229-4.
- Lescinsky, D.T., Merle, O., 2005. Extensional and compressional strain in lava flows and the formation of fractures in surface crust. *Geol. Soc. Am. Spec. Pap.* 396, 163-179.
- Lev, E., Spiegelman, M., Wysicki, R.J., Karson, J.A., 2012. Investigating lava flow rheology using video analysis and numerical flow models. *J. Volcanol. Geoth. Res.* 247-248, 62-73.
- Linden, P.F., 2000. Convection in the environment. In *Perspectives in Fluid Dynamics* (ed. G.K. Batchelor, H.K. Moffat, M.G. Worster). Cambridge University Press.
- Llewellyn, E.W., Mader, H.M., Wilson, S.D.R., 2002. The rheology of a bubbly liquid. *Proc. R. Soc. Lond. A* 458: 987-1016.
- Llewellyn, E.W., Del Bello, E., Taddeucci, J., Scarlato, P., Lane, S.J., 2012. The thickness of the falling film of liquid around a Taylor bubble. *Proc. Royal Soc. London A*, 468: 1041-1064, doi:10.1098/rspa.2011.0476.
- Lodge, R.W.D., Lescinsky, D.T., 2009. Anisotropic stress accumulation in cooling lava flows and resulting fracture patterns: insights from starch-water desiccation experiments. *J. Volcanol. Geoth. Res.* 185, 323-336.
- Lube, G., Breard, E.C.P., Cronin, S.J. and Jones, J., 2015. Synthesizing large-scale pyroclastic flows: Experimental design, scaling, and first results from PELE. *J. Geophys. Res.* 120: 1487-1502, doi: 10.1002/2014JB011666.
- Lube, G., Breard, E.C.P., Jones, J., Fullard, L., Dufek, J., Crinin, S.J., Wang, T., 2019. Generation of air lubrication within pyroclastic density currents. *Nat. Geosci.*, 12: 381-386, <https://doi.org/10.1038/s41561-019-0338-2>.
- Lyman, A.W., Koenig, E., Fink, J.H., 2004. Predicting yield strengths and effusion rates of lava domes from morphology and underlying topography. *J. Volcanol. Geoth. Res.* 129, 125-138.
- Lyman, A.W., Kerr, R.C., Griffiths, R.W., 2005. Effects of internal rheology and surface cooling on the emplacement of lava flows. *J. Geophys. Res.* 110, B08207, doi: 10.1029/JB003643.
- Lyman, A.W., Kerr, R.C., 2006. Effect of surface solidification on the emplacement of lava flows on a slope. *J. Geophys. Res.* 111, B05206, doi: 10.1029/JB004133.
- Lyons, J.L., Ichihara, M., Kurokawa, A., Lees, J.M., 2013. Switching between seismic and seismo-acoustic harmonic tremor simulated in the laboratory: Insights into the role of open degassing channels and magma viscosity. *J. Geophys. Res.* 118: 277-289, doi:10.1002/jgrb.50067.
- Macorps, E., Graettinger, A.H., Valentine, G.A., Ross, P-S., White, J.D.L., Sonder, I., 2016. The effects of the host-substrate properties on maar-diatreme volcanoes: experimental evidence. *Bull. Volcanol.* 78: 26, doi: 10.1007/s00445-016-1013-8.
- Mader, H.M., Brodsky, E.E., Howard, D., Sturtevant, B., 1997. Laboratory simulations of sustained volcanic eruptions. *Nature*, 388: 462-464.
- Mader, H.M., Manga, M., Koyaguchi, T., 2004. The role of laboratory experiments in volcanology. *J. Volcanol. Geotherm. Res.* 129: 1-5.
- Mader, H.M., Phillips, J.C., Sparks, R.S.J., Sturtevant, B., 1996. Dynamics of explosive degassing of magma: Observations of fragmenting two-phase flows. *J. Geophys. Res.* 101(B3): 5547-5560.
- Mader, H.M., Zhang, Y., Phillips, J.C., Sparks, R.S.J., Sturtevant, B., Stolper, E., 1994. Experimental simulations of explosive degassing of magma. *Nature*, 372: 85-88.
- Manga, M., Castro, J., Cashman, K.V., Loewenberg, M., 1998. Rheology of bubble-bearing magmas. *J. Volcanol. Geotherm. res.* 87, 15-28.
- Manga, M., Patel, A., Dufek, J., 2011. Rounding of pumice clasts during transport: field measurements and laboratory studies. *Bull. Volcanol.* 73: 321-333, doi: 10.1007/s00445-010-0411-6.
- Mangan, M. and Sisson, T., 2000. Delayed, disequilibrium degassing in rhyolite magma: decompression experiments and implications for explosive volcanism. *Earth Planet. Sci. Lett.* 183: 441-455.
- Mangeney, A., Roche, O., Hungr, O., Mangold, N., Faccanoni, G., Lucas, A., 2010. Erosion and mobility in granular collapse over sloping beds. *J. Geophys. Res.*, 115: F03040, doi: 10.1029/2009JF001462.

- Manzella, I., Bonadonna, C., Phillips, J., Monnard, H., 2015. The role of gravitational instabilities in deposition of volcanic ash. *Geology* 43, 3, 211-214.
- Martel, C., Dingwell, D.B., Spieler, O., Pichavant, M., Wilke, M., 2000. Fragmentation of foamed silicic melts: an experimental study. *Earth Planet. Sci. Lett.* 178: 47-58.s
- Martin, D., Nokes, R., 1989. A fluid-dynamical study of crystal settling in convecting magmas. *J. Petrology* 30(6): 1471-1500.
- Mayer, K., Scheu, B., Gilg, H.A., Heap, M.J., Kennedy, B., Lavallée, Y., Letham-Brake, M., Dingwell, D.B., 2015. Experimental constraints on phreatic eruption processes at Whakaari (White Island volcano). *J. Volcanol. Geotherm. Res.* 302: 150-162, <http://dx.doi.org/10.1016/j.jvolgeores.2015.06.014>.
- McLeod, P., Tait, S., 1999. The growth of dykes from magma chambers. *J. Volcanol. Geotherm. Res.* 92: 231-246.
- McTaggart, K.C., 1960. The mobility of nuées ardentes. *Am. J. Sci.* 258: 369-382.
- Medici, E.F., Allen, J.S., Waite, G.P., 2014. Modeling shock waves generated by explosive volcanic eruptions. *Geophys. Res. Lett.* 41, 414-421, doi: 10.1002/2013GL058340.
- Medici, E.F., Waite, G.P., 2016. Experimental laboratory study on the formation of multiple shock waves observed during volcanic eruptions. *Geophys. Res. Lett.* 43, 85-92, doi: 10.1002/2015GL066426.
- Menand, T., Daniels, K.A., Benghiat, P., 2010. Dyke propagation and sill formation in a compressive tectonic environment. *J. Geophys. Res.* 115: B08201, doi: 10.1029/2009JB006791.
- Menand, T., Tait, S.R., 2001. A phenomenological model for precursor volcanic eruptions. *Nature*, 411: 678-680.
- Menand, T. and Tait, S., 2002. The propagation of a buoyant liquid-filled fissure from a source under constant pressure: An experimental approach. *J. Geophys. Res.* 107(B11): 2306, doi: 10.1029/2001JB000589.
- Méndez Harper, J.S., Cimarelli, C., Dufek, J., Gaudin, D. and Thomas, R.J., 2018. Inferring compressible fluid dynamics from vent discharges during volcanic eruptions. *Geophysical Research Letters*, 45: <https://doi.org/10.1029/2018GL078286>.
- Merle, O., 1998. Internal strain within lava flows from analogue modelling. *J. Volcanol. Geoth. Res.* 81, 189-206.
- Merle, O., 2015. The scaling of experiments on volcanic systems. *Frontiers in Earth Sciences*, 3: 26, doi: 10.3389/feart.2015.00026.
- Mier-Torrecilla, M., Geyer, A., Phillips, J.C., Idelsohn, S.R. and Oñate, E., 2012. Numerical simulations of negatively buoyant jets in an immiscible fluid using the Particle Finite Element Method. *Int. J. Numer. Meth. Fluids*, 69: 1016-1030, doi: 10.1002/flid.2628.
- Montanaro, C., Scheu, B., Mayer, K., Orsi, G., Moretti, R., Isaia, R., Dingwell, D.B., 2016. Experimental investigations on the explosivity of steam-driven eruptions: A case study of Solfatara volcano (Campi Flegrei). *J. Geophys. Res.* 121: doi: 10.1002/2016JB013273.
- Montanaro, C., Scheu, B., Cronin, S.J., Breard, E.C.P., Lube, G., Dingwell, D.B., 2016. Experimental estimates of the energy budget of hydrothermal eruptions; application to 2012 Upper Te Maari eruption, New Zealand. *Earth Planet. Sci. Lett.* 452: 281-294, <http://dx.doi.org/10.1016/j.epsl.2016.07.052>.
- Montserrat, S., Tamburrino, A., Roche, O., Niño, Y., 2012. Pore fluid pressure diffusion in defluidizing granular columns. *J. Geophys. Res.* 117: F02034, doi: 10.1029/2011JF002164.
- Morton, B.R., Taylor, G.I., Turner, J.S., 1956. Turbulent gravitational convection from maintained and instantaneous sources. *Proc. R. Soc. Lond. A* 234, 1-23.
- Mourtada-Bonnefoi, C.C., Laporte, D., 1999. Experimental study of homogeneous nucleation in rhyolitic magmas bubble. *Geophys. Res. Lett.* 26(23): 3505-3508.
- Mourtada-Bonnefoi, C.C., Laporte, D., 2004. Kinetics of bubble nucleation in a rhyolitic melt: an experimental study of the effect of ascent rate. *Earth Planet. Sci. Lett.* 218: 521-537, doi: 10.1016/S0012-821X(03)00684-8.
- Mourtada-Bonnefoi, C.C., Mader, H.M., 2004. Experimental observations of the effect of crystals and pre-existing bubbles on the dynamics and fragmentation of vesiculating flows. *J. Volcanol. Geotherm. Res.* 129: 83-97, doi: 10.1016/S0377-0273(03)00233-6.
- Mueller, S.B., Lane, S.J., Kueppers, U., 2015. Lab-scale ash production by abrasion and collision experiments of porous volcanic samples. *J. Volcanol. Geotherm. Res.* 302: 163-172, doi: 10.1016/j.jvolgeores.2015.07.013.
- Mueller, S., Scheu, B., Spieler, O., Dingwell, D.B., 2008. Permeability control on magma fragmentation. *Geology*, 36(5): 399-402, doi: 10.1130/G24605A.
- Mueller, S., Llewellyn, E.W., Mader, H.M., 2010. The rheology of suspensions of solid particles. *Proc. R. Soc. A* 466: 1201-1228.
- Mueller, S., Llewellyn, E.W., Mader, H.M., 2011. The effect of particle shape on suspension viscosity and implications for magmatic flows. *Geophys. Res. Lett.* 38, L13316, doi: 10.1029/2011GL047167.
- Mueller, S.B., Kueppers, U., Ayris, P.M., Jacob, M., Dingwell, D.B., 2016. Experimental volcanic ash aggregation: Internal structure of accretionary lapilli and the role of liquid bonding. *Earth Planet. Sci. Lett.* 433, 232-240.
- Müller, G., 1998a. Experimental simulation of basalt columns. *J. Volcanol. Geotherm. Res.* 86, 93-96.
- Müller, G., 1998b. Starch columns: analog model for basalt columns. *J. Geophys. Res.* 103, 15,239-15,253.
- Muller, J.R., Ito, G., Martel, S.J., 2001. Effects of volcano loading on dike propagation in an elastic half-space. *J. Geophys. Res.* 106(B6): 11101-11113.
- Murase, T., McBirney, A.R., 1973. Properties of some common igneous rocks and their melts at high temperatures. *Geol. Soc. Am. Bull.* 84: 3563-3592.
- Namiki, A., Ueno, Y., Hurwitz, S., Manga, M., Munoz-Saez, C., Murphy, F., 2016. An experimental study of the role of subsurface plumbing on geothermal discharge. *Geochem. Geophys. Geosyst.* 17: 3691-3716, doi: 10.1002/2016GC006472.
- Namiki, A., 2012. An empirical scaling of shear-induced outgassing during magma ascent: Intermittent magma ascent causes effective outgassing. *Earth Planet. Sci. Lett.* 353-354: 72-81, <http://dx.doi.org/10.1016/j.epsl.2012.08.007>.
- Namiki, A., Manga, M., 2005. Response of a bubble bearing viscoelastic fluid to rapid decompression: Implications for explosive volcanic eruptions. *Earth Planet. Sci. Lett.* 236: 269-284, doi:10.1016/j.epsl.2005.02.045.

- Namiki, A., Manga, M., 2006. Influence of decompression rate on the expansion velocity and expansion style of bubbly fluids. *J. Geophys. Res.* 111: B11208, doi: 10.1029/2005JB004132.
- Namiki, A., Manga, M., 2008. Transition between fragmentation and permeable outgassing of low viscosity magmas. *J. Volcanol. Geotherm. Res.* 169: 48-60, doi:10.1016/j.jvolgeores.2007.07.020.
- Namiki, A., Rivalta, E., Woith, H., Walter, T.R., 2016. Sloshing of a bubbly magma reservoir as a mechanism of triggered eruptions. *J. Volcanol. Geotherm. Res.* 320: 156-171. Namiki, A., Rivalta, E., Woith, H., Willey, T., Parolai, S., Walter, T.R., 2018. Volcanic activities triggered or inhibited by resonance of volcanic edifices to large earthquakes. *Geology* 47:67-70, <https://doi.org/10.1130/G45323.45321>.
- National Academies of Sciences, Engineering, and Medicine, 2017. *Volcanic Eruptions and Their Repose, Unrest, Precursors, and Timing (ERUPT)*. Washington, DC: The National Academies Press. <https://doi.org/10.17226/24650>.
- Ohadhi, M., Ichihara, M., Toramaru, A., 2018. Bubble deformation in magma under transient flow conditions. *J. Volcanol. Geotherm. Res.* 364: 59-75.
- Okumura, S., Nakamura, M., Takeuchi, S., Tsuchiyama, A., Nakamura, M., Uesugi, K., 2009. Magma deformation may induce non-explosive volcanism via degassing through bubble networks. *Earth Planet. Sci. Lett.* 281: 267-274, doi: 10.1016/j.epsl.2009.02.036.
- Orescanin, M.M., Austin, J.M., Kieffer, S.W., 2010. Unsteady high-pressure flow experiments with applications to explosive volcanic eruptions. *J. Geophys. Res.* 115: B06206, doi: 10.1029/2009JB006985.
- Orescanin, M.M., Prisco, D., Austin, J.M., Kieffer, S.W., 2014. Flow of supersonic jets across flat plates: Implications for ground-level flow from volcanic blasts. *J. Geophys. Res.*, 119: 2976–2987, doi: 10.1002/2013JB010743.
- Paguican, E.M.R., van Wyk de Vries, B., Lagmay, A., 2012. Hummocks: how they form and how they evolve in rockslide-debris avalanches. *Landslides*, doi 10.1007/s10346-012-0368-y.
- Paillat, S., Kaminski, E., 2014a. Entrainment in plane turbulent pure plumes. *J. Fluid Mech.* 755, R2, doi:10.1017/jfm.2014.424.
- Paillat, S., Kaminski, E., 2014b. Second-order model of entrainment in planar turbulent jets at low Reynolds number. *Phys. Fluids* 26, 045110. doi:10.1063/1.4871521.
- Paola, C., Straub, K., Mohrig, D., Reinhardt, L., 2009. The “unreasonable effectiveness” of stratigraphic and geomorphic experiments. *Earth-Sci. Rev.* 97, 1-43.
- Pering, R.D., McGonigle, A.J.S., James, M.R., Capponi, A., Lane, S.J., Tamburello, G., Aiuppa, A., 2017. The dynamics of slug trains in volcanic conduits: Evidence for expansion driven slug coalescence. *J. Volcanol. Geotherm. Res.* 348: 26-35, <https://doi.org/10.1016/j.jvolgeores.2017.10.009>.
- Phillips, J.C., Lane, S.J., Lejeune, A.M., Hilton, M., 1995. Gum rosin-acetone system as an analogue to the degassing behaviour of hydrated magmas. *Bull. Volcanol.* 57: 263-268.
- Phillips, J.C., Woods, A.W., 2001. Bubble plumes generated during recharge of basaltic magma reservoirs. *Earth Planet. Sci. Lett.* 186: 297-309.
- Pioli, L., Bonadonna, C., Azzopardi, B.J., Phillips, J., Ripepe, M., 2012. Experimental constraints on the outgassing dynamics of basaltic magmas. *J. Geophys. Res.* 117: B03204, doi: 10.1029/2011JB008392.
- Quane, S.L., Russell, J.K., 2005. Welding: insights from high-temperature analogue experiments. *J. Volcanol. Geotherm. Res.* 142: 67-87, doi:10.1016/j.jvolgeores.2004.10.014.
- Renggli, C.J., Wiesmaier, S., De Campos, C.P., Hess, K.-U., Dingwell, D.B., 2016. Magma mixing induced by particle settling. *Contrib. Mineral. Petrol.* 171:96-109.
- Reynolds, O., 1883. An experimental investigation of the circumstances which determine whether the motion of water shall be direct or sinous, and of the law of resistances in parallel channels. *Phil. Trans. Roy. Soc. London* 174: 935-982.
- Rivalta, E., Böttinger, M., Dahm, T., 2005. Buoyancy-driven fracture ascent: Experiments in layered gelatine. *J. Volcanol. Geotherm. Res.* 144: 273-285, doi:10.1016/j.jvolgeores.2004.11.030.
- Rivalta, E., Pascal, K., Phillips, J.C., 2013. Explosive expansion of a slowly decompressed magma analogue: Evidence for delayed bubble nucleation. *Geochem. Geophys. Geosyst.* 14(8): 3067–3084, doi: 10.1002/ggge.20183.
- Roche, O., 2012. Depositional processes and gas pore pressure in pyroclastic flows: an experimental perspective. *Bull. Volcanol.* 74: 1807–1820, doi: 10.1007/s00445-012-0639-4.
- Roche, O., Niño, Y., Mangeney, A., Brand, B., Pollock, N., Valentine, G.A., 2013. Dynamic pore-pressure variations induce substrate erosion by pyroclastic flows. *Geology*, 41(10): 1107–1110, doi:10.1130/G34668.1.
- Roche, O., Buesch, D.C., Valentine, G.A., 2016. Slow-moving and far-travelled dense pyroclastic flows during the Peach Spring super-eruption. *Nat. Comm.* 7: 10890, doi: 10.1038/ncomms10890.
- Roche, O., Montserrat, S., Niño, Y., Tamburrino, A., 2008. Experimental observations of water-like behavior of initially fluidized, dam break granular flows and their relevance for the propagation of ash-rich pyroclastic flows. *J. Geophys. Res.* 113: B12203, doi: 10.1029/2008JB005664.
- Rodriguez-Sedano, L.A., Sarocchi, D., Sulpizio, R., Borselli, L., Campos, G., Moreno Chavez, G., 2016. Influence of particle density on flow behavior and deposit architecture of concentrated pyroclastic density currents over a break in slope: Insights from laboratory experiments. *J. Volcanol. Geotherm. Res.*, 328: 178–186, <http://dx.doi.org/10.1016/j.jvolgeores.2016.10.017>.
- Ross, P.-S., White, J.D.L., Valentine, G.A., Taddeucci, J., Sonder, I., Andrews, R.G., 2013. Experimental birth of a maar-diatreme volcano. *J. Volcanol. Geotherm. Res.* 260: 1-12, <http://dx.doi.org/10.1016/j.jvolgeores.2013.05.005>.
- Ross, P.-S., White, J.D.L., Zimanowski, B., Büttner, R., 2008. Multiphase flow above explosion sites in debris-filled volcanic vents: insights from analogue experiments. *J. Volcanol. Geotherm. Res.* 178: 104-112, doi: 10.1016/j.jvolgeores.2008.01.013.
- Ross, P.-S., White, J.D.L., Zimanowski, B., Büttner, R., 2008. Rapid injection of particles and gas into non-fluidized granular material, and some volcanological implications. *Bull. Volcanol.* 70: 1151-1168, doi: 10.1007/s00445-008-0230-1.
- Rowley, P.J., Roche, O., Druitt, T.H., Cas, R.A.F., 2014. Experimental study of dense pyroclastic density currents using sustained, gas-fluidized granular flows. *Bull. Volcanol.* 76: 855, doi 10.1007/s00445-014-0855-1.

- Rust, A.C., Manga, M., 2002. Effects of bubble deformation on the viscosity of dilute suspensions. *J. Non-Newtonian Fluid Mech.* 104: 53-63.
- Rust, A.C., Balmforth, N.J., Mandre, S., 2008. The feasibility of generating low-frequency volcano seismicity by flow through a deformable channel. In: S.J.G. LANE, J. S. (Editor), *Fluid Motions in Volcanic Conduits: A Source of Seismic and Acoustic Signals*. Geol. Soc. London, Spec. Pub., pp. 45–56, doi: 10.1144/SP307.
- Sakimoto, S.E.H., Gregg, T.K.P., 2001. Channeled flow: Analytic solutions, laboratory experiments, and applications to lava flows. *J. Geophys. Res.* 106 (B5), 8629-8644.
- Sato, H., Taniguchi, H., 1997. Relationship between crater size and ejecta volume of recent magmatic and phreato-magmatic eruptions: Implications for energy partitioning. *Geophys. Res. Lett.* 24(3): 205-208.
- Sato, E., Sato, H., 2009. Study of effect of magma pocket on mixing of two magmas with different viscosities and densities by analogue experiments. *J. Volcanol. Geotherm. Res.* 181: 115-123.
- Savage, S.B., 1984. The mechanics of rapid granular flows. *Advances in applied mechanics*, 24: 289-366.
- Scaillet, B., Pichavant, M., Cioni, R., 2008. Upward migration of Vesuvius magma chamber over the past 20,000 years. *Nature* 455: 216-220, doi: 10.1038/nature07232.
- Scollo, S., Bonadonna, C., Manzella, I., 2017. Settling-driven gravitational instabilities associated with volcanic clouds: new insights from experimental investigations. *Bull. Volcanol.* 79, 39-53.
- Shea, T., Van Wyk de Vries, B., 2008. Structural analysis and analogue modeling of the kinematics and dynamics of rockslide avalanches. *Geosphere*, 4(4): 657-686, doi: 10.1130/GES00131.1.
- Scheu, B., Kueppers, U., Mueller, S., Spieler, O., Dingwell, D.B., 2008. Experimental volcanology on eruptive products of Unzen volcano. *J. Volcanol. Geotherm. Res.* 175: 110-119, doi:10.1016/j.jvolgeores.2008.03.023.
- Scheu, B., Spieler, O., Dingwell, D.B., 2006. Dynamics of explosive volcanism at Unzen volcano: an experimental contribution. *Bull. Volcanol.* 69: 175-187, doi: 10.1007/s00445-006-0066-5.
- Schumacher, R., 1994. A reappraisal of Mount St. Helens's ash clusters – depositional model from experimental observation. *J. Volcanol. Geotherm. Res.* 59, 253-260.
- Sher, D., Woods, A.W. 2017. Experiments on mixing in pyroclastic density currents generated from short-lived volcanic explosions. *Earth Planet. Sci. Lett.* 467: 138-148, <http://dx.doi.org/10.1016/j.epsl.2017.03.009>.
- Shibano, Y., Namiki, A., Sumita, I., 2012. Experiments on upward migration of a liquid-rich layer in a granular medium: Implications for a crystalline magma chamber. *Geochemistry, Geophysics, Geosystems* 13: Q03007, doi: 10.1029/2011GC003994.
- Shields, J.K., Mader, H.M., Pistone, M., Caricchi, L., Floess, D., Putlitz, B., 2014. Strain-induced outgassing of three-phase magmas during simple shear. *J. Geophys. Res.* 119: 6936–6957, doi: 10.1002/2014JB011111.
- Seyfried, R., Freundt, A., 2000. Experiments on conduit flow and eruption behavior of basaltic volcanic eruptions. *J. Geophys. Res.* 105(B10): 23727-23740.
- Solovitz, S.A., Mastin, L.G., 2009. Experimental study of near-field air entrainment by subsonic volcanic jets. *J. Geophys. Res.* 114, B10203.
- Solovitz, S.A., Mastin, L.G., Saffaraval, F., 2011. Experimental study of near-field entrainment of moderately overpressured jets. *J. Fluids. Engin.* 133, 051304.
- Sonder, I., Harp, A., Graettinger, A. H., Moitra, P., Valentine, G. A., Büttner, R., Zimanowski, B., 2018. Meter-scale experiments on magma-water interaction. *J. Geophys. Res. Solid Earth*, 123: 10,597–10,615, <https://doi.org/10.1029/2018JB015682>.
- Soria-Hoyo, C., Valverde, J.M., Roche, O., 2019. A laboratory-scale study on the role of mechanical vibrations in pore pressure generation in pyroclastic materials: implications for pyroclastic flows. *Bull. Volcanol.* 81: 12, <https://doi.org/10.1007/s00445-019-1271-3>.
- Soule, S.A., Cashman, K.V., 2005. Shear rate dependence of the pahoehoe-to'a'a transition: Analog experiments. *Geology* 33(5), 361-364.
- Sparks, R.S.J., Carey, S.N. and Sigurdson, H., 1991. Sedimentation from gravity currents generated by turbulent plumes. *Sedimentology*, 38: 839-856.
- Sparks, R.S.J., Carey, S.N., Sigurdsson, H., 1993. Sediment-laden gravity currents with reversing buoyancy. *Earth Planet. Sci. Lett.* 114: 243-257.
- Spieler, O., Dingwell, D.B., Alidibirov, M., 2004a. Magma fragmentation speed: an experimental determination. *J. Volcanol. Geotherm. Res.* 129: 109-123, doi: 10.1016/S0377-0273(03)00235-X.
- Spieler, O., Kennedy, B., Kueppers, U., Dingwell, D.B., Scheu, B., Taddeucci, J., 2004b. The fragmentation threshold of pyroclastic rocks. *Earth Planet. Sci. Lett.* 226: 139-148.
- Spina, L., Scheu, B., Cimarelli, C., Arciniega-Ceballos, A.; Dingwell, D.B., 2016. Time scales of foam stability in shallow conduits: Insights from analogue experiments. *Geoch. Geophys. Geosys.* 17: 4179–4194, doi: 10.1002/2016GC006455.
- Stasiuk, M.V., Jaupart, C., Sparks, R.S.J., 1993. Influence of cooling on lava-flow dynamics. *Geology* 21, 335-338.
- Stasiuk, M.V., Jaupart, C., 1997. Lava flow shapes and dimensions as reflections of magma system conditions. *J. Volcanol. Geoth. Res.* 78, 31-50.
- Stix, J., 2001. Flow evolution of experimental gravity currents: implications for pyroclastic flows at volcanoes. *J. Geol.* 109: 381-398.
- Stix, J., Phillips, J.C., 2012. An analog investigation of magma fragmentation and degassing: Effects of pressure, volatile content, and decompression rate. *J. Volcanol. Geotherm. Res.* 211-212: 12-23, doi:10.1016/j.jvolgeores.2011.10.001.
- Sugioka, I., Bursik, M.I., 1995. Explosive fragmentation of erupting magma. *Nature*, 373: 689-692.
- Sulpizio, R., Castioni, D., Rodriguez-Sedano, L.A., Sarocchi, D., Lucchi, F., 2016. The influence of slope-angle ratio on the dynamics of granular flows: insights from laboratory experiments. *Bull. Volcanol.* 78: 77, doi: 10.1007/s00445-016-1069-5.
- Sulpizio, R., Dellino, P., Doronzo, D.M., Sarocchi, D., 2014. Pyroclastic density currents: state of the art and perspectives. *J. Volcanol. Geotherm. Res.* 283: 36-65, <http://dx.doi.org/10.1016/j.jvolgeores.2014.06.014>.

- Taddeucci, J., Spieler, O., Kennedy, B., Pompilio, M., Dingwell, D.B., Scarlato, P., 2004. Experimental and analytical modeling of basaltic ash explosions at Mount Etna, Italy, 2001. *J. Geophys. Res.* 109: B08203, doi: 10.1029/2003JB002952.
- Taddeucci, J., Spieler, O., Ichiara, M., Dingwell, D.B., Scarlato, P., 2006. Flow and fracturing of viscoelastic media under diffusion-driven bubble growth: An analogue experiment for eruptive volcanic conduits. *Earth Planet. Sci. Lett.* 243: 771-785, doi:10.1016/j.epsl.2006.01.011.
- Taddeucci, J., Valentine, G.A., Sonder, I., White, J.D.M., Ross, P.-S., Scarlato, P., 2013. The effect of pre-existing craters on the initial development of explosive volcanic eruptions: An experimental investigation. *Geophys. Res. Lett.* 40, 507-510.
- Taisne, B., Tait, S., 2009. Eruption versus intrusion? Arrest of propagation of constant volume, buoyant, liquid-filled cracks in an elastic, brittle host. *J. Geophys. Res. Solid Earth*, 114: B06202, doi: 10.1029/2009JB006297.
- Taisne, B., Tait, S., 2011. Effect of solidification on a propagating dike. *J. Geophys. Res.* 116: B01206, doi: 10.1029/2009JB007058.
- Tait, S., Taisne, B., 2013. The dynamics of dike propagation. In: S.A. Fagents, T.K.P. Gregg and R.M.C. Lopes (Editors), *Modeling volcanic processes - The physics and mathematics of volcanism*. Cambridge University Press, pp. 32-54.
- Takada, A., 1990. Experimental study on propagation of liquid-filled crack in gelatin: shape and velocity in hydrostatic stress condition. *J. Geophys. Res.* 95(B6): 8471-8481.
- Takada, A., 1994. Development of a subvolcanic structure by the interaction of liquid-filled cracks. *J. Volcanol. Geotherm. Res.* 62: 207-224.
- Takahashi, T., Tsujimoto, H., 2000. A mechanical model for Merapi-type pyroclastic flow. *J. Volcanol. Geotherm. Res.* 98: 91-115.
- Telling, J., Dufek, J., 2012. An experimental evaluation of ash aggregation in explosive volcanic eruptions. *J. Volcanol. Geotherm. Res.* 209-210, 1-8.
- Telling, J., Dufek, J., Shaikh, A., 2013. Ash aggregation in explosive volcanic eruptions. *Geophys. Res. Lett.* 40, 2355-2360, doi:10.1002/grl.50376.
- Thomas, N., Tait, S., Koyaguchi, T., 1993. Mixing of stratified liquids by the motion of gas bubbles: application to magma mixing. *Earth Planet. Sci. Lett.* 115: 161-175. Toramaru, A., 1995. Numerical study of nucleation and growth of bubbles in viscous magmas. *J. Geophys. Res.* 100(B2): 1913-1931.
- Toramaru, A., 2006. BND (bubble number density) decompression rate meter for explosive volcanic eruptions. *J. Volcanol. Geotherm. Res.* 154: 303-316, doi:10.1016/j.jvolgeores.2006.03.027.
- Toramaru, A., Matsumoto, T., 2004. Columnar joint morphology and cooling rate: A starch-water mixture experiment. *J. Volcanol. Geoth. Res.* 109, B02205, doi: 10.1029/JB002686.
- Toramaru, A. and Maeda, K., 2013. Mass and style of eruptions in experimental geysers. *J. Volcanol. Geotherm. Res.* 257: 227-239, <http://dx.doi.org/10.1016/j.jvolgeores.2013.03.018>.
- Trigila, R., Battaglia, M. and Manga, M., 2007. An experimental facility for investigating hydromagmatic eruptions at high-pressure and high-temperature with application to the importance of magma porosity for magma-water interaction. *Bull. Volcanol.* 69: 365-372, doi: 10.1007/s00445-006-0081-6.
- Turner, J.S., 1973. *Buoyancy effects in fluids* (Cambridge Monographs on Mechanics). Cambridge: Cambridge University Press. doi: 10.1017/CBO9780511608827.
- Turner, J.S., Campbell, I.H., 1986. Convection and mixing in magma chambers. *Earth-Sci. Rev.* 23: 255-352.
- Valderrama, P., Roche, O., Samaniego, P., Van Wyk de Vries, B., Araujo, G., 2018. Granular fingering as a mechanism for ridge formation in debris avalanche deposits: Laboratory experiments and implications for Tutupaca volcano, Peru. *J. Volcanol. Geotherm. Res.* 349: 409-418, doi: <https://doi.org/10.1016/j.jvolgeores.2017.12.004>.
- Valentine, G.A., Bonadonna, C., Manzella, I., Clarke, A., Dellino, P., 2011. Large-scale experiments on volcanic processes. *EOS Trans. AGU*, 92, 11.
- Valentine, G.A., Graettinger, A.H., Macorps, E., Ross, P.-S., White, J.D.L., Döhring, E., Sonder, I., 2015. Experiments with vertically and laterally migrating subsurface explosions with applications to the geology of phreatomagmatic and hydrothermal explosion craters and diatremes. *Bull. Volcanol.* 77: 15, doi: 10.1007/s00445-015-0901-7.
- Valentine, G.A., White, J.D.L., Ross, P.-S., Amin, J., Taddeucci, J., Sonder, I., Johnson, P.J., 2012. Experimental craters formed by single and multiple buried explosions and implications for volcanic craters with emphasis on maars. *Geophys. Res. Lett.* 39: L20301, doi: 10.1029/2012GL053716.
- Valverde, J.M., Soria-Hoyo, C., 2015. Vibration-induced dynamical weakening of pyroclastic flows: Insights from rotating drum experiments. *J. Geophys. Res.* 120: 6182-6190, doi: 10.1002/2015JB012317.
- Van Eaton, A.R., Muirhead, J.D., Wilson, C.J.N., Cimarelli, C., 2012. Growth of volcanic ash aggregates in the presence of liquid water and ice: an experimental approach. *Bull. Volcanol.* 74, 1963-1984.
- Vaschy, A., 1892. Sur les lois de similitude en physique. *Annales Télégraphiques* 19: 25-28.
- Vasseur, J., Wadsworth, F.B. and Dingwell, D.B., 2018. Forecasting multiphase magma failure at the laboratory scale using acoustic emission data. *Frontiers in Earth Science*, 6: 132, doi: 10.3389/feart.2018.00132.
- Vasseur, J., Wadsworth, F.B., Lavallée, Y., Hess, K.U., Dingwell, D.B., 2013. Volcanic sintering: Timescales of viscous densification and strength recovery. *J. Geophys. Res.* 40: 5658-5664, doi: 10.1002/2013GL058105.
- Veitch, G., Woods, A.W., 2000. Particle recycling and oscillations of volcanic eruption columns. *J. Geophys. Res.* 105, B2, 2829-2842.
- Vergnolle, S., Ripepe, M., 2008. From Strombolian explosions to fire fountains at Etna Volcano (Italy): what do we learn from acoustic measurements? In: Lane, J. S. (Editor), *Fluid Motions in Volcanic Conduits: A Source of Seismic and Acoustic Signals*. Geol. Soc. London, Spec. Pub. pp. 103-124, doi: 10.1144/SP307.7.
- Wadsworth, F.B., Witcher, T., Vossen, C.E.J., Hess, K.-U., Unwin, H.E., Scheu, B., Castro, J.M., Dingwell, D.B., 2018. Combined effusive-explosive silicic volcanism straddles the multiphase viscous-to-brittle transition. *Nat. Comm.* 9:4696, doi: 10.1038/s41467-018-07187-w.

- Walters, A.L., Philips, J.C., Brown, R.J., Filed, M., Gernon, T., Stripp, G., Sparks, R.S.J., 2006. The role of fluidisation in the formation of volcanoclastic kimberlite: Grain size observations and experimental investigation. *J. Volcanol. Geotherm. Res.* 155: 119-137, doi:10.1016/j.jvolgeores.2006.02.005.
- Watanabe, T., Masuyama, T., Nagaoka, K., Tahara, T., 2002. Analog experiments on magma-filled cracks: Competition between external stresses and internal pressure. *Earth Planets Space*, 54: 1247–1261.
- Weit, A., Roche, O., Dubois, T. and Manga, M., 2018. Experimental measurement of the solid particle concentration in geophysical turbulent gas-particle mixtures. *J. Geophys. Res.: Solid Earth*, 123: 3747-3761. <https://doi.org/10.1029/2018JB015530>.
- Weit, A., Roche, O., Dubois, T. and Manga, M., 2019. Maximum solid phase concentration in geophysical turbulent gas-particle flows: Insights from laboratory experiments. *Geophys. Res. Lett.*, 46. <https://doi.org/10.1029/2019GL082658>.
- Wilson, C.J.N., 1980. The role of fluidization in the emplacement of pyroclastic flows: an experimental approach. *J. Volcanol. Geotherm. Res.* 8: 231-249.
- Wilson, C.J.N., 1984. The role of fluidization in the emplacement of pyroclastic flows, 2: experimental results and their interpretation. *J. Volcanol. Geotherm. Res.* 20: 55-84.
- Witham, F., Woods, A.W., Gladstone, C., 2006. An analogue experimental model of depth fluctuations in lava lakes. *Bull. Volcanol.* 69: 51-56, doi: 10.1007/s00445-006-0055-8.
- Wohletz, K.H., 1983. Mechanisms of hydrovolcanic pyroclast formation: grain-size, scanning electron microscopy, and experimental studies. *J. Volcanol. Geotherm. Res.* 17: 31-63.
- Woods, A.W., Caulfield, C.-C.P., 1992. A laboratory study of explosive volcanic eruptions. *J. Geophys. Res.* 97, B5, 6699-6712.
- Woods, A.W., Bursik, M.A., 1994. A laboratory study of ash flows. *J. Geophys. Res.* 99(B3): 4375-439.
- Woods, A.W., 1997. A note on non-Boussinesq plumes in an incompressible stratified environment. *J. Fluid Mech.* 345, 347-356.
- Woods, A.W., Bursik, M.I., Kurbatov, A.V., 1998. The interaction of ash flows with ridges. *Bull. Volcanol.* 60: 38-51.
- Woods, A.W., Cowan, A., 2009. Magma mixing triggered during volcanic eruptions. *Earth Planet. Sci. Lett.* 288: 132-137.
- Yamamoto, H., Takayama, K., Ishikawa, K., 2008. Model experiment on magma fragmentation in explosive volcanic eruptions. *J. Mineral. Petrol. Sci.* 103: 192-203, doi: 10.2465/jmps.060905.
- Yoshimura, S. and Nakamura, M., 2010. Fracture healing in a magma: An experimental approach and implications for volcanic seismicity and degassing. *J. Geophys. Res.* 115: B09209, doi: 10.1029/2009JB000834.
- Zavada, P., Kratinova, Z., Kusbach, V., Schulmann, K., 2009. Internal fabric development in complex lava domes. *Tectonophysics* 466, 101-113.
- Zhang, Y., Sturtevant, B., Stolper, E.M., 1997. Dynamics of gas-driven eruptions: Experimental simulations using CO<sub>2</sub>-H<sub>2</sub>O-polymer system. *J. Geophys. Res.* 102(B2): 3077-3096.
- Zimanowski, B., Büttner, R., Lorenz, V. and Häfele, H.-G., 1997. Fragmentation of basaltic melt in the course of explosive volcanism. *J. Volcanol. Geotherm. Res.* 102(B1): 803-814.
- Zimanowski, B., Fröhlich, G., Lorenz, V., 1991. Quantitative experiments on phreatomagmatic explosions. *J. Volcanol. Geotherm. Res.* 48: 341-358.

# The contribution of experimental volcanology to the study of the physics of eruptive processes, and related scaling issues: a review

Olivier Roche, Guillaume Carazzo

## Supplementary material

**Supplementary Table S1.** Analogue materials used in experiments on dykes and sills.

<b>Medium</b>	<b>Analogue Material</b>	<b>References</b>
<b>Magma</b>	Air, gases	Takada (1990), Muller et al. (2001), Ito and Martel (2002), Rivalta et al. (2005), Kervyn et al. (2009), Menand et al. (2010), Le Corvec et al. (2013)
	Water, aqueous solutions (+ alcohol, glycerin)	Takada (1990), McLeod and Tait (1999), Menand and Tait (2001, 2002), Kervyn et al. (2009), Kavanagh et al. (2006, 2013, 2015)
	Silicone oil	Takada (1994), McLeod and Tait (1999), Watanabe et al. (2002)
	Vegetable oil	Takada (1990), Chanceaux and Menand (2014, 2016), Daniels and Menand (2015)
	Sugar solution, Golden syrup	Taisne and Tait (2009), Kervyn et al. (2009)
	Parafin wax	Taisne and Tait (2009)
<b>Host rock</b>		
Elastic behavior	Gelatin	Takada (1990, 1994), McLeod and Tait (1999), Menand and Tait (2001, 2002), Muller et al. (2001), Ito and Martel (2002), Watanabe et al. (2002), Rivalta et al. (2005), Kervyn et al. (2009), Taisne and Tait (2009, 2011), Menand et al. (2010), Kavanagh et al. (2006, 2013, 2015), Le Corvec et al. (2013), Chanceaux and Menand (2014, 2016), Daniels and Menand (2015)
Brittle behavior	Granular material	Kavanagh et al. (2006), Kervyn et al. (2009), Galland et al. (2006)

**Supplementary Table S2.** Source and environmental conditions imposed in laboratory experiments simulating explosive volcanic jets and plumes.  $\rho_f$ : fluid density ( $\text{kg m}^{-3}$ ),  $\eta_f$ : fluid viscosity ( $\text{kg m}^{-1} \text{s}^{-1}$ ),  $\rho_a$ : ambient density ( $\text{kg m}^{-3}$ ),  $\rho_p$ : particle density ( $\text{kg m}^{-3}$ ),  $d_p$ : particle size ( $\mu\text{m}$ ),  $\varepsilon_p$ : particle concentration at the source,  $V_0$ : exit velocity ( $\text{m s}^{-1}$ ),  $L_0$ : vent diameter (mm),  $P_0$ : exit pressure (bar).

References: **1:** Carazzo and Jellinek (2012); **2:** Carazzo and Jellinek (2013); **3:** Carazzo et al. (2014); **4:** Carazzo et al. (2015); **5:** Cardoso and Zarrebini (2001a); **6:** Cardoso and Zarrebini (2001b); **7:** Carey et al. (1988); **8:** Chojnicki et al. (2006); **9:** Chojnicki et al. (2014); **10:** Chojnicki et al. (2016); **11:** Clarke et al. (2009); **12:** Del Bello et al. (2017); **13:** Dellino et al. (2007); **14:** Dellino et al. (2010); **15:** Dellino et al. (2014); **16:** Ernst et al. (1994); **17:** Ernst et al. (1996); **18:** Holasek et al. (1996); **19:** Jessop and Jellinek (2014); **20:** Jessop et al. (2016); **21:** Kaminski et al. (2005); **22:** Kieffer and Sturtevant (1984); **23:** Kitamura and Sumita (2011); **24:** Koyaguchi et al. (2009); **25:** Manzella et al. (2015); **26:** Medici and Waite (2016); **27:** Medici et al. (2014); **28:** Paillat and Kaminski (2014a); **29:** Paillat and Kaminski (2014b); **30:** Scollo et al. (2017); **31:** Solovitz and Mastin (2009); **32:** Solovitz et al. (2011); **33:** Sparks et al. (1991); **34:** Veitch and Woods (2000); **35:** Woods and Caufield (1992).

Ref.	Fluid	Particles	Environment	$\rho_f$	$\eta_f$	$\rho_a$	$\rho_p$	$d_p$	$\varepsilon_p$	$V_0$	$L_0$	$P_0$
1	water	cluster feldspar	stratified salt water	1000	$10^{-3}$	1000 - 1008	2600	150	2 - 10 vol%	0.3 - 1.3	3.2	1
2	water	cluster feldspar	stratified salt water	1000	$10^{-3}$	1000 - 1008	2600	150	2 - 10 vol%	0.3 - 1.3	3.2	1
3	salt water	-	stratified salt water	1000 - 1020	$10^{-3}$	1000 - 1030	-	-	-	0.14 - 1.1	5.5	1
4	hot air	hollow polymer spheres	air	1	$10^{-5}$	1	42	13 - 120	0.03 - 1.15 vol%	0.08 - 0.37	27.2	1
5	water	glass beads	salt water	1000	$10^{-3}$	1018 - 1021	2470	33 - 96	0.6 - 0.9 wt%	0.07 - 0.12	7	1
6	water	glass beads	salt water	1000	$10^{-3}$	1020	2470	38 - 115	0.6 wt%	0.08	7	1
7	water	silicon carbide	salt water	1000	$10^{-3}$	1021	3210	7 - 120	1 - 6 wt%	0.004 - 0.1	8	1
8	air	glass beads	air	1	$10^{-5}$	1	2500	45, 90, 150	0.4 - 0.47 vol%	350 - 650	38	1 - 70
9	water	silver-coated hollow glass spheres	water	1000	$10^{-3}$	1000	1100	10	n/a	1	20	1
10	water	-	water	1000	$10^{-3}$	1000	-	-	-	1.1 - 3.1	3, 9, 15	1
11	water (+ isopropyl or salt)	silica powder or glass beads	water	961 - 1037	$10^{-3}$	1000	2500	< 10, 45	2, 3.5 vol%	4 to 7	3, 15	1
12	air	volcanic material	air	1	$10^{-5}$	1	764 - 2846	125 - 1000	n/a	box experiment		1
13	air (explosion)	volcanic material	air	1	$10^{-5}$	1	2000	10 - 8000	0.17 wt%	7.4 - 12	600	130 - 175
14	air (explosion) or hot air	volcanic material	air	1	$2 \cdot 10^{-5}$ - $4 \cdot 10^{-4}$	1	2000	125 - 3000	0.04 - 0.12 wt%	27 - 110	300, 600	90 - 180
15	nitrogen (explosion)	hot or cold volcanic material	air	1	$10^{-5}$	1	1045 - 2408	21 - 3600	0.2 - 16 vol%	5 - 35	300, 600	n/a
16	cold or hot water	-	water	1000 - 1010	$10^{-3}$	1000	-	-	-	0.02 - 0.15	19	1
17	water	silicon carbide	salt water	1000	$10^{-3}$	> 1021	3210	115 - 327	0.1 - 0.2 wt%	0.08 - 0.8	4	1
18	water	silicon carbide	stratified salt water	> 1000	$10^{-3}$	> 1021	3210	17 - 37	0.4 - 2 wt%	feeder box		1
19	water	fine silica or silica sand	stratified salt water	1000	$10^{-3}$	1000 - 1012	2500 - 2520	40 - 325	0.01 - 10 vol%	0.3 - 2.3	3 - 13	1
20	water	silica powder	water	1000	$10^{-3}$	1000	2500	200 - 300	0 - 3.2 vol%	0.3 - 2.3	8 - 11	1
21	ethanol and ethylene glycol	-	water	964 - 968	$10^{-3}$	1000	-	-	-	0.03 - 0.37	2 - 6	1
22	freon, nitrogen or helium	-	air	1.13 - 35.8	$10^{-5}$	1	-	-	-	175 - 868	15	7.25
23	water, milk, saline solutions	-	water	1000 - 1800	$9.2 \cdot 10^{-4}$ - $1.2 \cdot 10^{-3}$	1000	-	-	-	0.2 - 1.5	1	1
24	water (+ NaCl /	glass beads	water (+ NaCl / $\text{CH}_2\text{CH}_2\text{OH}$ / $\text{Na}_6\text{O}_{18}\text{P}_6$ )	1004 - 1006	$1.4 \cdot 10^{-3}$	1010	2500 - 4200	23 - 100	n/a	box experiment		1

	CH <sub>2</sub> CH <sub>2</sub> OH / Na <sub>6</sub> O <sub>18</sub> P <sub>6</sub> )											
25	water	glass beads	sugar solution	1000 - 1001	10 <sup>-3</sup>	1008	2550	33 - 63	0.3 - 0.5 wt%	box experiment		1
26	nitrogen	-	air	7.96	10 <sup>-5</sup>	1	-	-	-	380 - 530	25.4	34.5 - 51.7
27	nitrogen	-	air	7.96	10 <sup>-5</sup>	1	-	-	-	750 - 810	25.4	51.7 - 81
28	salt water	glass hollow-spheres	water + ethanol	1000 - 1080	10 <sup>-3</sup>	980 - 1000	n/a	3 - 20	traces	0.1 - 0.3	0.5 - 1	1
29	water	glass hollow-spheres	water	1000	10 <sup>-3</sup>	1000	n/a	3 - 20	traces	0.1 - 1	0.2 - 1	1
30	water	glass beads, volcanic material	sugar solution	1000 - 1001	10 <sup>-3</sup>	1008	2550	< 32 - 180	0.3 - 0.5 wt%	box experiment		1
31	air	titanium dioxide	air + oil droplets	1	1.55 10 <sup>-5</sup>	1	4100	3	traces	58 - 283	9.25 - 11.8	6.2
32	air	titanium dioxide	air + oil droplets	1	1.6 10 <sup>-5</sup>	1	4100	3	traces	140 - 355	2.71 - 11.84	1.2 - 2.8
33	water	silicon carbide	salt water	1000	10 <sup>-3</sup>	1021	3210	28 - 131	1 wt%	0.003 - 0.01	8	1
34	water	glass beads	salt water	1000	10 <sup>-3</sup>	1005 - 1012	2500	40 - 70	1.5 wt%	n/a	10	1
35	water + methanol + ethylene glycol	-	water	977 - 995	10 <sup>-3</sup>	1000	-	-	-	0.006 - 0.04	10	1

**Supplementary Table S3.** Aggregation experiments (modified from Van Eaton et al. 2012).  $d_p$ : particle size ( $\mu\text{m}$ ), RE: relative humidity (%),  $T$ : ambient temperature ( $^{\circ}\text{C}$ ).

References: **1:** Del Bello et al. (2015); **2:** Gilbert and Lane (1994); **3:** James et al. (2002); **4:** James et al. (2003); **5:** Mueller et al. (2016); **6:** Schumacher (1994); **7:** Schumacher and Schmincke (1995); **8:** Telling and Dufek (2012); **9:** Telling and Dufek (2013); **10:** Van Eaton et al. (2012).

Ref.	Method	Binding agent	Particles	$d_p$	RE	$T$
1	turbulent fall chamber	electrostatic forces	volcanic material (Sakurajima, Campi Flegrei)	< 32 - 90	50/60	24/30
2	wind tunnel	liquid water	volcanic material, $\text{SiO}_2$ , $\text{SiC}$ , $\text{Al}_2\text{O}_3$ particles	< 50 - 300	10/85	n/a
3	pumice-fracturing fall chamber	electrostatic forces	volcanic material (Mt St Helens)	< 200	25/35	20/25
4	pumice-fracturing fall chamber	electrostatic forces	volcanic material (Mt St Helens)	< 200	25/35	20/25
5	fluidized bed in chamber	liquid water	glass beads, volcanic material (Laacher See)	< 50 - 300	12/45	87/93
6	powder-coating system	electrostatic forces	volcanic material (Laacher See)	< 250	n/a	n/a
7	powder-coating system, vibratory pan	electrostatic forces, liquid water	volcanic material (Laacher See)	< 250 - 2000	n/a	n/a
8	wind tunnel	liquid water	$\text{SiO}_2$ particles, volcanic material (Tungurahua)	90 - 250	23/93	20/21
9	low pressure fall chamber	liquid water	$\text{SiO}_2$ particles, volcanic material (Tungurahua, Mt St Helens)	90 - 150	11/95	17/25
10	vibratory pan	ice, liquid water	volcanic material (Oruanui, Eyjafjallajökull)	< 1414	< 30	-20/18

**Supplementary Table S4.** Source and boundary conditions imposed in laboratory experiments simulating lava flows and domes.  $\rho_f$ : fluid density ( $\text{kg m}^{-3}$ ),  $\eta_f$ : fluid viscosity ( $\text{kg m}^{-1} \text{s}^{-1}$ ),  $\rho_a$ : ambient density ( $\text{kg m}^{-3}$ ),  $\Delta T$ : initial temperature difference,  $U$ : flow velocity ( $\text{mm s}^{-1}$ ),  $L$ : flow thickness (cm),  $W$ : flow width (cm).

References: **1:** Applegarth et al. (2010); **2:** Bagdassarov and Pinkerton (2004); **3:** Balmforth et al. (2000); **4:** Blake and Bruno (2000); **5:** Buisson and Merle (2002); **6:** Canon-Tapia and Pinkerton (2000); **7:** Cashman et al. (2006); **8:** Castruccio et al. (2010); **9:** Castruccio et al. (2014); **10:** Dietterich et al. (2015); **11:** Edwards et al. (2013); **12:** Fink and Griffiths (1990); **13:** Fink and Griffiths (1992); **14:** Fink and Griffiths (1998); **15:** Garel et al. (2012); **16:** Garel et al. (2013); **17:** Garel et al. (2014); **18:** Garel et al. (2016); **19:** Gregg and Fink (1995); **20:** Gregg and Fink (2000); **21:** Griffiths and Fink (1992); **22:** Griffiths and Fink (1993); **23:** Griffiths and Fink (1997); **24:** Griffiths et al. (2003); **25:** Hulme (1974); **26:** Huppert et al. (1982); **27:** Huppert et al. (1984); **28:** Kerr (2009); **29:** Kerr et al. (2006); **30:** Lescinsky and Merle (2005); **31:** Lev et al. (2012); **32:** Lodge and Lescinsky (2009); **33:** Lyman and Kerr (2006); **34:** Lyman et al. (2004); **35:** Lyman et al. (2005); **36:** Merle (1998); **37:** Müller (1998a,b); **38:** Sakimoto and Gregg (2001); **39:** Soule and Cashman (2005); **40:** Stasiuk and Jaupart (1997); **41:** Stasiuk et al. (1993); **42:** Toramaru and Matsumoto (2004); **43:** Zavada et al. (2009).

Ref.	Fluid	Environment	Slope	$\rho_f$	$\eta_f$	$\rho_a$	$\Delta T$	$U$	$L$	$W$
1	silicone + sand/plaster/quartz	air	4 - 12	1400	$10^4$	1	0	0.01 - 0.1	$\sim 1$	1 - 10
2	golden syrup + air bubbles	air	0	$\sim 1300$	$10^2$	1	0	rotational van-viscometer		
3	wax + kaolin slurries	air	0	1320	15	1	0	0.05 - 0.15	0.4 - 1.2	2 - 10
4	PEG (600)	cold water	0	1097 - 1118	$5 - 13 \times 10^{-2}$	997	22 - 41	0.2 - 5.6	n/a	6 - 40
5	silicone putty	air	0	$\sim 1200$	$\sim 10^5$	1	0	$3e-5 - 4e-4$	0.5 - 3.6	8 - 10
6	molten basalt	air	0 - 25	2700	$\sim 150$	1	1175 - 1350	n/a	n/a	n/a
7	PEG (600)	cold salt water	3.5	1120 - 1122	0.12 - 0.13	>1000	14 - 16	0.01 - 0.2	0.4 - 10.4	8 - 15
8	golden syrup + sugar crystals/xanthan gum	air	0	1345 - 1386	78	1	0	n/a	n/a	5
9	syrup + sugar crystals or nylon cubes / hair gel	air	5 - 15	1000 - 1500	$45 - 10^3$	1	0	0.01 - 1	0.5 - 3	100
10	syrup / molten basalt	air	3 - 25	1443 - 2700	$10^2$	1	0 - 1300	1 - 10	0.1 - 1	< 150
11	molten basalt	air/ice*	5 - 10	2700	150	1	1300	50 - 100	$\sim 5$	15 - 20
12	PEG (600)	cold sucrose water	0 - 6.5	1125 - 1128	0.18 - 0.23	1003 - 1116	3 - 19	n/a	n/a	n/a
13	PEG (600)	cold sucrose water	0	1033 - 1168	0.1 - 0.18	1003 - 1116	4 - 19	0.3 - 0.8	$\sim 2.1$	$\sim 10$
14	PEG (600)+ kaolin	cold water	0	$\sim 1500$	0.1 - 0.18	1000	4 - 19	n/a	2 - 5	10 - 20
15	silicone oil	air	0	942 - 975	2.7 - 15	1	0 - 36	0.01 - 6	0.1 - 0.5	2 - 25
16	silicone oil	air	0	949	3	1	28 - 29	0.03	0.1 - 0.5	2 - 25
17	PEG (3515)	air	0	1100	$10^{-1} - 10^5$	1	22 - 26	3 - 45	0.3	2 - 30
18	silicone oil / glucose syrup / wax	air	0	942 - 1390	$10^{-1} - 10^5$	1	0 - 40	0.01 - 50	0.1 - 0.5	2 - 30
19	PEG (600)	cold sucrose water	0 - 60	1033 - 1168	0.1 - 0.18	1003 - 1116	4 - 19	0.3 - 0.8	$\sim 2.1$	$\sim 10$
20	PEG (600)	cold sucrose water	1 - 60	1125 - 1128	0.18 - 0.23	1003 - 1116	3 - 19	5 - 8	< 0.3 - 0.5	3 - 21
21	PEG (600)	cold sucrose water	0	1033 - 1168	0.1 - 0.18	1003 - 1116	4 - 19	0.3 - 0.8	$\sim 2.1$	$\sim 10$
22	PEG (600)	cold sucrose water	0	1126	$1 - 1.6 \times 10^{-4}$	1003 - 1116	4 - 23	0.06 - 1.1	1 - 10	4 - 20
23	PEG (600)+ kaolin	cold water	0	1450	0.78	1000	0 - 17	0.08 - 0.3	2 - 7	4 - 28
24	PEG (600)	cold saline solution	1.6 - 7	1120 - 1122	0.12 - 0.13	>1000	14 - 16	0.01 - 0.2	0.4 - 10.4	8 - 15
25	water + kaolin	air	3 - 9	1120 - 1250	1.8 - 20	1	0	0.018 - 5.8	0.3 - 1.9	8.7 - 35

26	silicon oil	air	0	~950	~1.25 - 105	1	0	1.3e-4	0.5 - 0.01	1 - 14
27	aqueous solution	alcohol	0	n/a	n/a	n/a	61	confined chamber		
28	hot sucrose solution	air/PEG 600*	3.5	1281	0.0287	1/1126*	46*	48	0.36	4.8
29	PEG (600)	cold water	1.3 - 8.5	1121	0.12 - 0.13	1000	18 - 22	n/a	n/a	25 - 80
30	silicone + sand/plaster/quartz	air	0 - 6	1400	10 <sup>4</sup>	1	0	n/a	2.8 - 4.2	20
31	molten basalt	air	5 - 20	2700	150	1	1300	75	8	49
32	starch water	air	0	800 - 1200	n/a	1	0	confined chamber		
33	PEG (600)+ kaolin	air / cold salt water	1.5 - 19.5	1257 - 1439	0.19 - 2.13	1 - 1245	0 - 33	0.1 - 30	4 - 80	15 - 25
34	PEG (600)+ kaolin	cold water	0 - 60	~1500	0.1 - 0.18	1000	2 - 20	n/a	n/a	8 - 20
35	PEG (600)+ kaolin	air / cold salt water	0	1257 - 1439	0.19 - 2.13	1 - 1245	0 - 33	0.05 - 500	12 - 24	15 - 25
36	silicone	air	0 - 10	1350	10 <sup>4</sup>	1	48	n/a	1 - 2	20 - 50
37	starch water	air	0	1484	n/a	1	0	confined chamber		
38	PEG	sucrose water	10 - 60	1108 - 1124	0.07 - 0.17	~1000	>0	1.3 - 17.3	0.5 - 1.4	2.6 - 16.8
39	corn syrup + rice grains	air	0	1440	50 - 100	1	0	rotational van-viscometer		
40	golden syrup	air	0	1438	46 - 91	1	0	n/a	1.2 - 2.2	27 - 55
41	golden syrup	salt water	0	1108 - 1438	3.2x10 <sup>-5</sup> - 130	1000	0 - 33	n/a	~1	100
42	starch water	air	0	n/a	n/a	1	0	confined chamber		
43	plaster+water slurries	sand	0	2300	0.8 - 6.2	2500	0	0.6- 12.5	4 - 11	20 - 25